Identification and Characterization of Oxalate Oxidoreductase, a Novel Thiamine Pyrophosphate-dependent Enzyme that Enables Anaerobic Growth on Oxalate

by

Elizabeth A. Pierce

A dissertation submitted in partial fulfillment
of the requirements for the degree of
Doctor of Philosophy
(Biological Chemistry)
in The University of Michigan
2011

Doctoral committee:

Professor Stephen W. Ragsdale, Chair
Professor Ruma Banerjee
Professor Carol A. Fierke
Associate Professor Bruce A. Palfey
Assistant Professor Nicolai Lehnert

ACKNOWLEDGEMENTS

I have many people to thank for their help and support during my studies. First, I would like to thank Dr. Steve Ragsdale, who has been my mentor and advisor for many years, through both my Master's and Ph.D. studies. I have learned so much in your lab, from your advice and teaching, in discussions with you, and from the great example you set in your constant enthusiasm both for science and for life.

I would like to thank my committee members, Dr. Ruma Banerjee, Dr. Carol Fierke, Dr. Nicolai Lehnert and Dr. Bruce Palfey for your help guidance. Particular thanks are due to Dr. Banerjee. You served on both my Master's and Ph.D. committees and your helpful criticism and suggestions for my work, both during my committee meetings and during many joint group meetings, have been invaluable.

My thesis would have been impossible without the constant help and advice and support I have gotten from members of Dr. Ragsdale's lab over the years. I owe a large debt of gratitude to so many people, including Dr. Javier Seravalli, Brady Brabec, Dr. Vekalet Tek, Dr. Mathias Antoine, Dr. Güneş Bender, Dr. Joe Darty, Jeff Hill, Stelian Pop, Dr. Nirupama Gupta, Dr. Kuljeet Singh, Dr. Hisashi Hemmi, Dr. Mishtu Dey, Dr. Ryan Kunz, Dr. Xianghui Li, Dr. Yuzhen Zhou, Ali Bogart, Mike Dowling, Dr. Ireena Bagai, and Andrea Morris.

My thesis would also have been impossible without collaborations with many other scientists. I would like to thank Dr. Don Becker (University of Nebraska-Lincoln) for collaborating on OOR, Dr. Yan Kung and Dr. Cathy Drennan (Massachusetts Institute of Technology) for collaboration on ACS, Ted Huston (University of Michigan) for your beautifully painstaking metal analysis work, and Oliver Lazarus, Thomas Woolerton, Fraser Armstrong (Oxford University) and colleagues for collaboration on CODH.

I would like to thank the Department of Biological Chemistry for its support during my studies. Special thanks go to all of the administrative staff. Without your work, it would not be possible for me to get anything done. In particular, I wish to thank Julie Woodruff for so much help in getting the supplies need for our experiments and for so patiently helping me figure out problems with ordering and shipping things. Thanks also to Beth Goodwin for your guidance, help and very good advice throughout my degree, particularly during the last few stressful months.

Thanks are due here to my parents and Sarah, for your unconditional love and support and a lot of good advice, to Christian for so many more things than I can mention here, but particularly for giving me a break from thinking about science by telling me so many stories about how crazy the rest of the world is, and to Nicholas for your almost endless patience, even when the answer to the question “do you have to go to work today?” was so obvious that instead you started saying “I’m not even going to ask.....”

TABLE OF CONTENTS

LIST OF FIGURES

FIGURE

LIST OF TABLES

TABLE

LIST OF ABBREVIATIONS

ACS, acetyl-CoA synthase

BisTris, 2-[bis(2-hydroxyethyl)-amino]-2-(hydroxymethyl)propane-1,3-dio

CH_3-H_4folate, methyl tetrahydrofolate

CoA, coenzyme A

CFeSP, corrinoid iron-sulfur protein

CODH, carbon monoxide dehydrogenase

EPR, electron paramagnetic resonance

FAD, flavin adenine dinucleotide

Fd, ferredoxin

H_4folate, tetrahydrofolate

M. thermoacetica, *Moorella thermoacetica*

NBS, N-bromosuccinamide

OFOR, 2-oxoacid:ferredoxin oxidoreductase

OOR, oxalate oxidoreductase

PFOR, pyruvate:ferredoxin oxidoreductase

TPP, thiamine pyrophosphate

ABSTRACT

Identification and Characterization of Oxalate Oxidoreductase, a Novel Thiamine Pyrophosphate-dependent Enzyme that Enables Anaerobic Growth on Oxalate

by

Elizabeth A. Pierce

Chair: Stephen W. Ragsdale

Moorella thermoacetica is an anaerobic bacterium that uses the Wood-Ljungdahl or reductive acetyl-CoA pathway as a terminal electron accepting pathway for heterotrophic and autotrophic growth on many substrates. One electron donor to *M. thermoacetica* is oxalate. Oxalate is an important substrate for various microbes and is produced in soil, where *M. thermoacetica* lives. We identified a novel enzyme, oxalate oxidoreductase (OOR) that enables growth on oxalate. This is the first known enzyme that directly oxidizes oxalate in an anaerobic organism, reducing an electron carrier by two electrons, and producing carbon dioxide or bicarbonate. In conjunction with the Wood-Ljungdahl pathway, OOR constitutes a novel path for oxalate metabolism. Exposure to oxalate induces expression of the three subunits of OOR. Like other members of the 2-oxoacid:ferredoxin oxidoreductase family, OOR contains thiamine pyrophosphate and three 4Fe-4S clusters. However, unlike previously

characterized members of this family, OOR does not use coenzyme A as a substrate. Oxalate is oxidized with k_{cat} of 0.09 per second and K_m of 60 micromolar at pH 8.0. The enzyme transfers its reducing equivalents to a broad range of electron acceptors, including ferredoxin and carbon monoxide dehydrogenase. OOR can oxidize pyruvate, also without any requirement for CoA. Pyruvate oxidation leads to inhibition of OOR, probably through formation of stable TPP-bound intermediates. One of these intermediates is a hydroxyethyl-TPP radical like the one formed as part of the pyruvate:ferredoxin oxidoreductase catalytic cycle. The formation of this radical on OOR indicates a common mechanism with other 2-oxoacid:ferredoxin oxidoreductases.

A second line of research explores the importance for catalysis of a sodium binding site on the key Wood-Ljungdahl pathway enzyme acetyl-CoA synthase. Mutation of a residue in the sodium binding site decreases the CO/acetyl-CoA exchange activity by approximately 25-fold. The activity of wild-type ACS is dependent on the sodium concentration with an approximately four-fold increase in the activity between 40 micromolar and 5 millimolar. The sodium concentration where the effect is seen is lower than the expected concentration in the cell.

CHAPTER I

Introduction

The main work described in this thesis is on the enzymology of oxalate metabolism by *Moorella thermoacetica*. This bacterium has been the model organism for the elucidation of the acetate synthesis pathway called the Wood-Ljungdahl pathway. This chapter will describe the metabolism of *M. thermoacetica*, production and degradation of oxalate by other organisms and prior research on oxalate metabolism in *M. thermoacetica*. The enzyme that degrades oxalate in *M. thermoacetica* is closely related to pyruvate:ferredoxin oxidoreductase (PFOR). The reactions catalyzed by PFOR and its catalytic mechanism are described here.

M. thermoacetica (originally named *Clostridium thermoaceticum*) is a Gram-positive Clostridium from the Thermoanaerobacteriaceae family (*1*). It is a strictly anaerobic, soil-dwelling thermophile that grows optimally at 55-60 ^{o}C. It was first isolated from horse manure in experiments separating cellulose fermenting organisms from the organisms that ferment the simple sugars that are products of cellulose metabolism (*2*). When it was isolated, *M. thermoacetica* was remarkable for its ability to form more than two moles of acetate from one mole of glucose, which indicated either an unusual metabolism of glucose to three two-carbon units, or an acetate synthesis pathway

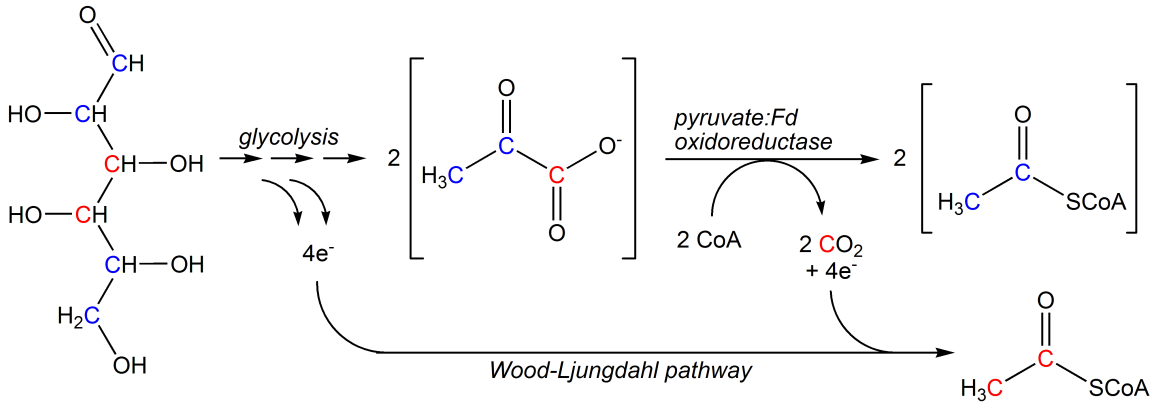

Figure 1.1. Stoichiometric acetyl-CoA formation from glucose.

(*2*). Some of the earliest isotope tracer studies showed that *M. thermoacetica* could make acetate directly from CO_2, specifically CO_2 from carbons 3 and 4 of glucose (Figure 1.1). The specific activity of $^{14}CO_2$ incorporation into acetate suggested its total synthesis from CO_2 (*3*); it was shown conclusively by mass spectrometry that $^{13}CH_3{}^{13}COO^-$ was formed from $^{13}CO_2$ (*4*). The steps of the acetate synthesis pathway were described by Harland Wood and Lars Ljungdahl, and by researchers working in their labs, so the pathway is named after these two scientists. Besides being interesting from a metabolic standpoint, the Wood-Ljungdahl pathway has provided a wealth of fascinating metal-dependent enzymes and reactions for study, including two of nine currently known nickel-dependent enzymes, a unique cobalt to nickel methyl transfer reaction, and the first known tungsten-dependent enzyme.

1.1 Description of the Wood-Ljungdahl pathway

In the Wood-Ljungdahl pathway, one CO_2 is reduced to the methyl level, a second CO_2 is reduced to CO, and these are joined with CoA by the key enzyme of the

pathway, acetyl-CoA synthase (ACS) (Figure 1.2). In the methyl branch of the pathway, CO_2 is first reduced to formate by an NADPH-dependent formate dehydrogenase that contains a tungstopterin co-factor and selenocysteine. This was the first enzyme found to be tungsten-dependent (*5*). Formate is ligated to tetrahydrofolate (H_4folate) in an ATP-dependent reaction (*6, 7*). Three steps are needed to convert formyl-H_4folate to methyl-H_4folate. 5,10-Methenyl-H_4folate cyclohydrolase and methylene-H_4folate dehydrogenase activities are catalyzed by one enzyme in *M. thermoacetica*, (*8-10*), but by separate enzymes in other closely related acetogens (*11*). The final reduction step in the methyl branch is catalyzed by a 5,10-methylene-H_4folate reductase that contains iron-sulfur

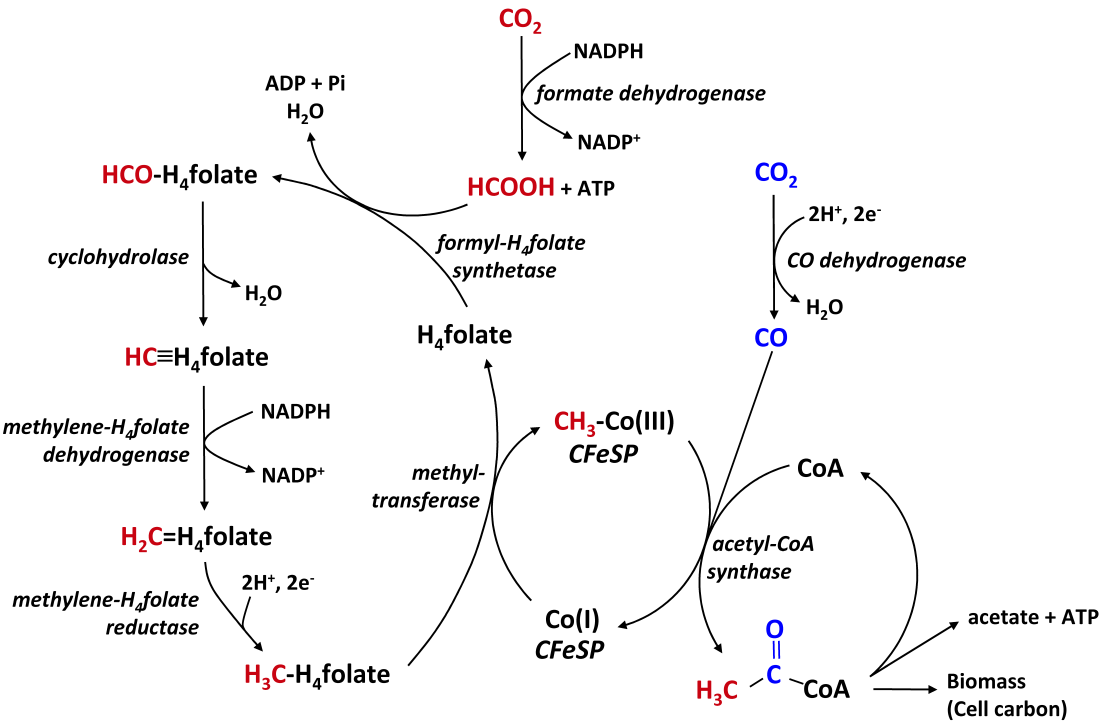

Figure 1.2. The Wood-Ljungdahl pathway of carbon fixation.

clusters and FAD (*12*). The methyl group is transferred from CH_3-H_4folate to the Co^{+1} center of a corrinoid iron-sulfur protein (CFeSP) by a methyltransferase (*13, 14*).

In the carbonyl branch of the pathway, carbon monoxide dehydrogenase (CODH) reduces CO_2 to CO, which becomes the carbonyl group of acetyl-CoA (*15, 16*). In *M. thermoacetica*, the Wood-Ljungdahl pathway enzyme, CODH, forms a bifunctional complex with ACS. The CO molecule that becomes the carbonyl group of acetyl-CoA is not released into solution, but instead is channeled 70 Å from the CODH active site to the ACS active site (*17, 18*), where ACS catalyzes formation of acetyl-CoA from the methyl group donated by CH_3-Co^{3+} CFeSP, CO and CoA (*16, 19*).

CODH and ACS are both nickel-dependent enzymes with unique active site metal clusters. The C-cluster, the site of CODH activity, is a distorted $NiFe_3S_4$ cubane linked by one sulfur atom to a fourth iron atom (*18, 20-22*). Substrate binding and catalysis take place on Ni and the Fe that is not part of the cubane (*23*). The ACS active site, the A-cluster, consists of a Fe_4S_4 cluster bridged by cysteine to a Ni-Ni site (*18, 22*). EPR, ENDOR, Mössbauer, infrared spectroscopic and ^{14}C-labeling studies indicate that the nickel proximal to the Fe_4S_4 cluster binds the methyl and carbonyl groups during catalysis (*24-27*). It is bridged by two additional cysteine residues to the second nickel, which has square planar coordination and is in the Ni^{2+} state, probably through the whole catalytic cycle. The overall reaction is not a redox reaction, but ACS requires reductive activation to enter the catalytic cycle, and the proximal Ni atom undergoes redox changes during catalysis (*28*), although there has been much disagreement about the necessary oxidation states of different components of the A-cluster (*29, 30*).

1.2 Distribution of the Wood-Ljungdahl pathway, and its metabolic roles

The Wood-Ljungdahl pathway plays several roles in the metabolism of *M. thermoacetica*. When *M. thermoacetica* was isolated it was grown only heterotrophically, and it wasn't discovered until forty years later that the Wood-Ljungdahl pathway enables its autotrophic growth by fixing CO_2 into acetyl-CoA, which enters biosynthetic pathways in the cell (*31*). The pathway also allows energy conservation when CO_2 is used as a terminal electron acceptor, by coupling CO_2 reduction to generation of a chemiosmotic gradient across the cell membrane (*32*). As well as conserving energy from autotrophic substrates, the Wood-Ljungdahl pathway can act as a sink for reducing equivalents from energy-rich substrates like glucose. Whether growth on sugars with CO_2 engages the same energy conservation pathway that is used during autotrophic growth has not been clearly shown, but the mass of cells produced per mole of substrate for *M. thermoacetica* growing on simple sugars was higher than would be expected from substrate level phosphorylation alone, as shown by calculations of Y_{ATP} values (grams of cells formed per mole of ATP produced from substrate catabolism) (*33*).

The Wood-Ljungdahl pathway is found in taxonomically diverse groups of organisms. It is present in some spirochaetes, deltaproteobacteria, chloroflexi and other clostridia among bacteria, and in methanogenic archaea. All phyla that contain organisms with the Wood-Ljungdahl pathway contain many species that do not and there is no apparent taxonomic conservation of the pathway (*34*). Not all organisms with the Wood-Ljungdahl pathway produce acetate as the main reduced product. In methanogenic archaea, energy conservation is coupled to methane production, and the Wood-Ljungdahl pathway is used for carbon assimilation, and, in acetoclastic methanogenesis as well, for

converting acetate to methane (*35*). Some bacteria also apparently use the Wood-Ljungdahl pathway only for carbon assimilation. An example of this is *Carboxydothermus hydrogenoformans*, also a member of the Thermoanaerobacteriaceae family which grows autotrophically on CO with H_2 as the main reduced product (*36*).

1.3 Growth of *M. thermoacetica* on various electron donors and acceptors

Experiments described in this thesis focus on the enzyme that allows *M. thermoacetica* to use oxalate as an electron donor and carbon source. When *M. thermoacetica* is grown on oxalate as an electron donor, the flow of reductant to respiratory pathways is regulated differently than reductant flow from other substrates. This section will describe the variety of electron donors and acceptors that can be used for growth by *M. thermoacetica* and detail what is known about how reductant flow to two terminal electron acceptors, CO_2 and nitrate, is regulated during growth on most substrates.

While it is now known to use diverse electron donors and acceptors, *M. thermoacetica* was isolated and for many years was grown only in medium containing glucose or other simple sugars (*2, 33*). It wasn't until forty years after the first isolation that it was shown to be capable of autotrophic growth on H_2/CO_2 or CO (*31, 37*), and that it expresses hydrogenase (*38*), which allows autotrophic growth by providing reducing equivalents for the Wood-Ljungdahl pathway. A diverse set of substrates has since been shown to support acetogenic growth, or growth with acetate as the main reduced product. These include glucose, fructose, xylose (*33*), H_2, CO (*31*), methanol (*37*), one-, two- and three-carbon acids formate (*39*), oxalate, glyoxylate (*40*), glycolate (*41*), pyruvate (*39*)

and lactate (*42*), short-chain alcohols such as ethanol, *n*-propanol and *n*-butanol (*43*), and methyl groups of many methoxylated aromatic compounds (*44, 45*). *M. thermoacetica* can also use electron acceptors other than CO_2, including nitrate, which is reduced to nitrite and ammonia (*46*), nitrite (*47*), dimethylsulfoxide and thiosulfate (*48*).

1.3.1 *Effect of nitrate on growth by the Wood-Ljungdahl pathway*

Nitrate is a strong regulator of the Wood-Ljungdahl pathway, and in some conditions, it blocks autotrophic growth of *M. thermoacetica*. Diverting electrons from the Wood-Ljungdahl pathway in the presence of nitrate would theoretically allow the bacterium to gain more energy for growth, because the redox potential of the CO_2/acetate couple is more negative (E_0' = -0.29 V vs. standard hydrogen electrode) than that of the NO_3^-/NO_2^- couple (E_0' = +0.43 V vs. standard hydrogen electrode) so the stoichiometry of ATP production should be higher with nitrate as the terminal electron acceptor (*49*). Oxalate is the only substrate known so far that causes *M. thermoacetica* to preferentially reduce CO_2 rather than nitrate.

When CO_2 is the electron acceptor, methanol and methyl groups of vanillate and vanillin, and glucose are converted to acetate with yields close to the stoichiometries predicted by equations 1.1 and 1.2. The predicted stoichiometry for growth on CO is given in eq. 1.3 (*2, 46, 50*).

$$4 \text{ aromatic-OCH}_3 + 2CO_2 + 2H_2O \rightarrow 4 \text{ aromatic-OH} + 3CH_3COOH \quad (1.1)$$

$$\text{glucose} + 2H_2O \rightarrow 3CH_3COOH + 4H^+ \quad (1.2)$$

$$4CO + 2H_2O \rightarrow 2CO_2 + CH_3COOH \quad (1.3)$$

The ability of *M. thermoacetica* to use the Wood-Ljungdahl pathway is impaired by nitrate (*39, 51*). When the same substrates are used for growth in the presence of nitrate, the acetate yield from glucose is approximately two-thirds as much as when nitrate is absent, which is consistent with the expected oxidation of glucose to two acetate and two CO_2 molecules by the Embden-Meyerhof-Parnas pathway. Acetate is not detected in cultures oxidizing CO or methyl groups to reduce nitrate; nitrite and ammonia are produced instead. Oxidation of CO and methyl groups can only be coupled to nitrate reduction when *M. thermoacetica* is grown on undefined medium with yeast extract, so that apparently the Wood-Ljungdahl pathway is not needed for carbon assimilation (*46*). As described above, *M. thermoacetica* can grow on H_2 as an electron donor. In undefined medium, either NO_3^- or CO_2 can be used as the terminal electron acceptor. Although ATP production from cultures growing with nitrate or carbon dioxide as the electron acceptor has not been measured directly, growth is more efficient (eight-fold more biomass is produced per mole of H_2 consumed) during nitrate-dependent growth than during CO_2-dependent growth (*39*), consistent with the preferential use of a higher potential acceptor to conserve more energy.

Because nitrate blocks use of the Wood-Ljungdahl pathway, it affects autotrophic growth by *M. thermoacetica*. Formate, methanol and CO do not individually support growth in the presence of nitrate when cells are grown in a minimal, defined medium. Growth on vanillate and syringate, of which *M. thermoacetica* uses only the methyl groups, is also blocked in the presence of nitrate. However, when both CO and vanillate or syringate are present along with nitrate, *M. thermoacetica* can use at least the final steps of the Wood-Ljungdahl pathway to synthesize enough acetyl-CoA for autotrophic

growth, although no extra acetate is made (*39*). The mechanism of the block on the Wood-Ljungdahl pathway is at least partly known: levels of a cytochrome that is thought to be important for anaerobic respiration during growth on the pathway are lower in nitrate-grown cells (*39*) and, under some growth conditions, expression of Wood-Ljungdahl pathway genes is decreased at the transcriptional level (*51*).

1.4 Growth of *M. thermoacetica* on oxalate

1.4.1 *Pathways for oxalate production and degradation in other organisms*

The growth of *M. thermoacetica* in the soil has not been carefully studied, but the competitiveness of the organism in this environment is likely to come, at least in large part, from its ability to make use of so many different substrates (*48*). In pure culture, oxalate is a poor substrate for supporting growth, but in soils, where it is produced by many organisms, the ability to use oxalate in mixed growth on many substrates may confer an advantage on *M. thermoacetica*.

Oxalate is produced by some plants, fungi and bacteria. It comes from degradation of oxaloacetate in fungi and bacteria (*52*) and a few plants (*53*), and is a product of ascorbic acid and galactose metabolism in plants (*54, 55*). In many environments, oxalate is released into the soil, where it can reach high micromolar concentrations (*56*). This has been proposed to benefit the oxalate-producing organisms by increasing the availability of other ions, including phosphate (by chelating metals from calcium and Fe^{3+} phosphates) and aluminium (by forming a soluble complex with Al^{+3}), and by forming insoluble precipitates with toxic metals (*57*). Fungal release of oxalate has also been implicated in pathogenesis in some plant tissues (*58*).

Metabolism of oxalate in organisms other than *M. thermoacetica* occurs by three known mechanisms. The best known oxalate-degrading bacterium is *Oxalobacter formigenes*, which does not oxidize oxalate. Instead, it conserves energy by a formate:oxalate antiporter that generates an electrochemical gradient across the membrane when oxalate is taken up and metabolized to formate, which is excreted by the cell. After transport into the cell, oxalate is first activated to oxalyl-CoA and then is decarboxylated, giving formyl-CoA and CO_2. The oxalyl-CoA ligation step does not require energy, because it is catalyzed by a formyl-CoA transferase that exchanges a formyl group for an oxalyl-group on CoA, thus producing formate and regenerating oxalyl-CoA (*59, 60*). Other bacteria that use oxalyl-CoA decarboxylase and formyl-CoA transferase include *Lactobacillus* species (*61*).

Other pathways for oxalate degradation include oxidative and non-oxidative decarboxylation of oxalate. Non-oxidative decarboxylation of oxalate (to formate and CO_2) has been seen in the fungi *Aspergillus niger* and *Flammulina velupties*, and in bacteria including *Bacillus subtilis* (*62-64*). In fungi, oxalate decarboxylase is induced by oxalate. The *B. subtilis* enzyme is induced by acid, and was proposed to be part of a pathway, along with glyoxylate dehydrogenase and formate dehydrogenase that would produce ATP by substrate level phosphorylation and help maintain the pH of the cytoplasm in acidic environments (*64*). The X-ray crystal structure of oxalate decarboxylase from *B. subtilis* has been solved. It is a cupin-family enzyme that like other oxalate decarboxylases, requires manganese. Although the reaction catalyzed by oxalate decarboxylase is not a redox reaction, this enzyme requires O_2 for catalysis (*62, 65*).

Oxalate undergoes oxidative decarboxylation by germin, another manganese dependent cupin-family enzyme. Germin is an O_2-dependent enzyme that generates H_2O_2 using the reducing equivalents from oxalate oxidation. Germin also has superoxide dismutase activity. Germin is part of a family of desiccation-tolerant seed-storage proteins that are extremely resistant to environmental extremes including H_2O_2. Its activity is thought to be linked to controlling levels of calcium in cell walls (oxalate forms a very tight complex with calcium), and to be part of plants' response to pathogens through the production of H_2O_2 which leads to hydroxyl radical production (*58*).

1.4.2 *Prior research on oxalate metabolism in M. thermoacetica*

M. thermoacetica converts oxalate to acetate with oxidation of oxalate by two electrons (*41*). The expected stoichiometry of acetate production from oxalate is given in Equation 1.4. The experimentally observed stoichiometry matches this well (*41*):

$$4\ COO^-\text{-}COO^- + 3\ H^+ \rightarrow CH_3COO^- + 6\ CO_2 \qquad (1.4)$$

Oxalate was hypothesized to be metabolized by a different pathway than that used for oxidation of glycolate and glyoxylate, related two-carbon substrates that *M. thermoacetica* also uses for growth, because the protein expression profile of cells grown on oxalate showed high levels of two proteins that were not induced in cells grown on other substrates, including glyoxylate (*40*). Furthermore, growth on glyoxylate in the presence of both CO_2 and nitrate was coupled to nitrate reduction, and CO_2 was only reduced to acetate during the stationary phase, so nitrate is clearly the preferred electron sink for growth on glyoxylate. However, when cells are grown on oxalate, CO_2 was reduced to acetate during exponential growth, and nitrate was only reduced during the

stationary phase, so CO_2, not nitrate, is the preferred electron acceptor for oxalate-dependent growth. Interestingly, in both oxalate- and glyoxylate-grown cells, the membranous cytochrome *b* whose expression has been shown to be repressed by nitrate, was absent in cells grown with nitrate. Therefore during oxalate-dependent growth in the presence of nitrate, electron flow must be changed in some way to accommodate this lack of expression (*66*). Oxalate is the only substrate known so far for which CO_2 is the preferred electron acceptor.

Among other enzymes known to metabolize oxalate, oxalate decarboxylase and oxalate oxidase could both be ruled out as possibilities for *M. thermoacetica*, since both are O_2 dependent. *M. thermoacetica* has a sequence with low homology to oxalyl-CoA decarboxylase, but no homolog of formyl-CoA transferase, so a different enzyme would be needed if oxalate were activated to oxalyl-CoA (*34*).

Oxalate-dependent methyl and benzyl viologen reduction activity were measured in extracts and whole cells of oxalate-grown *M. thermoacetica* (*67*). An electron acceptor was necessary for oxalate consumption. Oxalate was oxidized in the presence of CO_2, nitrate or thiosulfate in whole cells, and in the presence of benzyl viologen in cell extracts. In assays of cell extracts, both $NADP^+$ and benzyl viologen could act as electron acceptors for formate dehydrogenase activity, but $NADP^+$ was not reduced in oxalate-dependent assays, which strongly suggested that formate was not an intermediate in oxalate oxidation. It was also shown that addition of CoA did not change the rate of methyl viologen reduction, indicating that activation of oxalate by ligation to form oxalyl-CoA was not a step in oxalate metabolism (*67*), although it was possible that in cell extracts, a CoA regenerating system would render addition of CoA to assays

unnecessary. As shown in this thesis, both conclusions, i.e. that CoA is not needed for oxalate oxidation and that formate is not an intermediate in the oxalate degradation pathway, were correct. We found that oxalate is metabolized by a novel enzyme, which is CoA independent, and does not produce formate as an intermediate in oxalate oxidation.

1.5 Reactions catalyzed by pruvate:ferredoxin oxidoreductase, a homolog of oxalate oxidoreductase

The central enzyme of pyruvate metabolism in *M. thermoacetica* is pyruvate:ferredoxin oxidoreductase (PFOR). The reaction catalyzed by PFOR is shown in Equation 1.5. Decarboxylation and oxidation of pyruvate and ligation of the resulting acetyl intermediate to CoA take place in the active site of PFOR, on thiamine pyrophosphate. The electrons from oxidation of pyruvate are passed from the active site through a series of three $[Fe_4S_4]^{2+/1+}$ clusters to the surface of the enzyme, where ferredoxin and CODH can act as electron acceptors[1].

$$CH_3COCOO^- + CoAS^- + Fd_{ox} \leftrightarrow CH_3COSCoA + CO_2 + Fd_{red} \qquad (1.5)$$

As shown in Eq. 1.5, the PFOR reaction is reversible, and PFOR can also act as a pyruvate synthase (*68*). The CO_2/pyruvate couple has a low redox potential (-0.54 V vs. SHE). Because the CO_2/CO couple has a similar reduction potential (-0.52 V vs. SHE (*69*)), CO oxidation can drive the formation of pyruvate. At *in vivo* concentrations of CO_2 and acetyl-CoA, the pyruvate synthase reaction occurs about 8-fold slower than the PFOR reaction at physiological concentrations of pyruvate and CoA. The k_{cat} and k_{cat}/K_m values for the reverse reaction are also only about 8-10-fold slower than for the pyruvate

[1]The reaction shown in Eq. 1.5 produces two moles of electrons per mole of substrate. PFOR from *M. thermoacetica* uses a ferredoxin with two $[Fe_4S_4]^{2+/1+}$ clusters as an electron acceptor in *in vitro* assays.

oxidation reaction, which indicates that PFOR is fairly efficient in catalyzing the reaction in either direction (*68*).

CoA is absolutely required for the PFOR reaction as well as the reactions of other members of this family, which includes 2-oxobutyrate, 2-oxoglutarate, 2-oxoisovalerate and indolepyruvate oxidases. The sole known exception to production of acetyl-CoA from pyruvate is *Pyrococcus furiosus* PFOR, which also produces acetaldehyde as a side product in the PFOR reaction (up to 0.4 moles of acetaldehyde per mole of acetyl-CoA produced) (*70*). This pyruvate decarboxylase reaction is independent of an electron acceptor (ferredoxin) but is dependent on CoA. This is most likely because of a specific conformation of the protein stabilized by CoA binding, since in the normal PFOR reaction, the sulfur of CoA is important in the catalytic mechanism (as described in section 1.5.1) (*71*), whereas in the reaction that produces acetaldehyde, desulfo-CoA can replace CoA. It is not known how the *P. furiosus* active site is altered to make acetaldehyde release favourable enough to compete with oxidation (*70*).

1.5.1 *Mechanism of pyruvate:ferredoxin oxidoreductase and other 2-oxoacid:ferredoxin oxidoreductases*

The mechanism of *M. thermoacetica* PFOR (shown in Figure 1.3) has been thoroughly studied (*71-73*). The first steps are common to all TPP-dependent enzymes that metabolize pyruvate. The first step is deprotonation of C2 of the thiazole ring of TPP, which forms an ylide that can perform a nucleophilic attack on C2 of pyruvate (step 2), to form a lactyl-TPP intermediate. This is followed by decarboxylation of lactyl-TPP (step 3), leaving an enamine or hydroxyethyl-TPP (HE-TPP) anion intermediate (the

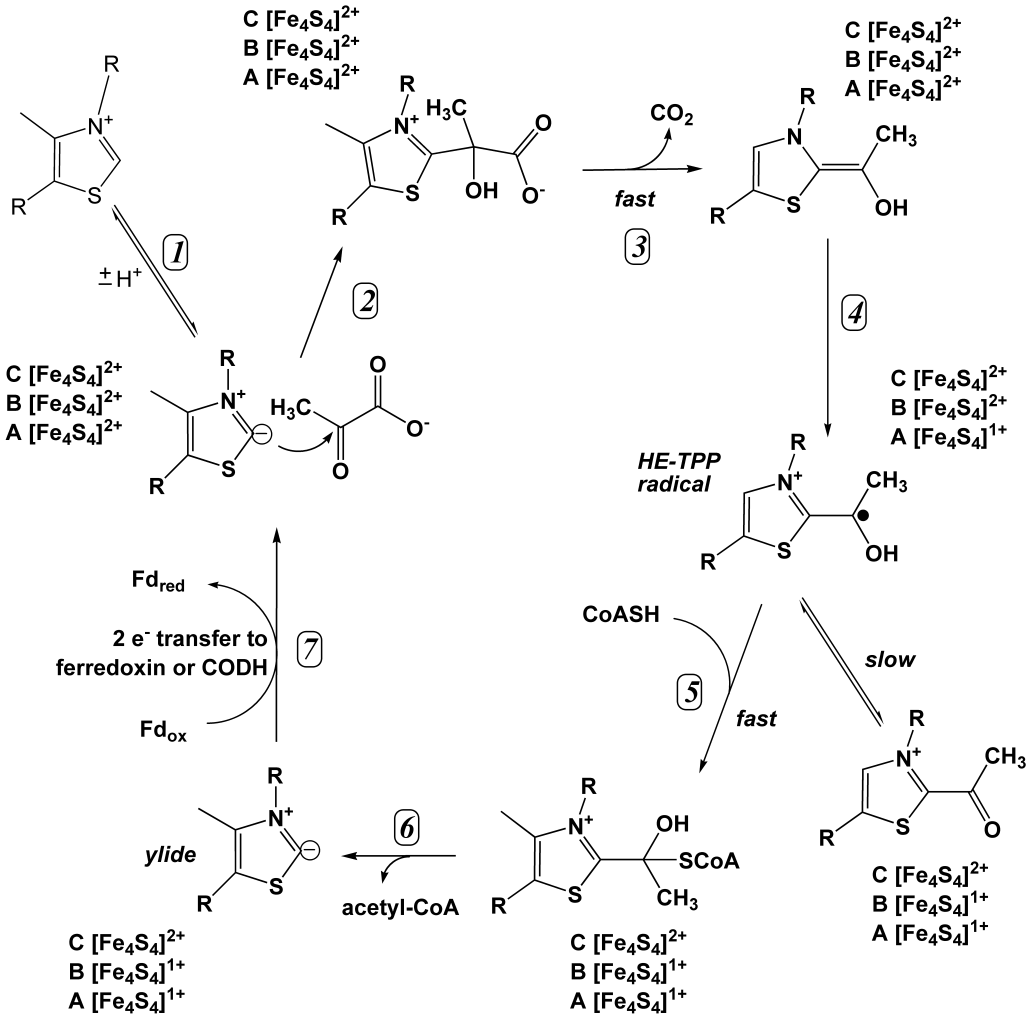

Figure 1.3. Mechanism of pyruvate:ferredoxin oxidoreductase.

protonated form, the enamine, is shown in Figure 1.3). Figure 1.4 shows several fates for this intermediate when pyruvate is metabolized by different enzymes. Acetaldehyde can be released from TPP, in pyruvate decarboxylase and in the side reaction of *P. furiosus* PFOR discussed in section 1.5. The enamine can be oxidized, followed by hydrolysis of the acetyl-TPP product in pyruvate oxidase, or concomitant with reduction of a disulfide from lipoic acid in the pyruvate dehydrogenase complex. In PFOR, and in *Lactobacillus*

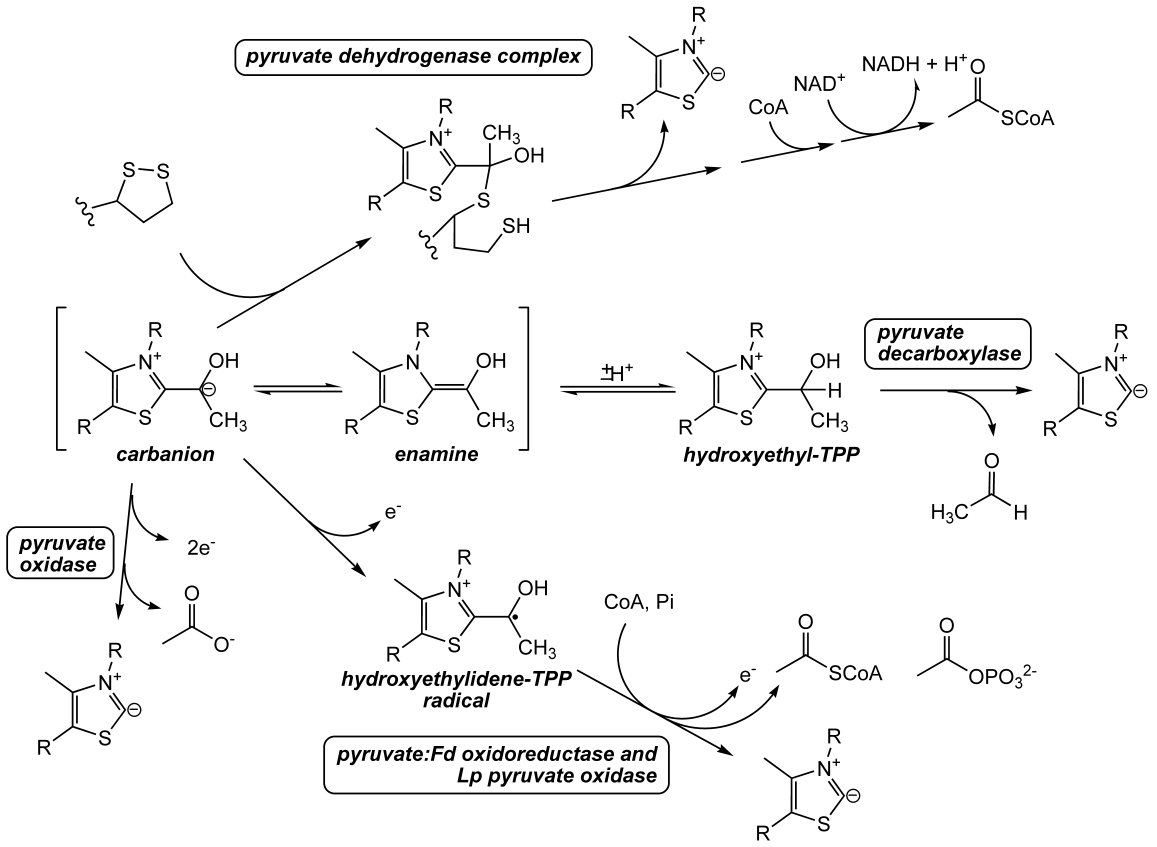

Figure 1.4. Fates of the hydroxyethyl-TPP intermediate in different enzymes that metabolize pyruvate.

plantarum pyruvate oxidase, the HE-TPP is oxidized by one electron to form a hydroxyethyl-TPP radical (step 4). In PFOR, the electron that leaves the HE-TPP intermediate is passed to the first of three $[Fe_4S_4]^{2+/1+}$ clusters, which has a redox potential of -0.54 V. The second and third clusters have potentials of -0.515 V and -0.39 V, so electrons should flow from the active site through a series of iron-sulfur clusters to the surface of the protein (*73*). In *L. plantarum* pyruvate oxidase, the immediate acceptor is FAD instead of an FeS cluster.

The HE-TPP radical has been proposed to be intermediate in all PFOR reactions, and in all other reactions of the 2-oxoacid:ferredoxin oxidoreductase (2-OFOR) enzyme family of which PFOR is part (*72*). It was first seen by EPR of pyruvate and 2-oxobutyrate:ferredoxin oxidoreductases[2] purified from *Halobacterium halobium* that were treated with substrates in the absence of CoA; the spectra of the radicals were lost upon addition of CoA (*74*). Since then, the HE-TPP radical has been extensively characterized. From X-ray crystallography studies, it was proposed to be a sigma radical, primarily localized on C2 of TPP and C2α of the hydroxyethyl group. In this hypothesized intermediate, the bond between C2 and C2α was lengthened, the thiazole ring was in a bent conformation, and its aromaticity was lost (*75*). EPR and computational studies directly contradict this result. In these studies, replacement of carbon and nitrogen at different positions within the substrate and the thiazole ring of TPP results in somewhat altered EPR spectra with most substitutions. Comparison of parameters from simulations of these spectra with those obtained from electronic structure calculations give, as the most consistent result, a pi radical delocalized over the aromatic thiazole ring and C2α and the hydroxyl of the hydroxyethyl group (*76*).

In the absence of CoA, the HE-TPP radical is stable with a half life of several minutes (k = 0.001 s^{-1}). When CoA is present, the rate constant of decay of the radical is equal to the rate constant of the first electron transfer (k = 140 s^{-1}), and the radical does not appreciably accumulate (*71, 72*). This means that CoA enhances the rate of electron transfer by about 10^5-fold. Experiments in which the sulfur of CoA was removed

[2] Although the radical is referred to throughout this discussion as the hydroxyethyl-TPP radical, other 2-OFOR enzymes, which use pyruvate, 2-oxobutyrate, 2-oxoglutarate, 2-oxoisovalerate and indolepyruvate form the corresponding radicals by one-electron oxidation of the substrate moiety that is left on TPP after the decarboxylation step.

indicate that while most of the binding energy of CoA comes from the bulk of the CoA molecule, this binding energy does not account for the enhancement of the rate of electron transfer by CoA, and addition of desulfo-CoA does not stimulate the rate of electron transfer (*71*). One explanation of these results is that the potential of the hydroxyethyl-TPP radical is not sufficiently low to readily drive reduction of the proximal iron-sulfur cluster, but that addition of the negatively charged CoA molecule to the HE-TPP radical forms an anion radical adduct with a significantly more negative redox potential (*71*). Oxidation of this more reducing radical adduct would result in a larger driving force for electron transfer to the proximal cluster. Results from *L. plantarum* pyruvate oxidase are consistent with this hypothesis. For that enzyme, it was calculated, based on the assumption that the intrinsic driving force for the reaction totally accounts for the change in the rate of electron transfer when phosphate is added to the radical, that the relative potentials of the enamine and hydroxyethyl-TPP radical are -0.757 and -0.487 V, while the potential of the anion radical adduct that would form when phosphate adds to the HE-TPP radical was calculated as -0.817 V (*77*). The increase in electron transfer rate upon phosphate addition to the HE-TPP radical of *L. plantarum* pyruvate oxidase is about 100-fold, so a greater decrease in potential would be needed to account for the increase in the electron transfer rate when CoA is added to PFOR.

The subsequent steps in the PFOR mechanism consists of formation (step 6) and release (step 7) of acetyl-CoA and electron transfers between the iron-sulfur clusters and an external electron acceptor (step 8), which regenerate the active ylide and the oxidized forms of the $[Fe_4S_4]^{2+/1+}$ clusters.

1.6 References

(1) Collins, M. D., Lawson, P. A., Willems, A., Cordoba, J. J., Fernandez-Garayzabal, J., Garcia, P., Cai, J., Hippe, H., and Farrow, J. A. E. (1994) The Phylogeny of the Genus Clostridium: Proposal of Five New Genera and Eleven New Species Combinations. *Int. J. Syst. Bacteriol. 44*, 812-826.

(2) Fontaine, F. E., Peterson, W. H., McCoy, E., Johnson, M. J., and Ritter, G. J. (1942) A New Type of Glucose Fermentation by *Clostridium thermoaceticum*. *J. Bacteriol. 43*, 701-715.

(3) Barker, H. A., and Kamen, M. D. (1945) Carbon Dioxide Utilization in the Synthesis of Acetic Acid by *Clostridium thermoaceticum*. *Proc. Natl. Acad. Sci. U.S.A. 31*, 219-225.

(4) Wood, H. G., and Harris, D. L. (1952) A Study of Carbon Dioxide Fixation by Mass Determination of the Types of C13-Acetate. *J. Biol. Chem. 194*, 905-931.

(5) Yamamoto, I., Saiki, T., Liu, S. M., and Ljungdahl, L. G. (1983) Purification and properties of NADP-dependent formate dehydrogenase from *Clostridium thermoaceticum*, a tungsten-selenium-iron protein. *J. Biol. Chem. 258*, 1826-1832.

(6) Sun, A. Y., Ljungdahl, L., and Wood, H. G. (1969) Total Synthesis of Acetate from CO_2 II. Purification and Properties of Formyltetrahydrofolate Synthetase from *Clostridium thermoaceticum*. *J. Bacteriol. 98*, 842-844.

(7) Ljungdahl, L., Brewer, J. M., Neece, S. H., and Fairwell, T. (1970) Purification, Stability, and Composition of Formyltetrahydrofolate Synthetase from *Clostridium thermoaceticum*. *J. Biol. Chem. 245*, 4791-4797.

(8) O'Brien, W. E., Brewer, J. M., and Ljungdahl, L. G. (1973) Purification and Characterization of Thermostable 5,10-Methylenetetrahydrofolate Dehydrogenase from *Clostridium thermoaceticum*. *J. Biol. Chem. 248*, 403-408.

(9) Ljungdahl, L. G., O'Brien, W. E., Moore, M. R., Liu, M.-T., and Donald B. McCormick, L. D. W. (1980) [83] Methylenetetrahydrofolate dehydrogenase from *Clostridium formicoaceticum* and methylenetetrahydrofolate dehydrogenase, methenyltetrahydrofolate cyclohydrolase (combined) from *Clostridium thermoaceticum*, in *Methods Enzymol.* pp 599-609, Academic Press.

(10) Liu, M.-T., and Ljungdahl, L. G. (1978) Methylenetetrahydrofolate cyclohydrolase and methylenetetrahydrofolate dehydrogenase combined from *Clostridium thermoaceticum*. *Fed. Proc. 37*, 1805.

(11) Clark, J. E., and Ljungdahl, L. G. (1982) Purification and properties of 5,10-methenyltetrahydrofolate cyclohydrolase from *Clostridium formicoaceticum*. *J. Biol. Chem. 257*, 3833-3836.

(12) Park, E. Y., Clark, J. E., DerVartanian, D. V., and Ljungdahl, L. G. (1991) 5,10-Methylenetetrahydrofolate Reductases: Iron-Sulfur-Zinc Flavoproteins of Two Acetogenic Clostridia, in *Chemistry and Biochemistry of Flavoenzymes* (Müller, F., Ed.) pp 389-400, CRC Press, Boca Raton.

(13) Drake, H. L., Hu, S. I., and Wood, H. G. (1981) Purification of five components from *Clostridium thermoaceticum* which catalyze synthesis of acetate from pyruvate and methyltetrahydrofolate. Properties of phosphotransacetylase. *J. Biol. Chem. 256*, 11137-11144.

(14) Hu, S. I., Pezacka, E., and Wood, H. G. (1984) Acetate synthesis from carbon monoxide by *Clostridium thermoaceticum*. Purification of the corrinoid protein. *J. Biol. Chem. 259*, 8892-8897.

(15) Ragsdale, S. W., Clark, J. E., Ljungdahl, L. G., Lundie, L. L., and Drake, H. L. (1983) Properties of purified carbon monoxide dehydrogenase from *Clostridium thermoaceticum*, a nickel, iron-sulfur protein. *J. Biol. Chem. 258*, 2364-2369.

(16) Ragsdale, S. W., and Wood, H. G. (1985) Acetate biosynthesis by acetogenic bacteria. Evidence that carbon monoxide dehydrogenase is the condensing enzyme that catalyzes the final steps of the synthesis. *J. Biol. Chem. 260*, 3970-3977.

(17) Seravalli, J., and Ragsdale, S. W. (2000) Channelling of Carbon Monoxide during Anaerobic Carbon Dioxide Fixation. *Biochemistry 39*, 1274-1277.

(18) Doukov, T. I., Iverson, T. M., Seravalli, J., Ragsdale, S. W., and Drennan, C. L. (2002) A Ni-Fe-Cu Center in a Bifunctional Carbon Monoxide Dehydrogenase/ Acetyl-CoA Synthase. *Science 298*, 567-572.

(19) Hu, S. I., Drake, H. L., and Wood, H. G. (1982) Synthesis of acetyl coenzyme A from carbon monoxide, methyltetrahydrofolate, and coenzyme A by enzymes from *Clostridium thermoaceticum*. *J. Bacteriol. 149*, 440-448.

(20) Drennan, C. L., Heo, J., Sintchak, M. D., Schreiter, E., and Ludden, P. W. (2001) Life on carbon monoxide: X-ray structure of *Rhodospirillum rubrum* Ni-Fe-S carbon monoxide dehydrogenase. *Proc. Natl. Acad. Sci. U.S.A. 98*, 11973-11978.

(21) Dobbek, H., Svetlitchnyi, V., Gremer, L., Huber, R., and Meyer, O. (2001) Crystal structure of a carbon monoxide dehydrogenase reveals a [Ni-4Fe-5S] cluster. *Science 293*, 1281-5.

(22) Darnault, C., Volbeda, A., Kim, E. J., Legrand, P., Vernede, X., Lindahl, P. A., and Fontecilla-Camps, J. C. (2003) Ni-Zn-[Fe4-S4] and Ni-Ni-[Fe4-S4] clusters in closed and open [alpha] subunits of acetyl-CoA synthase/carbon monoxide dehydrogenase. *Nat. Struct. Mol. Biol. 10*, 271-279.

(23) Kung, Y., Doukov, T. I., Seravalli, J., Ragsdale, S. W., and Drennan, C. L. (2009) Crystallographic Snapshots of Cyanide- and Water-Bound C-Clusters from Bifunctional Carbon Monoxide Dehydrogenase/Acetyl-CoA Synthase. *Biochemistry 48*, 7432-7440.

(24) Ragsdale, S. W., Wood, H. G., and Antholine, W. E. (1985) Evidence that an iron-nickel-carbon complex is formed by reaction of CO with the CO dehydrogenase from *Clostridium thermoaceticum*. *Proc. Natl. Acad. Sci. U.S.A. 82*, 6811-6814.

(25) Xia, J., Hu, Z., Popescu, C. V., Lindahl, P. A., and Münck, E. (1997) Mössbauer and EPR Study of the Ni-Activated α-Subunit of Carbon Monoxide Dehydrogenase from *Clostridium thermoaceticum*. *J. Am. Chem. Soc. 119*, 8301-8312.

(26) George, S. J., Seravalli, J., and Ragsdale, S. W. (2005) EPR and Infrared Spectroscopic Evidence That a Kinetically Competent Paramagnetic Intermediate is Formed When Acetyl-Coenzyme A Synthase Reacts with CO. *J. Am. Chem. Soc. 127*, 13500-13501.

(27) Barondeau, D. P., and Lindahl, P. A. (1997) Methylation of Carbon Monoxide Dehydrogenase from Clostridium thermoaceticum and Mechanism of Acetyl Coenzyme A Synthesis. *J. Am. Chem. Soc. 119*, 3959-3970.

(28) Bender, G., and Ragsdale, S. W. (2011) Evidence That Ferredoxin Interfaces with an Internal Redox Shuttle in Acetyl-CoA Synthase during Reductive Activation and Catalysis. *Biochemistry 50*, 276-286.

(29) Lindahl, P. (2004) Acetyl-coenzyme A synthase: the case for a Ni_p^0-based mechanism of catalysis. *J. Biol. Inorg. Chem. 9*, 516-524.

(30) Ragsdale, S. W. (2007) Nickel and the carbon cycle. *J. Inorg. Biochem. 101*, 1657-1666.

(31) Kerby, R., and Zeikus, J. G. (1983) Growth of *Clostridium thermoaceticum* on H_2/CO_2 or CO as energy source. *Curr. Microbiol. 8*, 27-30.

(32) Hugenholtz, J., Ivey, D. M., and Ljungdahl, L. G. (1987) Carbon monoxide-driven electron transport in *Clostridium thermoautotrophicum* membranes. *J. Bacteriol. 169*, 5845-7.

(33) Andreesen, J. R., Schaupp, A., Neurauter, C., Brown, A., and Ljungdahl, L. G. (1973) Fermentation of Glucose, Fructose, and Xylose by *Clostridium thermoaceticum*: Effect of Metals on Growth Yield, Enzymes, and the Synthesis of Acetate from CO_2. *J. Bacteriol. 114*, 743-751.

(34) Pierce, E., Xie, G., Barabote, R. D., Saunders, E., Han, C. S., Detter, J. C., Richardson, P., Brettin, T. S., Das, A., Ljungdahl, L. G., and Ragsdale, S. W.

(2008) The complete genome sequence of *Moorella thermoacetica* (f. *Clostridium thermoaceticum*). *Environ. Microbiol. 10*, 2550-2573.

(35) Ferry, J. G. (1999) Enzymology of one-carbon metabolism in methanogenic pathways. *FEMS Microbiol. Rev. 23*, 13-38.

(36) Soboh, B., Linder, D., and Hedderich, R. (2002) Purification and catalytic properties of a CO-oxidizing:H_2-evolving enzyme complex from *Carboxydothermus hydrogenoformans*. *Eur. J. Biochem. 269*, 5712-21.

(37) Daniel, S. L., Hsu, T., Dean, S. I., and Drake, H. L. (1990) Characterization of the H_2- and CO-dependent chemolithotrophic potentials of the acetogens *Clostridium thermoaceticum* and *Acetogenium kivui*. *J. Bacteriol. 172*, 4464-71.

(38) Drake, H. L. (1982) Demonstration of hydrogenase in extracts of the homoacetate-fermenting bacterium *Clostridium thermoaceticum*. *J. Bacteriol. 150*, 702-9.

(39) Frostl, J. M., Seifritz, C., and Drake, H. L. (1996) Effect of nitrate on the autotrophic metabolism of the acetogens *Clostridium thermoautotrophicum* and *Clostridium thermoaceticum*. *J. Bacteriol. 178*, 4597-603.

(40) Daniel, S. L., and Drake, H. L. (1993) Oxalate- and Glyoxylate-Dependent Growth and Acetogenesis by *Clostridium thermoaceticum*. *Appl. Environ. Microbiol. 59*, 3062-3069.

(41) Seifritz, C., Fröstl, J. M., Drake, H. L., and Daniel, S. L. (1999) Glycolate as a metabolic substrate for the acetogen Moorella thermoacetica. *FEMS Microbiol. Lett.170*, 399-405.

(42) Talabardon, M., Schwitzguebel, J. P., and Peringer, P. (2000) Anaerobic thermophilic fermentation for acetic acid production from milk permeate. *J. Biotechnol. 76*, 83-92.

(43) Beatty, P. S., and Ljungdahl, L. G. (1991) in *Abstracts of the 91st General Meeting of the American Society for Microbiology* pp 236, American Society for Microbiology, Washington, D.C.

(44) Wu, Z. R., Daniel, S. L., and Drake, H. L. (1988) Characterization of a CO-dependent O-demethylating enzyme system from the acetogen *Clostridium thermoaceticum*. *J. Bacteriol. 170*, 5747-50.

(45) Daniel, S. L., Keith, E. S., Yang, H., Lin, Y. S., and Drake, H. L. (1991) Utilization of methoxylated aromatic compounds by the acetogen *Clostridium thermoaceticum*: expression and specificity of the co-dependent O-demethylating activity. *Biochem. Biophys. Res. Commun. 180*, 416-22.

(46) Seifritz, C., Daniel, S. L., Gossner, A., and Drake, H. L. (1993) Nitrate as a preferred electron sink for the acetogen *Clostridium thermoaceticum*. *J. Bacteriol. 175*, 8008-13.

(47) Seifritz, C., Drake, H. L., and Daniel, S. L. (2003) Nitrite as an energy-conserving electron sink for the acetogenic bacterium *Moorella thermoacetica*. *Curr. Microbiol. 46*, 329-33.

(48) Drake, H. L., and Daniel, S. L. (2004) Physiology of the thermophilic acetogen *Moorella thermoacetica*. *Res. Microbiol. 155*, 422-436.

(49) Thauer, R. K., Jungermann, K., and Decker, K. (1977) Energy conservation in chemotrophic anaerobic bacteria. *Microbiol. Mol. Biol. Rev. 41*, 100-180.

(50) Bache, R., and Pfennig, N. (1981) Selective isolation of *Acetobacterium woodii* on methoxylated aromatic acids and determination of growth yields. *Arch. Microbiol. 130*, 255-261.

(51) Arendsen, A. F., Soliman, M. Q., and Ragsdale, S. W. (1999) Nitrate-dependent regulation of acetate biosynthesis and nitrate respiration by *Clostridium thermoaceticum*. *J. Bacteriol. 181*, 1489-95.

(52) Kubicek, C. P., Schreferl-Kunar, G., Wohrer, W., and Rohr, M. (1988) Evidence for a cytoplasmic pathway of oxalate biosynthesis in *Aspergillus niger*. *Appl. Environ. Microbiol. 54*, 633-7.

(53) Kim, C. H., and Thompson, L. T. (2005) Deactivation of Au/CeO_x water gas shift catalysts. *J. Catal. 230*, 66-74.

(54) Kostman, T. A., Tarlyn, N. M., Loewus, F. A., and Franceschi, V. R. (2001) Biosynthesis of L-ascorbic acid and conversion of carbons 1 and 2 of L-ascorbic acid to oxalic acid occurs within individual calcium oxalate crystal idioblasts. *Plant Physiol. 125*, 634-40.

(55) Keates, S. E., Tarlyn, N. M., Loewus, F. A., and Franceschi, V. R. (2000) L-Ascorbic acid and L-galactose are sources for oxalic acid and calcium oxalate in Pistia stratiotes. *Phytochemistry 53*, 433-40.

(56) Strobel, B. W. (2001) Influence of vegetation on low-molecular-weight carboxylic acids in soli solution - a review. *Geoderma 99*, 169-198.

(57) Gadd, G. M. (1999) Fungal production of citric and oxalic acid: importance in metal speciation, physiology and biogeochemical processes. *Adv. Microb. Physiol. 41*, 47-92.

(58) Woo, E.-J., Dunwell, J. M., Goodenough, P. W., Marvier, A. C., and Pickersgill, R. W. (2000) Germin is a manganese containing homohexamer with oxalate oxidase and superoxide dismutase activities. *Nat. Struct. Biol. 7*, 1036-1040.

(59) Anantharam, V., Allison, M. J., and Maloney, P. C. (1989) Oxalate:formate exchange: the basis for energy coupling in *Oxalobacter*. *J. Biol. Chem*. *264*, 7244-7250.

(60) Baetz, A. L., and Allison, M. J. (1989) Purification and characterization of oxalyl-coenzyme A decarboxylase from *Oxalobacter formigenes*. *J. Bacteriol. 171*, 2605-2608.

(61) Turroni, S., Vitali, B., Bendazzoli, C., Candela, M., Gotti, R., Federici, F., Pirovano, F., and Brigidi, P. (2007) Oxalate consumption by lactobacilli: evaluation of oxalyl-CoA decarboxylase and formyl-CoA transferase activity in *Lactobacillus acidophilus*. *J. Appl. Microbiol. 103*, 1600-9.

(62) Emiliani, E., and Riera, B. (1968) Enzymatic oxalate decarboxylation in *Aspergillus niger*: II. Hydrogen peroxide formation and other characteristics of the oxalate decarboxylase. *Biochim. Biophys. Acta, Enzymol. 167*, 414-421.

(63) Mehta, A., and Datta, A. (1991) Oxalate decarboxylase from *Collybia velutipes*. Purification, characterization, and cDNA cloning. *J. Biol. Chem*. *266*, 23548-53.

(64) Tanner, A., and Bornemann, S. (2000) *Bacillus subtilis* YvrK Is an Acid-Induced Oxalate Decarboxylase. *J. Bacteriol. 182*, 5271-5273.

(65) Anand, R., Dorrestein, P. C., Kinsland, C., Begley, T. P., and Ealick, S. E. (2002) Structure of oxalate decarboxylase from *Bacillus subtilis* at 1.75 A resolution. *Biochemistry 41*, 7659-69.

(66) Seifritz, C., Frostl, J. M., Drake, H. L., and Daniel, S. L. (2002) Influence of nitrate on oxalate- and glyoxylate-dependent growth and acetogenesis by *Moorella thermoacetica*. *Arch. Microbiol. 178*, 457-64.

(67) Daniel, S. L., Pilsl, C., and Drake, H. L. (2004) Oxalate metabolism by the acetogenic bacterium *Moorella thermoacetica*. *FEMS Microbiol. Lett.231*, 39-43.

(68) Furdui, C., and Ragsdale, S. W. (2000) The role of pyruvate ferredoxin oxidoreductase in pyruvate synthesis during autotrophic growth by the Wood-Ljungdahl pathway. *J. Biol. Chem*. *275*, 28494-9.

(69) Lindahl, P. A., Munck, E., and Ragsdale, S. W. (1990) CO dehydrogenase from *Clostridium thermoaceticum*. EPR and electrochemical studies in CO_2 and argon atmospheres. *J. Biol. Chem*. *265*, 3873-9.

(70) Ma, K., Hutchins, A., Sung, S.-J. S., and Adams, M. W. W. (1997) Pyruvate ferredoxin oxidoreductase from the hyperthermophilic archaeon, *Pyrococcus furiosus*, functions as a CoA-dependent pyruvate decarboxylase. *Proc. Natl. Acad. Sci. U.S.A. 94*, 9608-9613.

(71) Furdui, C., and Ragsdale, S. W. (2002) The Roles of Coenzyme A in the Pyruvate:Ferredoxin Oxidoreductase Reaction Mechanism: Rate Enhancement of Electron Transfer from a Radical Intermediate to an Iron-Sulfur Cluster. *Biochemistry 41*, 9921-9937.

(72) Menon, S., and Ragsdale, S. W. (1997) Mechanism of the Clostridium thermoaceticum Pyruvate:Ferredoxin Oxidoreductase: Evidence for the Common Catalytic Intermediacy of the Hydroxyethylthiamine Pyropyrosphate Radical. *Biochemistry 36*, 8484-8494.

(73) Pieulle, L., Guigliarelli, B., Asso, M., Dole, F., Bernadac, A., and Hatchikian, E. C. (1995) Isolation and characterization of the pyruvate-ferredoxin oxidoreductase from the sulfate-reducing bacterium *Desulfovibrio africanus*. *Biochim. Biophys. Acta, Protein Struct. Mol. Enzymol. 1250*, 49-59.

(74) Cammack, R., Kerscher, L., and Oesterhelt, D. (1980) A stable free radical intermediate in the reaction of 2-oxoacid:ferredoxin oxidoreductases of *Halobacterium halobium*. *FEBS Lett.. 118*, 271-273.

(75) Chabrière, E., Vernède, X., Guigliarelli, B., Charon, M.-H., Hatchikian, E. C., and Fontecilla-Camps, J. C. (2001) Crystal Structure of the Free Radical Intermediate of Pyruvate:Ferredoxin Oxidoreductase. *Science 294*, 2559-2563.

(76) Mansoorabadi, S. O., Seravalli, J., Furdui, C., Krymov, V., Gerfen, G. J., Begley, T. P., Melnick, J., Ragsdale, S. W., and Reed, G. H. (2006) EPR Spectroscopic and Computational Characterization of the Hydroxyethylidene-Thiamine Pyrophosphate Radical Intermediate of Pyruvate:Ferredoxin Oxidoreductase. *Biochemistry 45*, 7122-7131.

(77) Tittmann, K., Wille, G., Golbik, R., Weidner, A., Ghisla, S., and Hübner, G. (2005) Radical Phosphate Transfer Mechanism for the Thiamin Diphosphate- and FAD-Dependent Pyruvate Oxidase from Lactobacillus plantarum. Kinetic Coupling of Intercofactor Electron Transfer with Phosphate Transfer to Acetyl-thiamin Diphosphate via a Transient FAD Semiquinone/Hydroxyethyl-ThDP Radical Pair. *Biochemistry 44*, 13291-13303.

CHAPTER II

Identification and Characterization of Oxalate Oxidoreductase, a Novel Thiamine Pyrophosphate-dependent 2-Oxoacid Oxidoreductase that Enables Anaerobic Growth on Oxalate[3]

2.1 Introduction

Moorella thermoacetica is a strictly anaerobic gram-positive acetogenic bacterium. Acetogens are commonly found in the soil, animal GI tract and the rumen that grows heterotrophically or autotrophically on many different electron donors. Electrons from these substrates are used to reduce CO_2 to acetate by the Wood-Ljungdahl pathway. During growth by this pathway, acetate and cell mass are the only growth products and electron-rich growth substrates like glucose are converted stoichiometrically to acetate; therefore *M. thermoacetica* is called a homoacetogen. *M. thermoacetica* can use other electron acceptors (e.g. nitrate, nitrite, thiosulfate, dimethyl sulfoxide). Under most conditions, nitrate reduction occurs preferentially to CO_2 reduction and nitrate has been shown to repress autotrophic growth (*1, 2*). However, oxalate is unique in its properties as an electron donor by *M. thermoacetica* for acetogenic growth. When both nitrate and

[3]The contents of this chapter were previously published: Pierce, E. A., Becker, D. F. and Ragsdale, S. W. (2010) Identification and Characterization of Oxalate Oxidoreductase, a Novel Thiamine Pyrophosphate-Dependent 2-Oxoacid Oxidoreductase that Enables Anaerobic Growth on Oxalate. *Journal of Biological Chemistry 285*, 40515-40524. The sedimentation equilibrium experiments were performed by Dr. Don Becker at the University of Nebraska - Lincoln.

CO_2 are provided to cells growing on oxalate, CO_2 is reduced to acetate during the exponential growth phase and nitrate is only used as the electron acceptor during stationary phase (*3*). Oxalate is the only substrate with which *M. thermoacetica* has been shown to reduce CO_2 instead of nitrate when both are present.

Oxalate ($C_2O_4^{2-}$) is the most oxidized two-carbon compound. It is made in high concentrations by some plants and fungi and can reach high micromolar concentrations in soil (*4*). Oxalate is toxic to mammals, but is metabolized by many bacteria and plants by various pathways. In *Oxalobacter formigenes*, oxalate is first activated to oxalyl-CoA, then decarboxylated, giving formyl-CoA and CO_2. Formyl-CoA transferase then exchanges the formyl group for an oxalyl-group on CoA, thus producing formate and regenerating oxalyl-CoA. Energy for growth on oxalate in *O. formigenes* results from a formate:oxalate antiporter, which generates an electrochemical transmembrane gradient for ATP synthesis (*5, 6*), so most formate produced is excreted rather than oxidized (*7*). Other organisms, such as *Cupriavidus oxalaticus*, also use oxalyl-CoA decarboxylase to metabolize oxalate, but use formate dehydrogenase to generate NADH with the electrons derived from oxalate (*8, 9*). Oxalyl-CoA decarboxylase is a TPP-dependent enzyme with distant homology to yeast pyruvate decarboxylases (*10*). The *M. thermoacetica* genome has sequences with low homology to oxalyl-CoA decarboxylase, but no homolog of formyl-CoA transferase. In fungi and in some bacteria, including *Bacillus subtilis*, oxalate can also be metabolized by oxalate decarboxylase, a manganese-containing cupin family protein, to generate formate and CO_2 (*11*). This reaction requires O_2. Another Mn^{2+}-cupin called germin that is found in plants catalyzes the oxidative decarboxylation

of oxalate in the reaction $C_2O_4^{2-} + 2H^+ + O_2 \rightarrow 2CO_2 + H_2O_2$ (*12*). No enzyme that catalyzes anaerobic oxalate oxidation has been previously reported.

During growth on oxalate, *M. thermoacetica* consumes four moles of oxalate to produce one mole of acetate and six moles of CO_2 (Eq. 1) (*13*). Two proteins (33 kDa and 42 kDa) were identified to be induced when *M. thermoacetica* was exposed to oxalate (*14*). Similarly, Daniel et al. found that oxalate-grown cells metabolize oxalate much more quickly than cells that had been grown on glucose, which is consistent with an oxalate induction mechanism (*15*). They also showed that cell extracts from oxalate-grown cells could catalyze oxalate-dependent benzyl viologen reduction, that this activity was only slightly stimulated by coenzyme A and that the electron acceptor specificity of oxalate oxidation was different than that of formate oxidation. They concluded that *M. thermoacetica* catabolizes oxalate by a CoA-independent mechanism that does not use formate as an intermediate.

$4\ C_2O_4^{-2} + 5\ H_2O \rightarrow CH_3COO^- + 6\ HCO_3^- + OH^-$ ($\Delta G = -41.4$ kJ/mol oxalate) (Eq 1)

In this paper, we show that the enzyme induced by oxalate, which we have named oxalate oxidoreductase (OOR), is a novel member of the family of thiamine pyrophosphate (TPP)-dependent 2-oxoacid:ferredoxin oxidoreductases that typically catalyze oxidative decarboxylation of α-ketoacids to produce CO_2 and acyl-coenzyme A products. Unlike all previously characterized members of this family, OOR does not use coenzyme A as a substrate. The protein responsible for oxalate oxidation in *M. thermoacetica* was purified to homogeneity and shown to be the only enzyme required to catalyze the conversion of oxalate to CO_2 (or bicarbonate) and two electrons. Thus,

coupling OOR to the Wood-Ljungdahl pathway allows anaerobic bacteria to generate energy by oxidizing oxalate, producing reducing equivalents to drive acetate formation.

2.2 Experimental Procedures

2.2.1 *Culture media and growth conditions*

M. thermoacetica ATCC 39073 was grown at 55 ^{o}C in stoppered, crimp-sealed 120 mL serum bottles pressurized with pure CO_2 and containing 100 mL medium, or in a 10 L fermentor that was continually bubbled with CO_2 during growth. The medium was modified from the "undefined medium" of Lundie and Drake (*16*) and contained 5 g L^{-1} yeast extract, 5 g L^{-1} tryptone, 0.1 mM $Fe(NH_4)_2(SO_4)_2$, 4.4 mM sodium thioglycolate, 7.6 mM $(NH_4)_2SO_4$, 1.0 mM $MgSO_4$, 0.2 mM $CaCl_2$, 0.1 mM $CoCl_2$, 20 µM $NiCl_2$, 6.8 mM NaCl, 0.1 mM nitrilotriacetic acid, 5 µM $ZnCl_2$, 7 µM Na_2SeO_3, 3 µM Na_2WO_4, 25 µM Na_2MoO_4, 25 µM $MnCl_2$, 2.4 µM H_3BO_2 and 0.3 µM $KAl(SO_4)_2$ (solution A), 20 mM K_2HPO_4, 100 mM $NaHCO_3$ and 20 mM KH_2PO_4 (solution B). Solutions A and B were autoclaved separately, combined after cooling and sparged with CO_2. Before inoculation, the medium was supplemented with glucose (100 mM in 100 mL cultures, 20 mM in the fermentor) and/or oxalate (27 mM), a vitamin solution (*16*) and 10 mL L^{-1} of reducing solution (36 g L^{-1} each of $Na_2S{\cdot}9H_2O$ and cysteine-HCl). Cells were harvested during exponential growth by centrifugation under CO_2 or N_2 and were stored at -80^{o}C until use.

2.2.2 *Two-dimensional gel electrophoresis*

For two-dimensional gel electrophoresis, proteins were extracted with phenol as described (*17*), except that instead of tissue grinding, sonication was used to break the cells and, after precipitation of proteins in methanol, the protein pellet was washed twice with ice cold acetone (80% in water) and once with ice cold ethanol (70% in water). After washing, the protein pellets were suspended in 8 M urea, 2 M thiourea, 2% (w/v) CHAPS, 2% (w/v) triton X-100 and 50 mM dithiothreitol (DTT) to ~ 1 µg protein μL^{-1}. Samples (150 µL) were supplemented with Bio-Lyte ampholytes (BioRad) and loaded on 7 cm BioRad isoelectric focusing (IEF) gel strips (gradient from pH 5-8). The gels were subjected to 12 hours rehydration at 50 V, followed by focusing at 250 volts for 15 minutes and then at 4000 V for 35,000 volt-hours. After isoelectric focusing, the IEF gel strips were soaked in 6 M urea, 2% (w/v) SDS, 0.375 M Tris-HCl, pH 8.8, 20 % (w/v) glycerol and 20 mg/mL DTT for fifteen minutes, followed by incubation for fifteen minutes in the same buffer, but with 25 mg/mL iodoacetamide instead of DTT. Strips were rinsed in running buffer before loading them at the top of 12.5% acrylamide gels for SDS-PAGE. After SDS-PAGE, proteins were stained with Coomassie blue. Spots were cut from the gels and proteins were identified by mass spectrometry at the University of Michigan Protein Structure Facility. A blank spot of each gel was also taken and processed. The samples were subjected to in-gel Trypsin digestion. As a control, BSA was run on a separate gel and subjected to the same digestion and Mass Spectrometry procedure. LC-MS/MS was performed on a Q-TOF Premier Mass Spectrometer. Protein Lynx Global Server and Mascot search engines were used to search the SwissProt and NCBI databases.

2.2.3 *Purification of OOR*

Protein was purified from *M. thermoacetica* cells grown in the fermentor on glucose and oxalate. All purification steps and subsequent enzymatic manipulations were done in a Vacuum Atmospheres (Hawthorne, CA) anaerobic chamber maintained at $\leq$ 4 ppm O_2. Cells were suspended in Buffer A (50 mM Tris-HCl, 2 mM $MgCl_2$, 2 mM DTT, 1 mM TPP, pH 7.9) with 0.25 mg/mL lysozyme and 0.2 mM phenylmethanesulfonyl fluoride, sonicated and centrifuged at 4 ^{o}C at 100,000 x *g* for 1 hour. The supernatant was loaded on a 5 x 25 cm DEAE cellulose column and proteins were eluted with a gradient from 0.1 M to 0.5 M in Buffer A. The 0.3 M fraction was diluted to 0.075 M NaCl with Buffer A and loaded on a 2.5 x 25 cm red agarose (Sigma Aldrich) column. OOR did not bind to this column, so 0.85 M ammonium sulfate was added to the flow-through and wash fractions and these were loaded on a 2.5 x 25 cm fast-flow high substitution phenyl sepharose (G.E. Healthcare) column and eluted with a reverse linear gradient from 0.85 M to 0 M ammonium sulfate and 10 percent glycerol in Buffer A. Oxalate oxidation activity eluted at around 0.45 M ammonium sulfate. Fractions containing OOR activity were pooled, concentrated and exchanged into Buffer A using 30 kDa molecular weight cut-off centrifuge concentrators. The protein was loaded on a 2.5 x 25 cm high performance Q sepharose column (Sigma-Aldrich) and eluted with a linear gradient from 0-0.7 M NaCl in Buffer A. OOR activity eluted at 0.47 M NaCl. Fractions containing OOR activity were pooled and exchanged into 50 mM Tris-HCl, pH 7.9, and 2 mM DTT. OOR was stored in 50 mM Tris-HCl, pH 7.9, and 2 mM DTT at a concentration of 210 µM and dilutions of this protein stock were used for all subsequent experiments, unless described otherwise.

2.2.4 *Enzyme assays*

OOR activity was measured in 50 mM Tris-HCl, 2 mM DTT, pH 7.9. Assays at 25 ^{o}C were done in a Vacuum Atmospheres anaerobic chamber maintained at $\leq$ 4 ppm O_2, using a UV-visible spectrophotometer from Ocean Optics (Dunedin, FL). Assays at 40 or 55 ^{o}C were performed in stoppered cuvettes flushed with N_2 gas, in an OLIS (Bogart, GA)-modified Cary-14 spectrophotometer. For steady-state assays performed with saturating substrate concentrations, 1 mM sodium oxalate and 10 mM methyl viologen were used and the reduction of methyl viologen was followed at 578 nm (ε_{578} = 9.7 mM^{-1} cm^{-1}). In assays using ferredoxin ($\Delta\varepsilon_{420}$ = 7.5 mM^{-1} cm^{-1}), horse heart cytochrome c ($\Delta\varepsilon_{553}$ = 19.4 mM^{-1} cm^{-1}), NAD^+ or $NADP^+$ (ε_{340} = 6.22 mM^{-1} cm^{-1}), FMN (ε_{450} = 12.2 mM^{-1} cm^{-1}), FAD (ε_{450} = 11.3 mM^{-1} cm^{-1}), or CODH, methyl viologen was omitted. The extinction coefficients for FMN and FAD are for two-electron reductions. $\Delta\varepsilon_{320}$ for metronidazole was determined by titrating 100 µM metronidazole with 20 µM aliquots of oxalate, in the presence of 1.8 µM OOR ($\Delta\varepsilon_{320}$ = 3.2 (mM reducing equivalent)$^{-1}$ cm^{-1}) at 320 nm was determined. In all assays, calculations were based on the assumption that oxidation of one mole of oxalate produces two moles of electrons. CODH as an electron acceptor for OOR was assayed in 50 mM sodium phosphate, pH 7.0, with 1 mM oxalate, 20 µM CODH/ACS from *M. thermoacetica* and 50 µM myoglobin in stoppered cuvettes that were flushed with 20% CO_2/80% N_2 (6.8 mM CO_2 in solution). The stock solution of myoglobin was pre-reduced by adding a stoichiometric amount of sodium dithionite. Formation of CO from CO_2 was measured as myoglobin-bound CO. At pH 7, the specific activity of CO_2 reduction by CODH using dithionite (instead of OOR) as a reductant was 4.7 µmoles min^{-1} µmole $CODH^{-1}$. Formation of Mb-

CO was monitored at 423 nm. The extinction coefficient, $\Delta\varepsilon_{423}$ = 129 mM^{-1} cm^{-1}, was determined from the difference between the spectra of myoglobin-CO and dithionite-reduced myoglobin. The concentration of myoglobin used for these spectra was determined from extinction coefficients of 121 mM^{-1} cm^{-1} at 435 nm for ferrous myoglobin and 207 mM^{-1} cm^{-1} at 423 nm for myoglobin-CO (*18*).

For whole cell assays, cells were harvested from growing cultures, washed twice with 15 mM NaCl in 50 mM potassium phosphate, pH 7.0, and re-suspended in stoppered serum bottles in fresh growth medium with 10 mM oxalate and 1 atmosphere of CO_2. Aliquots were removed with a syringe, quenched in 1 M HCl and oxalate concentrations were measured by HPLC on a 300 x 7.8 mm BioRad Aminex HPX-87H column with a mobile phase of 0.008 N H_2SO_4 in a Beckman Coulter (Brea, CA) System Gold HPLC with diode array UV-visible detector. Oxalate was detected by its absorbance at 210 nm. Concentrations were determined by comparison to oxalate standards prepared in the medium used for the assays. Oxalate concentrations between 0.25 and 10 mM could be reliably determined by this assay. HPLC-based assays with purified protein or cell extracts were performed in the same way, except that 50 mM Tris-HCl, pH 8.0, with 10 mM oxalate and 10 mM methyl viologen (under an N_2 atmosphere) was used instead of growth medium and oxalate standards were prepared in the assay buffer.

The pH dependence of OOR activity was determined by measuring activity with 1 mM oxalate and 10 mM methyl viologen in 50 mM buffer containing 2 mM DTT. Buffers were made by mixing 50 mM solutions of conjugate acid and base in different proportions and the pH of each buffer and DTT solution was measured before starting each assay. The buffers used were MES (pKa = 6.02, used from pH 5.0-7.1), sodium

phosphate (pKa = 6.82, used from pH 5.9-7.8), borate (pKa = 8.94, used from pH 8.1-9.1) and CAPSO (pKa = 9.42, used from pH 8.4-10.2).

2.2.5 *UV-visible spectroscopy*

OOR was diluted to 4.1 μM in 50 mM Tris-HCl, pH 7.9, and 2 mM DTT to measure the UV-visible spectrum of the as-isolated protein. The enzyme was reduced at 25 ^{o}C by adding 100 μM sodium oxalate. To measure the spectrum of the oxidized protein, 4.1 μM OOR was mixed with 50 nM *M. thermoacetica* CODH/ACS in 50 mM potassium phosphate, pH 7.0. The cuvette containing this mixture was stoppered and the headspace was flushed with 20% CO_2/80% N_2. After five minutes of CO_2 exposure, the spectrum was recorded. In this reaction, electrons from OOR are transferred to CODH, which reduces the CO_2 to CO. Once OOR was fully oxidized, the spectrum did not change during another hour of CO_2 exposure.

2.2.6 *EPR spectroscopy*

OOR was concentrated and diluted in 50 mM Tris-HCl, pH 8.0 (without DTT), to a concentration of 49 μM. Comparison of the UV-visible spectrum of this protein with dithionite-reduced OOR showed that the protein was two-thirds reduced. Sodium oxalate (50 μM, final) was added to completely reduce the protein. After reduction, different amounts of horse heart cytochrome c and 50 mM Tris-HCl, pH 8.0, were added to generate samples that were 39 μM OOR and between 20 and 160 μM cytochrome c. EPR spectra were collected at 9 K and the parameters were as follows: receiver gain, 2 x 10^2; modulation frequency, 100 kHz; modulation amplitude, 10 G; center field, 3450 or 3500

G; sweep width, 700 or 2000 G; and microwave power, 0.129 mW. The double integrals of the EPR signals were compared to that of a 1 mM copper(II) perchlorate standard to determine the number of spins per monomeric unit.

2.2.7 *Size exclusion chromatography*

A 90 x 1.6 cm column of Superdex 200 resin (G. E. Healthcare) was equilibrated with an anaerobically prepared solution of 50 mM Tris-HCl, pH 8.1 with 2 mM DTT, 0.2 mM $Na_2S_2O_4$ and 0.5 mM sodium oxalate. The buffer was added to the column through a continuous closed system of tubing, and the bottle containing the buffer was closed by a rubber stopper and pressurized with N_2 gas during use, to keep O_2 from entering the buffer and column. Proteins were dissolved in the same buffer anaerobically, removed from the anaerobic chamber in stoppered serum vials, and added to the column sample loop with a Hamilton gas-tight syringe. Blue dextran, a standard protein mixture consisting of carbonic anhydrase (29 kDa), bovine serum albumin (66 kDa), alcohol dehydrogenase (150 kDa), β-amylase (200 kDa), apoferritin (443 kDa) and thyroglobulin (669 kDa), OOR and *M. thermoacetica* pyruvate ferredoxin oxidoreductase were run separately over the column. Blue dextran and standard proteins were purchased from Sigma Aldrich.

2.2.8 *Sedimentation equilibrium*

The oligomeric state of OOR was determined at 20 ^{o}C by sedimentation equilibrium under anaerobic conditions using an Optima XL-I analytical ultracentrifuge (Beckman Coulter, Inc.) equipped with an eight-hole An50 Ti rotor. OOR was dialyzed

against 50 mM Tris-sulfate buffer (pH 8.0) containing 2 mM DTT and 100 mM NaCl before centrifugation. Sample and reference cells were incubated overnight in an anaerobic glove box (nitrogen atmosphere, Belle Technology) prior to loading with reference buffer and OOR samples. Three concentrations (8.3, 21, and 32 μM) of OOR were loaded (110 μl) in the sample cells and the reference cells were filled with the dialyzate buffer (125 μl). Radial scans were collected at 430, 460, and 470 nm after 22 h and 24 h using a rotor speed of 6,000 rpm. The scans are an average of 10 measurements at each radial position with a spacing of 0.001 cm. Data were fit by global analysis to an equation describing a single-species model using Origin 6.0. The partial specific volume of OOR used for best-fit analysis was 0.7396, which is the average of the three OOR polypeptides calculated by SedTerp. The solvent density of the buffer was calculated to be 1.0038 g/ml.

2.2.9 *Miscellaneous methods*

The stoichiometry of the three OOR peptides was estimated from a Coomassie-stained SDS polyacrylamide gel of the purified protein. To find the relative amounts of the three bands, the gel was scanned and digitized using UN-SCAN-IT gel Version 6.1 software from Silk Scientific (Orem, UT). Blue native polyacrylamide gel electrophoresis was done with the Invitrogen NativePAGE Novex Bis-Tris Gel System, using 4-16% acrylamide gradient gels, and NativeMark protein standards. OOR and PFOR proteins were mixed with 0.5% Coomassie G-250 before loading gels. Protein concentrations were determined by the Rose Bengal method (*19*), using a lysozyme standard. The concentration of TPP bound to OOR was determined by a fluorescent thiochrome assay

(*20*). Pure TPP was used as a standard. Metal concentrations were determined by ICP-OES at the Chemical Analysis Laboratory at the University of Georgia. For metal analysis, 1.1 mL of 20 μM OOR was dialyzed against two changes of 500 mL of 100 mM Tris-HCl, 2 mM DTT, pH 7.9. Metal concentrations in the protein sample were calculated after subtracting the concentrations in a sample of the dialysis buffer treated exactly as was the protein.

2.3 Results

2.3.1 *Identification of proteins induced during growth of M. thermoacetica on oxalate*

Daniel and Drake showed by SDS-PAGE that 33 kDa and 42 kDa proteins are induced during growth of *M. thermoacetica* on oxalate (*14*). Cell extracts from cells grown with different substrates, SDS-PAGE (Figure 2.1, lanes 2-3) and two-dimensional electrophoresis (Figure 2.2) experiments reveal three proteins (with molecular masses of 42, 39 and 35 kDa) that are more strongly expressed in cells grown in stoppered culture flasks on oxalate or on oxalate and glucose than those grown on glucose (in the absence of oxalate). These three proteins were identified by mass spectrometry as the subunits of an annotated 2-oxoacid:ferredoxin oxidoreductase, with NCBI accession numbers of YP_430440, YP_430441 and YP_430442 and Joint Genome Institute locus tag classifications Moth_1593, Moth_1592 and Moth_1591, respectively (*21*) (Table 2.1). Directly upstream from Moth_1593 are two genes that are transcribed in the same direction, which encode a transcriptional regulator (Moth_1595) and an AAA family ATPase in the CDC48 subfamily (Moth_1594). The N-terminal domain of the predicted

transcriptional regulator is annotated as a GntR family helix-turn-helix pfam domain and the C-terminal domain is annotated as an FCD ligand-binding domain. Moth_1590, downstream from Moth_1591, encodes a major facilitator superfamily protein with thirty-five percent sequence identity to the oxalate:formate antiporter of *Oxalobacter formigenes* (*22*) (Figure 2.3).

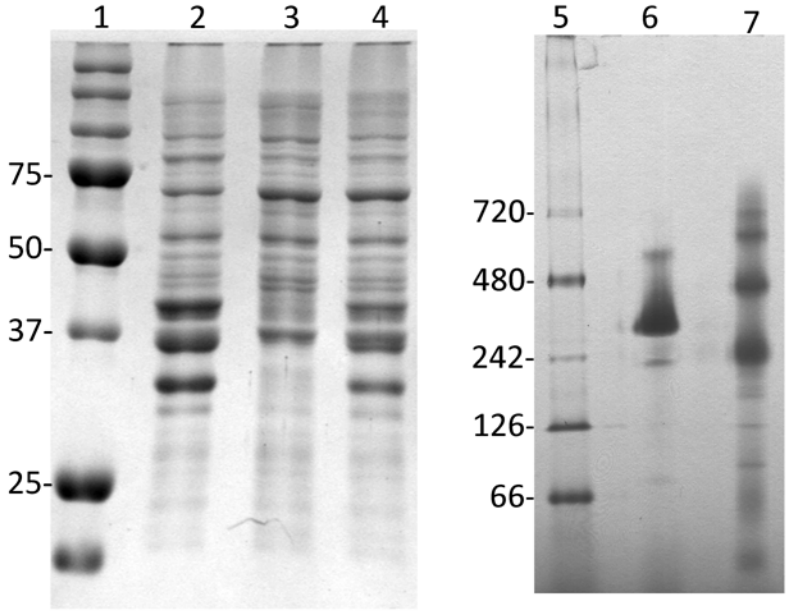

Figure 2.1. Native PAGE of purified OOR and SDS PAGE of *M. thermoacetica* cell extracts. Lanes 1-3, SDS-PAGE. Lane 1: molecular mass marker; Lane 2: total cell protein from *M. thermoacetica* grown on 28 mM oxalate and 50 mM glucose; Lane 3: total cell protein from *M. thermoacetica* grown on 50 mM glucose. Lanes 4-6, native PAGE. Lane 4: molecular mass marker; Lane 5: 10 µg *M. thermoacetica* PFOR; Lane 6: 10 µg oxalate oxidoreductase.

Table 2.1. Mass spectrometric identification of oxalate oxidoreductase

Spot	NCBI accession number	JGI locus tag	Percent sequence coverage	Number of peptides identified by LC-MS/MS
1	YP_430442	Moth_1593	58	26
2	YP_430441	Moth_1592	80	40
3	YP_429140	Moth_0262	29	10
4	YP_430440	Moth_1591	48	18
5	YP_429140	Moth_0262	50	17

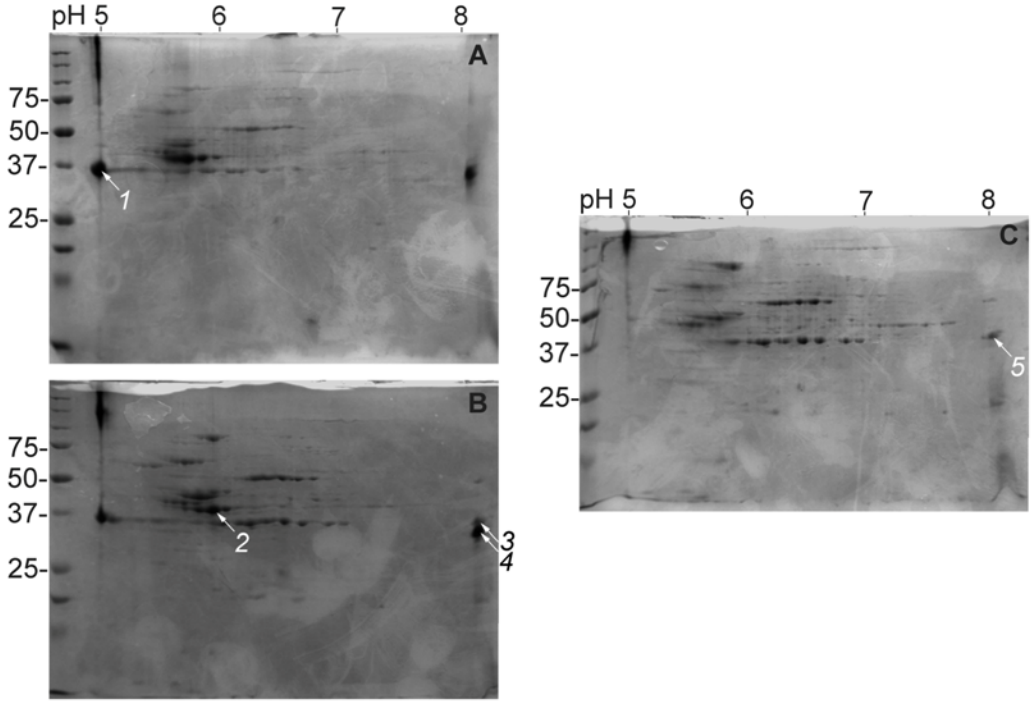

Figure 2.2. Two dimensional electrophoresis used to identify oxalate oxidoreductase in cell extracts. Molecular mass markers are visible at the left side of each gel. Cells were grown on CO_2 and A, oxalate; B, glucose and oxalate; C, glucose. Arrows point to the spots identified by mass spectrometry. The best match from the most predominant protein in each sample is listed in Table 2.1. Spots 1 and 2 were identified as the fusion of gamma and delta subunits and the alpha subunit of oxalate oxidoreductase. Two spots in A and B that are not well resolved (marked as 3 and 4) are in the same position as a protein spot in C (marked as 5). Spots 3 and 5 were identified as glyceraldehyde-3-phosphate dehydrogenase. Spot 4 was identified as the beta subunit of OOR. No peptides from this protein were identified in spot 5 from the gel from glucose-grown cells.

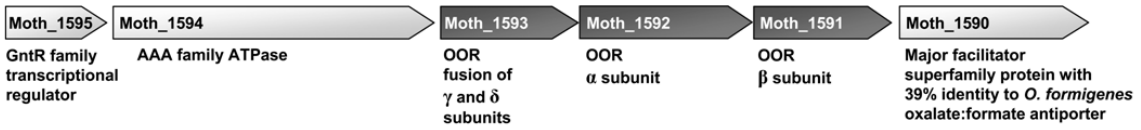

Figure 2.3. Gene cluster containing genes encoding OOR. Only the products of genes shown in dark grey were identified by 2-D electrophoresis and mass spectrometry as being highly expressed during growth on oxalate.

2.3.2 *Purification of oxalate degrading activity from M. thermoacetica*

As shown earlier (*15*), we found that cell extracts containing soluble protein from *M. thermoacetica* grown on oxalate and glucose catalyzed oxalate-dependent reduction of methyl viologen. Based on an HPLC-based assay that measures the decrease in oxalate concentration, the OOR specific activity was 0.4 μmoles min^{-1} mg $protein^{-1}$ at 55 ^{o}C, while that of extracts from cells grown on glucose without oxalate was less than 0.03 μmoles min^{-1} mg $protein^{-1}$ at 55 ^{o}C. We also used the HPLC-based assay to measure oxalate degradation by whole cells of *M. thermoacetica* grown on oxalate and glucose or on glucose alone. In these assays, which were followed for several hours, oxalate was degraded thirty times more quickly by cells that had been previously exposed to oxalate than by cells grown on glucose without oxalate.

To determine if the 2-oxoacid:ferredoxin oxidoreductase homolog that is overexpressed during growth on oxalate is the only protein needed for the oxalate-dependent methyl viologen reducing activity seen in cell extracts, we purified OOR from *M. thermoacetica* cells to greater than 95% purity, as shown by SDS-PAGE (Figure 2.4, Table 2.2). After 22-fold purification, the active protein consisted of three peptides in 1:0.8:1 stoichiometry, with estimated sizes of 36, 43 and 32 kDa, which corresponds well to the predicted masses of 34.2, 43.7 and 33.9 kDa for YP_430440, YP_430441 and YP_430442.

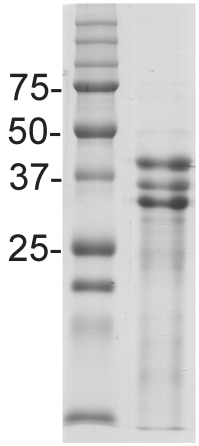

Figure 2.4. SDS-PAGE of purified OOR. Left lane, molecular mass marker (sizes shown in kDa); right lane, 6 μg of purified OOR.

Table 2.2. Purification of OOR

Purification step	U/mg[a]	mg protein	Total units	Purification (fold)
Cell-free extract	0.009	3780	34	1
DEAE cellulose	0.044	1590	70	5
Phenyl sepharose	0.169	349	54	18
Q sepharose	0.200	108	22	22

[a]Measured at 40°C

The purified OOR preparation retained 0.015 U/mg of CO dehydrogenase (CODH) activity, indicating that there is a 0.03% contamination of OOR with CODH/acetyl-CoA synthase (ACS), which apparently was not completely separated from OOR during the purification procedure.

When run on Blue native polyacrylamide gel electrophoresis, most of the OOR was found in a major band with an estimated molecular mass of 243 kDa and another species with a mass of 445 kDa (Figure 2.1). Molecular exclusion chromatographic analysis of OOR reveals predominantly a 236 kDa species and a 117 kDa species, which accounts for 10-20% of the total protein (Figure 2.5). In a parallel gel filtration

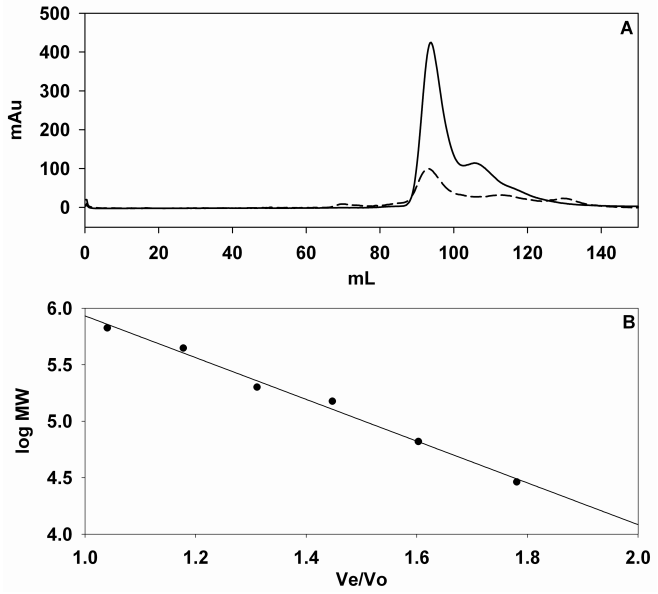

Figure 2.5. Size exclusion chromatography of purified OOR and PFOR. A, elution of OOR (solid line) and pyruvate:ferredoxin oxidoreductase (dashed line) from the column. Elution was monitored by absorbance at 280 nm. B, standard curve used to calculate approximate molecular weights of OOR and PFOR. Ve/Vo is the ratio of the elution volume of each protein standard to the void volume of the column, determined using blue dextran.

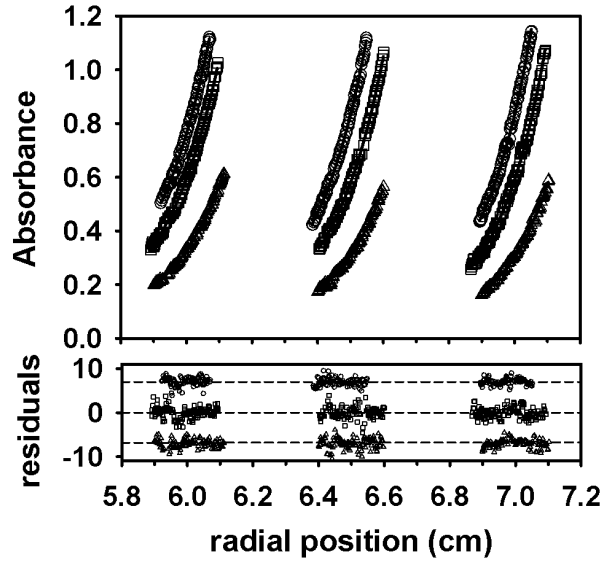

Figure 2.6. Sedimentation equilibrium analysis of OOR. The top panel shows a global fit of analytical ultracentrifugation data for three different concentrations of OOR collected at 6000 rpm. Absorbance data were recorded at 430, 460, and 470 nm for 8.3 μM (triangles), 20.7 μM (squares), and 32.3 μM (circles) OOR concentrations, respectively. The solid line through the points is the weighted best least squares fit to an ideal single-species model. Residuals for each fit are shown in the bottom panel. A vertical offset was applied to the residuals from the 8.3 μM (triangles) and 32.3 μM (circles) concentrations for clarity.

experiment, the *M. thermoacetica* PFOR was shown to elute with a similar profile. The quaternary structure of OOR was also characterized by analytical ultracentrifugation. (Figure 2.6) shows the results from sedimentation equilibrium analysis of OOR at three different concentrations. A best-fit value of 226,890 Da was estimated for the molecular weight of OOR which is within 1.5% of the molecular weight predicted for a dimeric species (223,700 Da). These combined results indicate that, like PFOR and other OFORs, OOR forms a dimeric structure consisting of two heterotrimeric units.

2.3.3 *Sequence analysis of OOR*

2-Oxoacid:ferredoxin oxidoreductases are made up of a minimum of three conserved domains, alpha, beta and gamma, with an additional delta domain in most OFORs. The genomic arrangement and fusion of these domains varies. The residues involved in binding TPP and one $[Fe_4S_4]^{2+/1+}$ cluster are in the beta subunit (*23*).

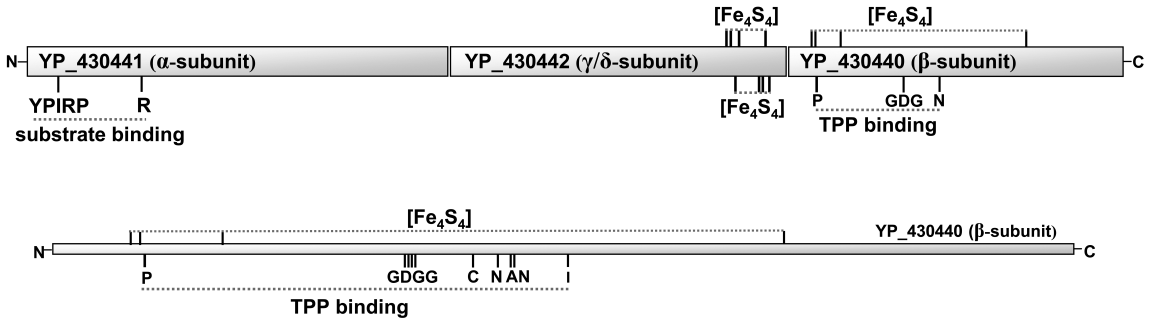

Figure 2.7. Schematic of OOR peptides. Top, arrangement of the three peptide sequences as they align with pyruvate:ferredoxin oxidoreductases from *D. africanus* and *M. thermoacetica*. Each rectangle represents a separate gene product. Locations of conserved residues that may be involved in iron-sulfur cluster, TPP, Mg^{2+}, and substrate binding are shown (Mg^{2+} binding residues include the $GDGX_{32}N$ motif in the β subunit). All residues proposed to ligate the Fe_4S_4 clusters are cysteines. Bottom, expanded view of the β subunit of OOR showing both conserved and non-conserved residues that align with the Fe_4S_4 cluster and TPP-binding residues of *D. africanus* PFOR.

```
Moth_oor   22 VDVICSYPIRPYTGIMSELAR 42     90  SGERLPVQMAIADRTLD-PPGDFGEEHT 131
Mt_por     21 PKVIPVYPITPQTSISEYLAK 41     89  AGLRNPIVMANANRALS-APLSIWNDQQ 130
Pf_por     22 PKVIAAFPITPSTLIPEKISE 42     90  AGMRLPIVMAIGNRALS-APINIWNDWQ 131
Pf_vor     25 VQVVAAYPITPQTSIIEKIAE 45     90  AGARLPIVMVDVNRAMA-PPWSVWDDQT 131
Moth_0378  22 VQVISAYPITPQSPIAEKLAE 42     90  SGCRVPIVMAVINRSLV-SPWSLWCDHQ 131
Moth_1922  20 AEVVAAYPITPQSTIVEKIAE 40     88  SGCRVPLVMAVANRGLA-APWTIWADHQ 129
Hp_por     28 IDVIAAYPITPSTPIVQNYGS 48     96  SGMRLPIVLNLVNRALA-APLNIHGDHS 137
Eh_por     18 SDVSFIFPITPSSPMAENADV 38     91  AGEHLPCVFHVTARALAGQALSIFGDHS 132
Moth_por   20 SEVATIYPITPSSPMAEIADE 40     93  AGELLPCVFHVAARALSTHALSIFGDHA 134
Da_por     22 SEVAAIYPITPSSTMGEEADD 42     95  SGELLPGVFHVTARAIAAHALSIFGDHQ 136
Tt_por     22 TEVAAIYPITPSSPMAELVDA 42     95  AGELLPGVFHVSARAVATHALSIFGDHS 136
Am_por     22 TDVAAIYPITPSSNMAENVDE 42     95  AGELLPGVFHVSARALAGHALSIFGDHS 136
Ht_por     48 VDASVSYPITPQSEAAHLIGE 68    115  AGTRIPVQLVLMARGVN-APLSIQPDNL 156
Ht_kor1    38 VDIAIAYPITPQSEVMHLVGD 58    105  PGHRIPAVLGVLTRVVN-APLSIQPDNV 146
Moth_0033  28 ADIMYGYPITPQNEIMHYWTR 48     94  EMMRLPTVVVVTQRGGPST-ATVIYSQQ 136
Mt_vor     16 CDCYFGYPITPASEILHEASR 36     92  AGAELPAVIVDVMRAGP-GLGNIGPEQG 135
Moth_1984  20 CRVFAGYPITPATEIAENMAR 40     87  ISSEIPLVIVNSQRVGPVVSGITGPGQG 129
Hp_kor     20 CRFFGGYPITPSSDIMHAMSV 40     97  FMAEIPLVIADVMRSGPSTGMPTRVAQG 138
Mt_kor     23 CRFFAGYPITPSTEIAEEMAL 43     90  AMTETPLVIVNVQRGSPSSTGQPTASQS 131
Hs_u      237 CRFISGYPMTPWTDAFTIMTQ 257   304  EMTETPLVLLEAQRAGPSTGMPTKPEQA 345
Ht_kor2   215 CKFYAAYPITPATTVGNYIVE 235   282  GMTELPIVIVDVQRVGPATGMPTKHEQG 323
Ta_kor    218 VRFVAAYPITPGTEVLEWLAP 238   285  VASETPITIVNVMRGGPSTGIPVKSEQS 326
Hs_kor    216 CRFYAGYPITPATDVMEYLTG 236   283  ATSETPLVIANVMRSGPSTGMPTKQEQG 324
Ap_u1     260 VRYQAYYPITPASDESVLLEE 280   333  GKNDVPMVITYYQRGGPSTGLPTRGSQS 374
St_u      247 VRFQSYYPITPASDESVYIEA 267   325  GMNEVPVVITYYIRGGPSTGLPTRTAQS 366
Ap_u2     257 LGVITYYPITPSSDEALYVEK 277   337  VEAEIPVVVTLWMRAGPSTGMPTRTGQQ 378
Mt_ior     32 VGVASTYPGTPSSEIGNVLSG 52     93  AYTGVRAGMVVLTADDP-SMFSSQNEQD 134
Pf_ior     34 IAVFAAYPGTPSSEVTDTMAA 54     95  SYMGVNGGFIVMVADDP-SMWSSQNEQD 136
```

Figure 2.8. Alignments of 2-oxoacid:ferredoxin oxidoreductase sequences. Alpha subunit sequences of pyruvate (por), 2-oxoisovalerate (vor), 2-oxoglutarate (kor) and indolepyruvate (ior) ferredoxin oxidoreductases, broad specificity 2-oxoacid:ferredoxin oxidoreductases (u) and four putative 2-oxoacid oxidoreductases from M. thermoacetica were aligned with the oxalate oxidoreductase alpha subunit (oor) using clustal W. The conserved YPITP substrate binding motif and arginine residue that bind pyruvate in the *D. africanus* PFOR crystal structure are highlighted. Species and NCBI sequence accession numbers are Moth: *M. thermoacetica* YP_430441 (oor), YP_428946 (por), YP_429255 (Moth_0378), YP_430765 (Moth_1922), YP_428916 (Moth_0033) and YP_430825 (Moth_1984); Mt: *Methanobacterium thermoautotrophicum* delta H (*24*) NP_276849 (por), O26800 (vor), NP_276168 (kor), and NP_276958 (ior); Pf: *Pyrococcus furiosus* (*25, 26*) NP_578695 (por), NP_578698 (vor) and NP_578262 (ior); Hp: *Helicobacter pylori* (*27*) NP_207901 (por) and NP_207384 (kor); Eh: *Entamoeba histolytica* (*28*) AAB49653; Da: *Desulfovibrio africanus* (*29*) CAA70873; Ta: *Thermoanaerobacter tengcongensis* NP_622125; Am: *Alkaliphilus metalliredigens* YP_001322386; Ht: *Hydrogenobacter thermophilus* (*30*) BAA95605 (por), BAI69553 (kor1) and BAI69551 (kor2); Hs: *Halobacterium salinarum* (*31*) YP_001689139 (u) and NP_279533 (kor); Ta: *Thauera aromatica* (*32*) CAD27440; Ap: *Aeropyrum pernix* (*33*) NP_148403 (u1) and NP_147967 (u2); St: *Sulfolobus tokodaii* (*34*) NP_378302.

Enzymes that include the delta subunit have two additional $[Fe_4S_4]^{2+/1+}$ clusters that are involved in electron transfer from the TPP active site to ferredoxin (*24*). The OOR protein is made up of separate α and β subunits and a third subunit that is a fusion of γ and δ domains (Figure 2.7). We performed separate clustalW alignments of the sequences

of the three OOR subunits with those of corresponding subunits of biochemically characterized pyruvate, 2-oxoisovalerate, 2-oxoglutarate, indolepyruvate and broad specificity oxidoreductases (see caption to Figure 2.8). The chosen sequences included the *D. africanus* PFOR, which has been crystallized in complex with pyruvate (*29*), allowing us to determine whether or not oxoacid binding residues are conserved in OOR. In the beta subunit, residues that coordinate TPP, the adjacent Mg^{2+} ion, and the $[Fe_4S_4]$ cluster that is nearest TPP are conserved. The eight cysteine residues that bind the other two $[Fe_4S_4]$ clusters are conserved in the OOR delta subunit.

In the alpha and beta subunits, two of five substrate-binding residues from *D. africanus* PFOR are conserved in OOR. Arg109 corresponds to Arg114 in *D. africanus* PFOR, which binds the carboxyl group of pyruvate. Three other residues, I123, I843 and N996 are less strongly conserved among the other OFORS. In the *D. africanus* PFOR structure, Asn996 forms a hydrogen bond to the carbonyl group and Ile843 and Ile123 interact with the methyl group of pyruvate. The corresponding residues are Asn143, and Val55 in the beta subunit and Phe117 in the alpha subunit of OOR. The fifth residue, Thr31 in PFOR, is part of a strongly conserved YPITP motif that is present in OFORs using many different substrates (*35*) and is within hydrogen bonding distance of the alpha-keto oxygen of pyruvate in the *D. africanus* PFOR crystal structure. This Thr is replaced by Arg in the OOR sequence (Figure 2.8), thus forming a YPIRP motif. A BLAST search of the non-redundant protein database at NCBI shows that this substitution is rare - eight of the eleven sequences most closely related to OOR have T31 replaced with arginine, but no other sequence in the first five hundred BLAST hits have arginine in this position.

2.3.4 *Cofactor binding*

OOR was purified in buffer containing 1 mM TPP and 2 mM $MgCl_2$ and, during the purification, the protein was assayed in the same buffer. After purification, the protein was exchanged into 50 mM Tris-HCl with 2 mM DTT, but without TPP or $MgCl_2$. The activity of the protein did not change after buffer exchange and we found that it was not necessary to add TPP to assays to see full activity. Using a fluorescent assay to quantify thiochrome bound to OOR, 1.0 mole of TPP was found per mole of protein.

As-isolated OOR is brown; metal analysis by ICP showed 14 moles of iron and 0.8 moles of Mg^{2+} per OOR monomer (calculated from the predicted value of 113.5 kDa per monomer, with concentrations of OOR estimated by Rose Bengal assays). After preparing the protein for metal analysis by dialysis into metal-free buffer, the protein retained activity with 0.7 mole TPP per mole of protein. Mg^{2+} is likely to help with TPP binding as it does in other TPP-dependent enzymes. Calcium, sodium and potassium were also present in the sample in greater than stoichiometric amounts, but their concentrations varied widely between two metal analysis samples, so it is possible that they bind non-specifically to the protein (Table 2.3).

Table 2.3. Cofactor content of OOR

Metal or co-factor	Mole/mol protein	
	As-isolated OOR	Dialyzed OOR
TPP	1.03	0.71
iron	14.0	14.3
magnesium	1.9	0.8
sodium	24.3	6.1
potassium	1.0	8.3
calcium	0.6	1.8

2.3.5 *Catalytic properties of OOR*

The purified heterotrimeric protein catalyzed the oxidation of oxalate using methyl viologen as an electron acceptor with a specific activity of 0.05 μmoles min^{-1} mg^{-1} (k_{cat} = 0.095 s^{-1}, at pH 7.9) and a K_m for oxalate of 58 ± 6 μM (Figure 2.9). Addition of CoA from 1 μM to 1 mM had no effect on the OOR reaction rate (Figure 2.9). Furthermore, the addition of 1 mM ATP and 1 mM CoA together to the assay mixture did not affect the rate of the reaction. The pH dependence of OOR activity was measured at pH values between 5.0 and 10.2 using saturating concentrations of oxalate (1 mM). The maximum activity (0.11 U/mg, 0.21 s^{-1}) was observed at pH 8.7 (Figure 2.9). Other reported optimal pH values for activity of 2-oxoacid:Fd oxidoreductases are between pH 7.5 and 9.0 (*31, 33, 36-40*). Since the pKa values for oxalate are 1.23 and 4.19 (*41*), the fully deprotonated form would be the substrate at the optimal pH for OOR.

OOR showed slow activity with all 2-oxoacids tested (Table 2.4). The OOR preparation had no formate dehydrogenase activity, which indicates that the decarboxylase activity of OOR, like other OFORs, is strictly coupled to electron carrier reduction, unlike the decarboxylases where the electron pair is retained in the other product (e.g., pyruvate decarboxylase generates CO_2 and acetaldehyde). These results are consistent with earlier assays of cell lysates (*15*), in which it was shown that the oxalate-catabolizing system in *M. thermoacetica* had different electron acceptor specificity than formate dehydrogenase. OOR was active with a broad range of electron acceptors (Table 2.5). OOR used CODH as an electron acceptor, catalyzing the oxalate-dependent reduction of CO_2 to CO.

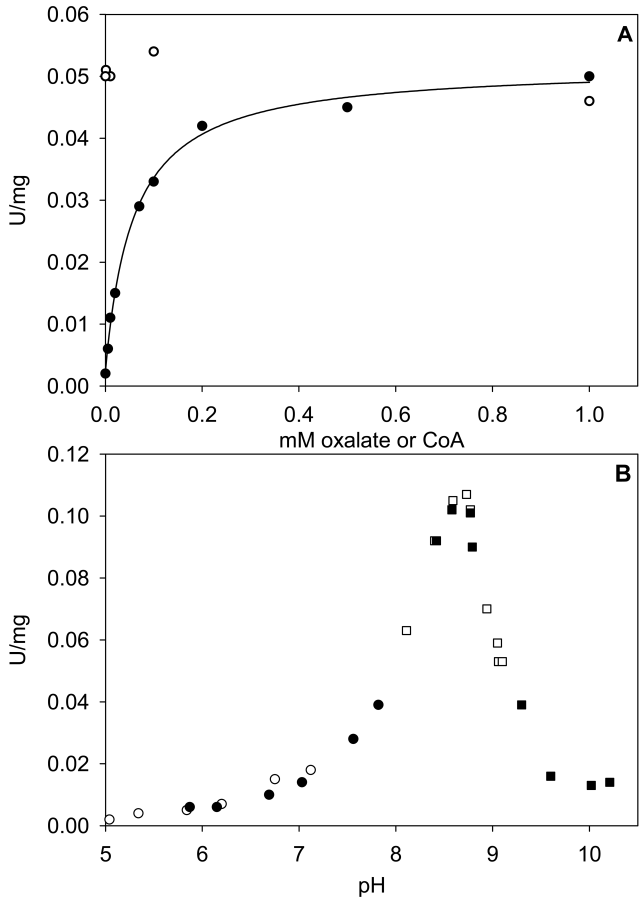

Figure 2.9. Oxalate and pH dependence of OOR activity. A, activity was measured at 25 °C in 50 mM Tris-HCl, pH 7.9, with 10 mM methyl viologen and with varying oxalate concentrations (closed circles) or 1 mM oxalate and varying coenzyme A concentrations (open circles). B, activity was measured at 25 °C in MES (open circles), sodium phosphate (closed circles), borate (open squares), and N-cyclohexyl-3-amino-propanesulfonic acid (closed squares).

2.3.6 *Spectral characterization of OOR*

The UV-visible spectrum of as-isolated OOR had a broad absorbance shoulder between 300 and 500 nm (Figure 2.10). The absorbance in this region increased when the protein was exposed to air or treated with ferricyanide. Treating the protein with sodium dithionite decreased the absorbance of the band between 300 and 500 nm, which is consistent with the bleaching seen upon reduction of $[Fe_4S_4]^{2+/1+}$ clusters in other

Table 2.4. Substrate specificity of OOR

Substrate	μmoles min^{-1} mg^{-1}
Oxalate	0.049 ± 0.004
Glyoxylate	0.024 ± 0.006
Glyoxylate + 100 μM CoA	0.029 ± 0.007
Pyruvate	0.005 ± 0.001
Pyruvate + 100 μM CoA	0.005 ± 0.001
2-oxobutyrate	0.014 ± 0.001
oxaloacetate	0.007 ± 0.003
2-oxovalerate	0.003 ± 0.001
2-oxoglutarate	0.004 ± 0.002
Formate	N.D.[a]

[a]N.D.: not detected. Slow enzyme-dependent methyl viologen reduction of about 0.002 U/mg was seen in assays with no substrate, so we could not measure any slower activity.

Table 2.5. Electron acceptor specificity of OOR

Electron acceptor	μmoles min^{-1} mg^{-1}
Methyl viologen (20 μM)	0.047 ± 0.008
Metronidazole (20 μM)	0.014 ± 0.002
Ferredoxin (20 μM)	0.029 ± 0.001
Cytochrome c (20 μM)	0.182 ± 0.004
NAD^+ (20 μM or 1 mM)	N.D.[a]
$NADP^+$ (20 μM or 1 mM)	N.D.
FAD (20 μM)	0.049 ± 0.008
FMN (20 μM)	0.057 ± 0.004
CODH (20 μM)	0.006 ± 0.001[b]

[a] N.D.: not detected with 230 μg enzyme in 1 mL assay

[b] Measured at pH 7.0, where CO_2 reduction by CODH with dithionite as a reductant was 4.7 μmoles min^{-1} μmole $CODH^{-1}$. OOR activity is approximately three-fold less at pH 7 than at pH 8 with methyl viologen as electron acceptor and OOR is inhibited by CO_2, with approximately half as much activity under 6.8 mM CO_2 as with no CO_2.

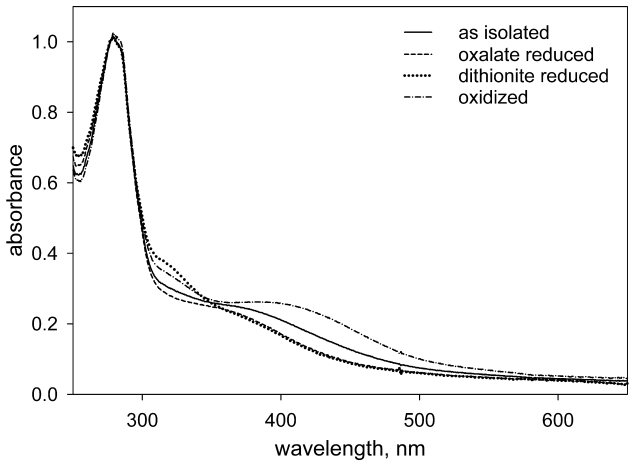

Figure 2.10. UV-visible spectra of OOR. Solid line, as-isolated protein; dashes and dots, oxidized protein; short dashes, oxalate-reduced protein; dots, dithionite-reduced protein. Spectra were measured anaerobically. 4.1 μM protein was prepared in 50 mM sodium phosphate, pH 7.0. Reduced protein was prepared by adding 10 μM sodium oxalate or 15 μM sodium dithionite to the as-isolated protein sample, and the spectra shown were recorded after 20 min. Oxidized protein was prepared by incubation in 6.8 mM CO2 with 80 nM CODH/ACS from *M. thermoacetica*.

proteins, for example, PFOR (*42*). OOR is expected to bind three [Fe_4S_4] clusters, based on the sequence alignments with PFOR and on the metal analyses described above. The maximum difference in absorbance between the oxidized and reduced protein was at 420 nm with a difference extinction coefficient ($\Delta\varepsilon$) of 24.9 mM^{-1} cm^{-1}, or 8.3 per mM [Fe_4S_4], which is similar to the extinction coefficients of 7 - 7.5 per mM cluster that have been reported for PFOR (*42, 43*). When OOR was incubated with oxalate, an identical difference spectrum was observed, and after oxalate reduction, OOR was oxidized by addition of a catalytic amount of CODH/ACS and excess CO_2.

Because [Fe_4S_4] clusters are diamagnetic in the oxidized (2+) state and paramagnetic in the reduced (1+) state, OOR was studied by EPR to follow reduction of the protein by oxalate. The UV-visible spectrum of the protein used in this experiment was used to calculate that the as-isolated protein had 1.7 clusters reduced. As-isolated

OOR exhibited an EPR spectrum (Figure 2.11) with g-values of 2.039, 1.955, 1.927 1.887 and 1.865 (1.2 spins/mol). When a stoichiometric amount of oxalate was added to the protein, the signal intensity increased to 3.4 spins/mol. The 1.955 and 1.865 features became broader and an additional feature at g = 2.007 was seen in samples of fully reduced OOR prepared with oxalate or dithionite (3.2 spins/mol). This EPR spectrum was saturated above 0.129 mW at 9K. The relative intensities of the 2.039 and 1.927 features decreased as the power was increased, although they were still present at 129 mW. When oxalate-reduced OOR was oxidized by additions of oxidized cytochrome c, there was no change in the overall shape of the EPR spectrum, even in the almost completely oxidized protein (0.07 spins/mol, (Figure 2.11)), indicating that the potentials of the iron-sulfur clusters are similar. The *g*-values of the OOR spectra are typical of $[Fe_4S_4]^{2+/1+}$ clusters such as those in eight iron (2-$[Fe_4S_4]$) ferredoxins (*44, 45*) and other OFOR enzymes (*31, 43*). As eight iron ferredoxins go from partially to fully reduced, an increase in complexity of the EPR spectrum is seen, which results from spin-spin interactions between two reduced $[Fe_4S_4]$ clusters. Similar coupling of clusters has been seen in PFOR (*43*), as well as spin-spin interaction between an $[Fe_4S_4]$ cluster and a substrate-derived radical in the active site (*31*). We did not see an increase in complexity with increasing reduction of OOR, nor did we see a substrate-derived radical when OOR was frozen ~30s after mixing with oxalate.

2.4 Discussion

Oxalate is an important metabolite that is produced in the soil and in the animal GI tract, with elevated levels causing kidney stones. Many bacteria that use oxalate as an

energy source also use oxalate as a carbon source by reduction to glyoxylate, which is incorporated into the central metabolite 3-phosphoglycerate (*46, 47*), but enzymes involved in glyoxylate incorporation have not been detected in oxalate-grown cultures of *M. thermoacetica* (*3, 48*). We have shown that *M. thermoacetica* metabolizes oxalate

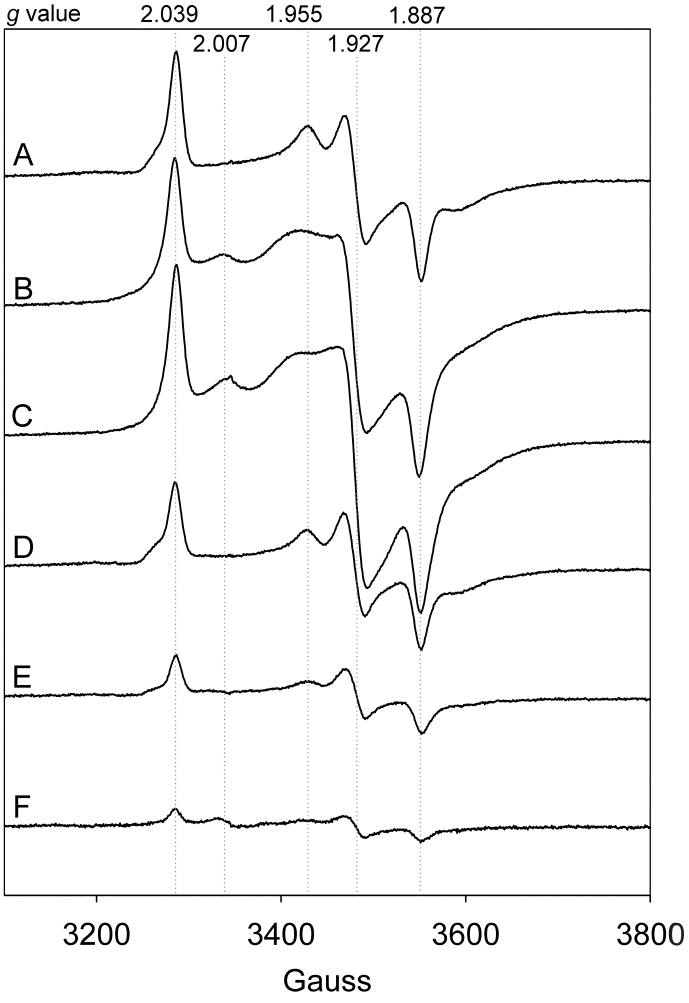

Figure 2.11. EPR spectra of OOR. 39 μM OOR was reduced with oxalate and then titrated with oxidized cytochrome c. A, as-isolated OOR (1.2 spins/monomer); B, oxalate-reduced OOR (3.4 spins/monomer); C, dithionite-reduced OOR (3.2 spins/monomer); D–F, oxalate reduced OOR, reoxidized by the addition of oxidized cytochrome c (D, 1.3 spins/monomer, E, 0.7 spins/monomer, F, 0.07 spins/monomer). The parameters were as follows: receiver gain, 2 x 10^2; modulation frequency, 100 kHz; modulation amplitude, 10 G; center field, 3450 G; sweep width, 700 G; microwave power, 0.129 milliwatt at 9 K.

very simply by a novel CoA-independent OFOR that catalyzes the oxidative decarboxylation of oxalate to two mol of CO_2, coupled to the reduction of ferredoxin (or other electron acceptors). The apparent reaction is $C_2O_4^{2-} + Fd_{ox} \leftrightarrow 2\ CO_2 + Fd_{red}$,[4] although we have not yet shown whether CO_2 or bicarbonate is the product that is released from OOR. Our results are consistent with previous studies, which indicate that incorporation of oxalate into cell material requires conversion to CO_2 (*3, 14*). For example, *M. thermoacetica* can grow on oxalate even in CO_2-free medium; however, when cells are grown on oxalate and CO_2, very little radioactivity from ^{14}C-oxalate is incorporated into biomass (*14*). Thus, OOR enables growth on oxalate by linking the production of CO_2 and reducing equivalents to the Wood-Ljungdahl pathway of autotrophic anaerobic acetyl-CoA formation (*3, 14*).

Oxalate induces the expression of three proteins (36, 43 and 32 kDa) in *M. thermoacetica* that can be resolved by two-dimensional PAGE electrophoresis. Earlier studies described the induction of two protein bands (one of the bands apparently was not resolved by one-dimensional SDS-PAGE) when *M. thermoacetica* was grown on oxalate, relative to growth on CO, formate or glyoxylate (*14*). Mass spectrometric results reveal that the oxalate-induced proteins belong to the OFOR family and are encoded within an operon that includes a homolog of *O. formigenes* oxalate:formate antiporter, a permease and a gene encoding a transcriptional regulatory protein, for which we propose the name OorR. OorR contains an N-terminal helix-turn-helix DNA binding domain and a C-terminal ligand-binding domain and is likely to coordinately regulate expression of OOR with expression of the enzymes of the Wood-Ljungdahl pathway. Oxalate is a unique

[4] The ferredoxin that we have used with OOR is an 8-Fe ferredoxin that contains two $[Fe_4S_4]$ clusters and accepts two electrons.

substrate for *M. thermoacetica*, which uses nitrate instead of CO_2 as electron acceptor when grown on other multiple-carbon growth substrates in the presence of nitrate and CO_2. However, CO_2 is used preferentially over nitrate when it is growing on oxalate (*3*). Nitrate appears to inhibit autotrophic growth by repressing the Wood-Ljungdahl pathway at the transcriptional level (*1, 2*). We suggest that interactions between oxalate, OorR and the promoters of the *oor* and *acs* operons are able to induce the *oor* operon and prevent the nitrate-dependent repression of the Wood-Ljungdahl pathway. *M. thermoacetica* does not produce formate from oxalate, but acetate, the end-product of the Wood-Ljungdahl pathway, could be exchanged with oxalate by the antiporter.

OOR is the first protein shown to catalyze anaerobic oxalate oxidation, unlike previously described anaerobic enzymes that produce CO_2 and formyl-CoA (*6, 9*). Although several features (e.g., Fe_4S_4 clusters and TPP content) of OOR are similar to other members of the OFOR family, OOR is unique among family members in its lack of requirement for CoA. Figure 2.12 describes a proposed mechanism of OOR, based on the results described here and on analogy with conserved features of other OFORs, such as PFOR whose mechanism has been extensively studied (*42, 43, 49*) and whose crystal structure is known (*29*).

2.4.1 *Steps 1 &2: Binding of TPP, Mg^{2+} and oxalate*

The early steps of the reaction would resemble those of all TPP-dependent enzymes, reviewed recently (*50*). After binding oxalate (Step 1), Step 2 of the proposed OOR mechanism involves nucleophilic attack of the anionic ylide of OOR-bound TPP on oxalate to generate an oxalyl-TPP adduct. The purified OOR contains Mg^{2+} and TPP, which were added during purification because in some OFORs, like PFOR from *M.*

thermoacetica, TPP dissociates rather easily resulting in loss of activity in buffer lacking TPP. However, TPP remains tightly bound to OOR even after extensive buffer exchange and over several months' storage. Based on sequence homology between OOR and the *Desulfovibrio africanus* PFOR, whose structure is known (*29*), we find that most of the key residues in PFOR that are involved in binding and activating TPP to generate the deprotonated ylide are conserved in OOR. These include beta subunit residues Cys130, and Asn143 (Cys840 and Asn996 in *D. africanus* PFOR), which interact with the pyrophosphate moiety of TPP. Conserved residues that interact with the Mg^{2+} ion include

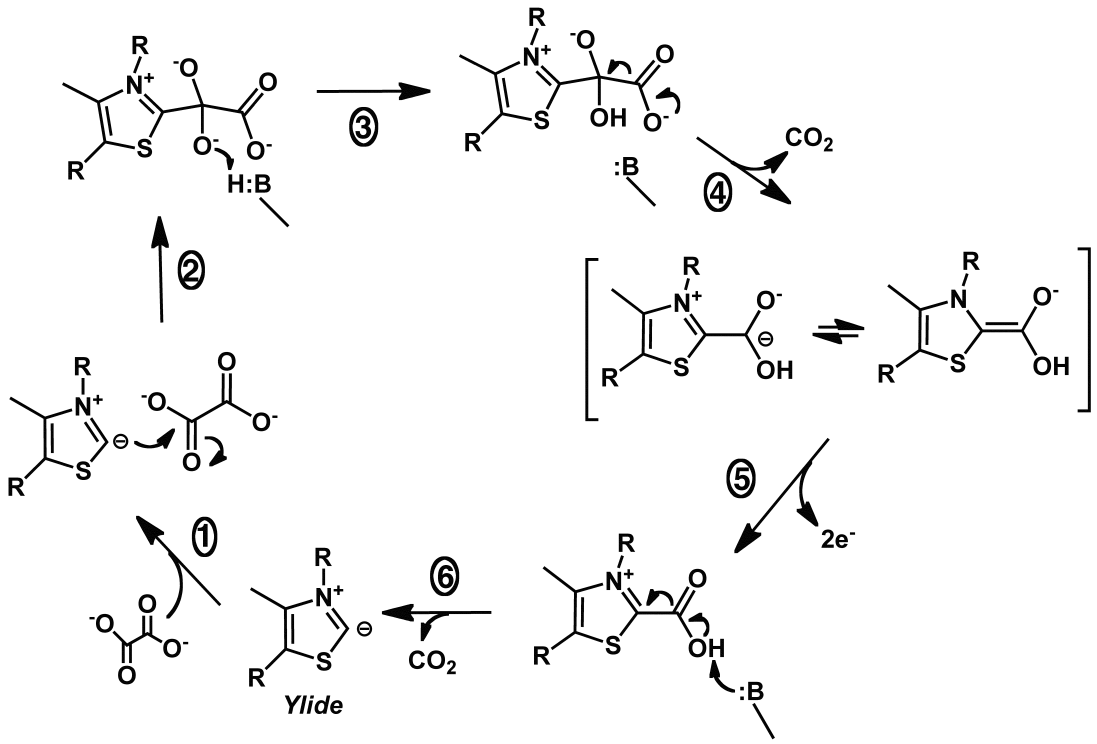

Figure 2.12. Proposed OOR mechanism. Oxalate binds to OOR (step 1) and undergoes nucleophilic attack by the TPP ylide (step 2), generating oxalyl-TPP, which could be stabilized by protonation from a general base (step 3). Decarboxylation (step 4) leaves an anionic intermediate that would release two electrons to the Fe_4S_4 clusters (step 5). The carboxyl-TPP that remains could be decarboxylated to release a second CO_2 molecule (step 6) or hydrolyzed to release bicarbonate (not shown), regenerating the starting form of the enzyme.

a $G^{109}DGX_{32}N$ motif ($G^{962}DGX_{32}N$ in PFOR). Another key conserved residue is Asp59 (Asp64 in PFOR), which interacts with the N1′ pyrimidine group of TPP and plays a key role in deprotonation of the C-2 of the thiazole ring to generate the active ylide. The conserved residue Asn996 in PFOR (Asn143) forms a hydrogen bonding interaction with the thiazolium sulfur of TPP and a large hydrophobic residue, Phe869 of PFOR (Ile159 in the beta subunit of OOR), interacts with TPP to promote formation of a V-conformation between the pyrimidine and thiazolium ring, which is conserved in all TPP-dependent enzymes so far studied. Different residues can stabilize the V-conformation in TPP-dependent enzymes: Ile is also found in this position in pyruvate decarboxylase (*51*), Met and Leu are found in pyruvate oxidase and transketolase, and other OFOR enzymes have His and Tyr.

Of the 2-oxoacid substrates we tested, oxalate was oxidized most quickly. Furthermore, the low K_m for oxalate (~60 μM) and the fact that the enzyme is induced in the presence of oxalate are consistent with oxalate being the physiological substrate for the enzyme. Although OOR can oxidize glyoxylate, the enzyme is not induced in cells grown on glyoxylate (*14*). Thus, we think it unlikely that OOR would be involved in glyoxylate metabolism in *M. thermoacetica*. OOR contains conserved residues that interact with the carboxyl and carbonyl groups of pyruvate in PFOR, but contains substitutions that we propose are important for binding the carboxyl group of oxalate that replaces the acetyl group of pyruvate.

Several residues involved in pyruvate binding in PFOR are conserved in OOR, including Arg109 (Arg114 in PFOR, which binds the carboxyl group of pyruvate) and Asn143 (Asn996 in PFOR forms hydrogen bonds to the carbonyl group of pyruvate).

Substitution of the Arg in *Sulfolobus tokodaii* that corresponds to Arg114 abolished activity (*34*). As expected, Ile123 and Ile843, which interact with the methyl group of PFOR are not conserved in OOR. Thr31 in PFOR is a highly conserved residue among the OFORs and is part of a YPITP motif that is important for catalysis. Substitutions of the end residues of this motif in an *Aeropyrum pernix* OFOR destroy activity and separate mutations of the three middle residues have varying effects that are in general larger for k_{cat} than for K_m, which suggests that the motif is important during reaction turnover (*35*). However, Thr31 is replaced with Arg31 in the OOR. Inclusion of a second Arg in the active site may help to stabilize the additional negative charge on oxalate. Since Arg in this position is found in only those few sequences in the NCBI protein database that have high identity to that of OOR, we propose that a YPIRP motif replaces the usual conserved YPITP motif, to promote interactions with may be characteristic of OORs.

2.4.2 *Decarboxylation and electron transfer*

In analogy to the mechanism of PFOR (*42*), a general base would be expected to stabilize the negative charge on the oxalyl-TPP intermediate in Step 3, followed by decarboxylation of the oxalyl-TPP adduct in step 4 to yield a reactive anionic carboxyl-TPP intermediate that, in Step 5, would release two electrons into the internal electron transfer pathway consisting of three $[Fe_4S_4]^{2+/1+}$ clusters. OOR contains sufficient iron to accommodate these three clusters. In addition, all 12 Cys residues that bind the three clusters of PFOR are conserved in the sequence of OOR. Furthermore, EPR and UV-visible experiments clearly showed that OOR contains three $[Fe_4S_4]^{2+/1+}$ and that oxalate

can reduce all of these clusters. Because oxalate is a two-electron donor, full reduction of all of the clusters would require two mol of oxalate.

Because [Fe_4S_4] clusters accept one-electron at a time, there is likely to be a transient intermediate in which one of the clusters is reduced by the anionic carboxy-TPP anion to generate a carboxy-TPP radical (not shown); transient kinetic experiments are underway to test this hypothesis.

In the PFOR reaction, binding of CoA accelerates the electron transfer reaction from the HE-TPP radical to the iron-sulfur clusters by 10^5-fold. However, OOR is a unique member of this family in having no requirement for CoA; therefore, Step 6 would involve a second decarboxylation to regenerate the active ylide for the next round of catalysis. Though it seems less likely, it is possible that this carboxy-TPP adduct undergoes hydrolysis to release bicarbonate instead of CO_2. One of the proposed roles of CoA in PFOR and other OFORs is to generate a highly reducing anionic intermediate that could transfer electrons to the clusters (*42, 52*), and the same role has been proposed for phosphate in *Lactobacillus plantarum* pyruvate oxidase (POX), which forms acetyl-phosphate and CO_2 from pyruvate (*53*). Perhaps the negative charge on the OOR carboxy-TPP adduct is sufficiently reducing to make CoA unnecessary.

In the final steps of the reaction, the two-electron-reduced state of OOR transfers its reducing equivalents from the internal electron transfer wire of [Fe_4S_4] clusters to an external electron acceptor. Like PFOR, OOR can use a wide range of acceptors and is unable to transfer electrons to pyridine nucleotides. Ferredoxin is one of these and is a likely physiological electron acceptor that could carry electrons to enzymes of the Wood-Ljungdahl pathway. The rates were similar among all electron acceptors that were found

to work. This suggests that the rate of catalysis is limited by some step other than electron transfer from the enzyme to the acceptor. Interestingly, like PFOR, OOR can transfer electrons directly to CODH to generate CO. This could be a physiologically relevant reaction *in vivo*, since electrons from oxalate are used in the synthesis of acetyl-CoA (*3*) and since *M. thermoacetica* can be cultured on oxalate even in CO_2-free medium (*14*). We propose that under CO_2-limiting conditions, CO_2 as well as electrons could be channeled directly from OOR to CODH. This would be an extremely interesting three-component channeling machine, because it is clear that CO is channeled from CODH to ACS (*54, 55*).

2.5 References

(1) Frostl, J. M., Seifritz, C., and Drake, H. L. (1996) Effect of nitrate on the autotrophic metabolism of the acetogens *Clostridium thermoautotrophicum* and *Clostridium thermoaceticum*. *J. Bacteriol. 178*, 4597-603.

(2) Arendsen, A. F., Soliman, M. Q., and Ragsdale, S. W. (1999) Nitrate-dependent regulation of acetate biosynthesis and nitrate respiration by *Clostridium thermoaceticum*. *J. Bacteriol. 181*, 1489-95.

(3) Seifritz, C., Frostl, J. M., Drake, H. L., and Daniel, S. L. (2002) Influence of nitrate on oxalate- and glyoxylate-dependent growth and acetogenesis by *Moorella thermoacetica*. *Arch. Microbiol. 178*, 457-64.

(4) Strobel, B. W. (2001) Influence of vegetation on low-molecular-weight carboxylic acids in soli solution - a review. *Geoderma 99*, 169-198.

(5) Anantharam, V., Allison, M. J., and Maloney, P. C. (1989) Oxalate:formate exchange: the basis for energy coupling in *Oxalobacter*. *J. Biol. Chem. 264*, 7244-7250.

(6) Baetz, A. L., and Allison, M. J. (1989) Purification and characterization of oxalyl-coenzyme A decarboxylase from *Oxalobacter formigenes*. *J. Bacteriol. 171*, 2605-2608.

(7) Allison, M. J., Dawson, K. A., Mayberry, W. R., and Foss, J. G. (1985) *Oxalobacter formigenes* gen. nov., sp. nov.: oxalate-degrading anaerobes that inhabit the gastrointestinal tract. *Arch. Microbiol. 141*, 1-7.

(8) Quayle, J. R., and Keech, D. B. (1959) Carbon assimilation by *Pseudomonas oxalaticus* (OX 1). 1. Formate and carbon dioxide utilization during growth on formate. *Biochem. J 72*, 623-630.

(9) Quayle, J. R. (1963) Carbon assimilation by *Pseudomonas oxalaticus* (OX1). 7. Decarboxylation of oxalyl-Coenzyme A to formyl-Coenzyme A. *Biochem. J 89*, 492-503.

(10) Costelloe, S. J., Ward, J. M., and Dalby, P. A. (2008) Evolutionary analysis of the TPP-dependent enzyme family. *J. Mol. Evol. 66*, 36-49.

(11) Tanner, A., and Bornemann, S. (2000) *Bacillus subtilis* YvrK Is an Acid-Induced Oxalate Decarboxylase. *J. Bacteriol. 182*, 5271-5273.

(12) Woo, E.-J., Dunwell, J. M., Goodenough, P. W., Marvier, A. C., and Pickersgill, R. W. (2000) Germin is a manganese containing homohexamer with oxalate oxidase and superoxide dismutase activities. *Nat. Struct. Biol. 7*, 1036-1040.

(13) Seifritz, C., Fröstl, J. M., Drake, H. L., and Daniel, S. L. (2006) Glycolate as a metabolic substrate for the acetogen *Moorella thermoacetica*. *FEMS Microbiol. Lett. 170*, 399-405.

(14) Daniel, S. L., and Drake, H. L. (1993) Oxalate- and Glyoxylate-Dependent Growth and Acetogenesis by Clostridium thermoaceticum. *Appl. Environ. Microbiol. 59*, 3062-3069.

(15) Daniel, S. L., Pilsl, C., and Drake, H. L. (2004) Oxalate metabolism by the acetogenic bacterium *Moorella thermoacetica*. *FEMS Microbiol. Lett. 231*, 39-43.

(16) Ragsdale, S. W., Clark, J. E., Ljungdahl, L. G., Lundie, L. L., and Drake, H. L. (1983) Properties of purified carbon monoxide dehydrogenase from *Clostridium thermoaceticum*, a nickel, iron-sulfur protein. *J. Biol. Chem. 258*, 2364-2369.

(17) Barent, R. L., and Elthon, T. E. (1992) Two-dimensional gels: an easy method for large quantities of proteins. *Plant Mol. Biol. Rep. 10*, 338-344.

(18) Antonini, E., and Brunori, M. (1971) *Hemoglobin and myoglobin in their reactions with ligands*, Vol. 21, North-Holland Publishing Company, Amsterdam.

(19) Elliott, J. I., and Brewer, J. M. (1978) The inactivation of yeast enolase by 2,3-butanedione. *Arch. Biochem. Biophys. 190*, 351-357.

(20) Penttinen, H. K. (1979) Fluorometric determination of thiamine and its mono-, di-, and triphosphate esters. *Methods Enzymol. 62*, 58-59.

(21) Pierce, E., Xie, G., Barabote, R. D., Saunders, E., Han, C. S., Detter, J. C., Richardson, P., Brettin, T. S., Das, A., Ljungdahl, L. G., and Ragsdale, S. W. (2008) The complete genome sequence of *Moorella thermoacetica* (f. *Clostridium thermoaceticum*). *Environ. Microbiol. 10*, 2550-2573.

(22) Abe, K., Ruan, Z.-S., and Maloney, P. C. (1996) Cloning, Sequencing, and Expression in *Escherichia coli* of OxlT, the Oxalate:Formate Exchange Protein of Oxalobacter formigenes. *J. Biol. Chem. 271*, 6789-6793.

(23) Zhang, Q., Iwasaki, T., Wakagi, T., and Oshima, T. (1996) 2-oxoacid:ferredoxin oxidoreductase from the thermoacidophilic archaeon, *Sulfolobus* sp. Strain 7. *J. Biochem. 120*, 587-599.

(24) Tersteegen, A., Linder, D., Thauer, R. K., and Hedderich, R. (1997) Structures and Functions of Four Anabolic 2-Oxoacid Oxidoreductases in *Methanobacterium thermoautotrophicum*. *Eur. J. Biochem. 244*, 862-868.

(25) Mai, X., and Adams, M. W. (1994) Indolepyruvate ferredoxin oxidoreductase from the hyperthermophilic archaeon *Pyrococcus furiosus*. A new enzyme involved in peptide fermentation. *J. Biol. Chem. 269*, 16726-16732.

(26) Heider, J., Mai, X., and Adams, M. (1996) Characterization of 2-ketoisovalerate ferredoxin oxidoreductase, a new and reversible coenzyme A-dependent enzyme involved in peptide fermentation by hyperthermophilic archaea. *J. Bacteriol. 178*, 780-787.

(27) Hughes, N. J., Clayton, C. L., Chalk, P. A., and Kelly, D. J. (1998) Helicobacter pylori *porCDAB* and *oorDABC* Genes Encode Distinct Pyruvate:Flavodoxin and 2-Oxoglutarate:Acceptor Oxidoreductases Which Mediate Electron Transport to NADP. *J. Bacteriol. 180*, 1119-1128.

(28) Rosenthal, B., Mai, Z., Caplivski, D., Ghosh, S., de la Vega, H., Graf, T., and Samuelson, J. (1997) Evidence for the bacterial origin of genes encoding fermentation enzymes of the amitochondriate protozoan parasite *Entamoeba histolytica*. *J. Bacteriol. 179*, 3736-3745.

(29) Chabriere, E., Charon, M.-H., Volbeda, A., Pieulle, L., Hatchikian, E. C., and Fontecilla-Camps, J.-C. (1999) Crystal structures of the key anaerobic enzyme pyruvate:ferredoxin oxidoreductase, free and in complex with pyruvate. *Nat. Struct. Mol. Biol. 6*, 182-190.

(30) Drennan, C. L., Heo, J., Sintchak, M. D., Schreiter, E., and Ludden, P. W. (2001) Life on carbon monoxide: X-ray structure of *Rhodospirillum rubrum* Ni-Fe-S carbon monoxide dehydrogenase. *Proc. Natl. Acad. Sci. U.S.A. 98*, 11973-11978.

(31) Cammack, R., Kerscher, L., and Oesterhelt, D. (1980) A stable free radical intermediate in the reaction of 2-oxoacid:ferredoxin oxidoreductases of *Halobacterium halobium*. *FEBS Lett. 118*, 271-273.

(32) Breese, K., Boll, M., Alt-Mörbe, J., Schägger, H., and Fuchs, G. (1998) Genes coding for the benzoyl-CoA pathway of anaerobic aromatic metabolism in the bacterium *Thauera aromatica*. *Eur. J. Biochem. 256*, 148-154.

(33) Nishizawa, Y., Yabuki, T., Fukuda, E., and Wakagi, T. (2005) Gene expression and characterization of two 2-oxoacid:ferredoxin oxidoreductases from *Aeropyrum pernix* K1. *FEBS Lett. 579*, 2319-2322.

(34) Fukuda, E., and Wakagi, T. (2002) Substrate recognition by 2-oxoacid:ferredoxin oxidoreductase from *Sulfolobus* sp. strain 7. *Biochim. Biophys. Acta, Protein Struct. Mol. Enzymol. 1597*, 74-80.

(35) Fukuda, E., Kino, H., Matsuzawa, H., and Wakagi, T. (2001) Role of a highly conserved YPITP motif in 2-oxoacid:ferredoxin oxidoreductase: Heterologous expression of the gene from *Sulfolobus* sp. strain 7, and characterization of the recombinant and variant enzymes *Eur. J. Biochem. 268*, 5639-5646.

(36) Ma, K., Hutchins, A., Sung, S.-J. S., and Adams, M. W. W. (1997) Pyruvate ferredoxin oxidoreductase from the hyperthermophilic archaeon, *Pyrococcus furiosus*, functions as a CoA-dependent pyruvate decarboxylase. *Proc. Natl. Acad. Sci. U.S.A. 94*, 9608-9613.

(37) Meinecke, B., Bertram, J., and Gottschalk, G. (1989) Purification and characterization of the pyruvate-ferredoxin oxidoreductase from *Clostridium acetobutylicum*. *Arch. Microbiol. 152*, 244-250.

(38) Park, E. Y., Clark, J. E., DerVartanian, D. V., and Ljungdahl, L. G. (1991) 5,10-Methylenetetrahydrofolate Reductases: Iron-Sulfur-Zinc Flavoproteins of Two Acetogenic Clostridia, in *Chemistry and Biochemistry of Flavoenzymes* (Müller, F., Ed.) pp 389-400, CRC Press, Boca Raton.

(39) Yamamoto, I., Saiki, T., Liu, S. M., and Ljungdahl, L. G. (1983) Purification and properties of NADP-dependent formate dehydrogenase from *Clostridium thermoaceticum*, a tungsten-selenium-iron protein. *J. Biol. Chem. 258*, 1826-1832.

(40) Dörner, E., and Boll, M. (2002) Properties of 2-oxoglutarate:ferredoxin oxidoreductase from *Thauera aromatica* and its role in enzymatic reduction of the aromatic ring. *J. Bacteriol. 184*, 3979-3983.

(41) Weast, R. C., and Astle, M. J. (1981), CRC Press, Inc., Boca Raton, Florida.

(42) Furdui, C., and Ragsdale, S. W. (2002) The Roles of Coenzyme A in the Pyruvate:Ferredoxin Oxidoreductase Reaction Mechanism: Rate Enhancement of Electron Transfer from a Radical Intermediate to an Iron-Sulfur Cluster. *Biochemistry 41*, 9921-9937.

(43) Pieulle, L., Guigliarelli, B., Asso, M., Dole, F., Bernadac, A., and Hatchikian, E. C. (1995) Isolation and characterization of the pyruvate-ferredoxin oxidoreductase from the sulfate-reducing bacterium *Desulfovibrio africanus*. *Biochim. Biophys. Acta, Protein Struct. Mol. Enzymol. 1250*, 49-59.

(44) Orme-Johnson, W. H., and Beinert, H. (1969) Heterogeneity of paramagnetic species in two iron-sulfur proteins: *Clostridium pasteurianum* ferredoxin and milk xanthine oxidase. *Biochem. Biophys. Res. Commun. 36*, 337-344.

(45) Mathews, R., Charlton, S., Sands, R. H., and Palmer, G. (1974) On the nature of the spin coupling between the iron-sulfur clusters in the eight-iron ferredoxins. *J. Biol. Chem. 249*, 4326-4328.

(46) Cornick, N. A., and Allison, M. J. (1996) Anabolic incorporation of oxalate by *Oxalobacter formigenes*. *Appl. Environ. Microbiol. 62*, 3011-3013.

(47) Cornick, N. A., Yan, B., Bank, S., and Allison, M. J. (1996) Biosynthesis of amino acids by *Oxalobacter formigenes*: analysis using ^{13}C-NMR. *Can. J. Microbiol. 42*, 1219-1224.

(48) Seifritz, C., Fröstl, J. M., Drake, H. L., and Daniel, S. L. (1999) Glycolate as a metabolic substrate for the acetogen Moorella thermoacetica. *FEMS Microbiol. Lett. 170*, 399-405.

(49) Menon, S., and Ragsdale, S. W. (1997) Mechanism of the Clostridium thermoaceticum Pyruvate:Ferredoxin Oxidoreductase: Evidence for the Common Catalytic Intermediacy of the Hydroxyethylthiamine Pyropyrosphate Radical. *Biochemistry 36*, 8484-8494.

(50) Ragsdale, S. W. (2003) Pyruvate ferredoxin oxidoreductase and its radical intermediate. *Chem. Rev. 103*, 2333-2346.

(51) Xia, J., Hu, Z., Popescu, C. V., Lindahl, P. A., and Münck, E. (1997) Mössbauer and EPR Study of the Ni-Activated α-Subunit of Carbon Monoxide Dehydrogenase from *Clostridium thermoaceticum*. *J. Am. Chem. Soc. 119*, 8301-8312.

(52) Astashkin, A. V., Seravalli, J., Mansoorabadi, S. O., Reed, G. H., and Ragsdale, S. W. (2006) Pulsed Electron Paramagnetic Resonance Experiments Identify the Paramagnetic Intermediates in the Pyruvate Ferredoxin Oxidoreductase Catalytic Cycle. *J. Am. Chem. Soc. 128*, 3888-3889.

(53) Tittmann, K., Wille, G., Golbik, R., Weidner, A., Ghisla, S., and Hübner, G. (2005) Radical Phosphate Transfer Mechanism for the Thiamin Diphosphate- and FAD-Dependent Pyruvate Oxidase from *Lactobacillus plantarum*: Kinetic Coupling of Intercofactor Electron Transfer with Phosphate Transfer to Acetyl-thiamin Diphosphate via a Transient FAD Semiquinone/Hydroxyethyl-ThDP Radical Pair. *Biochemistry 44*, 13291-13303.

(54) Seravalli, J., and Ragsdale, S. W. (2000) Channeling of Carbon Monoxide during Anaerobic Carbon Dioxide Fixation. *Biochemistry 39*, 1274-1277.

(55) Doukov, T. I., Blasiak, L. C., Seravalli, J., Ragsdale, S. W., and Drennan, C. L. (2008) Xenon in and at the end of the tunnel of bifunctional carbon monoxide dehydrogenase/acetyl-CoA synthase. *Biochemistry 47*, 3474-3483.

Appendix to Chapter II, Additional Sequence Analysis

2-Oxoacid:ferredoxin oxidoreductases are made up of a minimum of three conserved domains, alpha, beta and gamma, with an additional delta domain in most OFORs. The genomic arrangement and fusion of these domains varies, with some proteins consisting of two subunits (αγ-fusion and β, called αβ type), some having separate α, β, γ and δ subunits and some (like many bacterial PFORs, including the *M. thermoacetica* PFOR) containing all four domains fused. The residues involved in binding TPP and one $[Fe_4S_4]^{2+/1+}$ cluster are in the beta subunit (*23*). Enzymes that include the delta subunit have two additional $[Fe_4S_4]^{2+/1+}$ clusters that are involved in electron transfer from the TPP active site to ferredoxin (*42*). αβ type OFORs that lack delta subunits have only one $[Fe_4S_4]^{2+/1+}$ cluster per αβ. The OOR protein is made up of separate α and β subunits and a third subunit that is a fusion of γ and δ domains (Figure 2.3).

We performed separate clustalW alignments of the sequences of the three OOR subunits with those of corresponding subunits of biochemically characterized pyruvate, 2-oxoisovalerate, 2-oxoglutarate, indolepyruvate and broad specificity oxidoreductases (see caption to Figure 2.8). The chosen sequences included the *D. africanus* PFOR, which has been crystallized in complex with pyruvate (*29*), allowing us to determine whether or not oxoacid binding residues are conserved in OOR. In the beta subunit, residues Gly109, Asp110, Gly111 and Cys130 (Gly962, Asp963, Gly964 and Cys840 are

the corresponding residues in the *D. africanus* PFOR), which coordinate TPP and the adjacent Mg^{2+} ion, are present in OOR, along with the four cysteines (Cys residues 24, 27, 52 and 225 in the beta subunit) that ligate the $[Fe_4S_4]$ cluster that is nearest TPP. The eight cysteine residues that bind the other two $[Fe_4S_4]$ clusters are conserved in the OOR delta subunit (Cys residues 261, 264, 267 and 300 ligate one cluster and 271, 290, 293 and 296 coordinate the other cluster).

CHAPTER III

Involvement of a TPP-based Radical in the Mechanism of Oxalate Oxidoreductase

3.1 Introduction

Moorella thermoacetica is a strictly anaerobic bacterium that grows on many different electron donors and acceptors. Among its electron accepting pathways is reduction of CO_2 to acetate by the Wood-Ljungdahl pathway. *M. thermoacetica* metabolically couples oxidation of sugars, acids like pyruvate and lactate, and two-carbon acids such as oxalate, glyoxylate and glycolate to the Wood-Ljungdahl pathway (*1*). During growth using this pathway, acetate and cell mass are the only growth products and electron-rich growth substrates like glucose are converted almost stoichiometrically to acetate; therefore *M. thermoacetica* is called a homoacetogen. The Wood-Ljungdahl pathway can also be used for autotrophic growth, enabling *M. thermoacetica* to grow on CO, H_2/CO_2, formate, and methyl-group donors such as methanol and methoxylated aromatic compounds (*2, 3*). *M. thermoacetica* metabolizes oxalate by a very simple pathway: one mole of oxalate is oxidized to produce two moles of CO_2 and two moles of a reduced electron acceptor (or one mole of a reduced $2e^-$ acceptor). Eight electrons are used by the Wood-Ljungdahl pathway to reduce two CO_2 to acetate, and the

stoichiometry of growth on oxalate is, as expected, four moles oxidized to produce six moles of CO_2 and one mole of acetate (*4*).

In the work described in Chapter II, we showed that *M. thermoacetica* growing on oxalate makes a single enzyme that catalyzes the oxidation of oxalate and reduction of several different electron acceptors (*5*). This oxalate oxidoreductase (OOR) is a member of the family of 2-oxoacid:ferredoxin oxidoreductases (OFORs) that catalyze Eq. 1[5]. Unlike all other known members of this family, OOR does not use CoA. It oxidizes oxalate directly to $2CO_2$ or to CO_2 and bicarbonate.

$$RCOCOO^- + Fd_{ox} + CoAS^- \leftrightarrows RCOSCoA + Fd_{red} + CO_2 \qquad \text{(Eq. 3.1)}$$

The overall sequence similarity between OOR and other well-characterized members of the OFOR family is between 35 and 60%, and in general, OOR is most closely related to archaeal and bacterial PFORs, among known OFORs. The crystal structure of pyruvate:Fd oxidoreductase (PFOR) from *Desulfovibrio africanus* has been solved (*6*). OOR shares sequence similarity of around 40% with *D. africanus* PFOR, so we have used this PFOR as a model for thinking about the structure of OOR. This PFOR is a dimer of two large (135 kDa) subunits. Each subunit contains a TPP active site, with three Fe_4S_4 clusters arranged in a line from the active site to the surface of the protein. The quaternary structure and stoichiometry of TPP and Fe_4S_4 cluster binding in the *D. africanus* PFOR are representative of the OFOR family. In *D. africanus* PFOR, the entire sequence is contained in one large peptide, which dimerizes. OOR (along with many other enzymes in this family) has the same overall sequence composition, but is made up

[5] The reaction shown in Eq. 1 produces two electrons per mole of substrate. Both OOR and pyruvate:ferredoxin oxidoreductase from *M. thermoacetica* use a ferredoxin with two $[Fe_4S_4]^{2+/1+}$ clusters as an electron acceptor in *in vitro* assays.

of three separate peptides. The native size of OOR is consistent with an $\alpha_2\beta_2\gamma_2$ arrangement of subunits.

The catalytic mechanism of OFOR enzymes, particularly of PFOR from *M. thermoacetica*, has been studied in detail. In common with pyruvate dehydrogenase and pyruvate decarboxylase, C2 of the thiazole ring of TPP is deprotonated to form a carbanion that performs a nucleophilic attack on the alpha carbon of pyruvate. CO_2 is released, leaving an anionic hydroxyethyl-TPP (HE-TPP) intermediate which is converted to a HE-TPP radical by transfer of one electron to a $[Fe_4S_4]^{2+}$ cluster. This radical decays slowly (with a half-life of ~4 minutes) in the absence of CoA. This state of the enzyme might be stabilized by transfer of the electron from the cluster proximal to the active site (the A cluster) to the middle cluster (the B cluster), which has a higher redox potential than the A cluster. In the presence of CoA, the radical decays 10^5-fold more quickly (*7*), and acetyl-CoA is formed and dissociates from the enzyme. Internal electron transfers between the three Fe_4S_4 clusters pass electrons to the surface of the enzyme, where they are transferred to ferredoxin or to an artificial electron acceptor, such as methyl viologen. Both PFOR and OOR are able to bind and oxidize a substrate molecule in the absence of an external electron acceptor when the iron-sulfur clusters are already partly reduced.

The substrate-derived radical was first seen in PFOR and 2-oxoglutarate:Fd oxidoreductases from *Halobacterium halobium* (*8*), and has been found in other OFORs (*9-12*). It has been proposed to be a catalytic intermediate in all OFOR reactions (*13*). A substrate-derived HE-TPP radical is also an intermediate in the catalytic cycle of *Lactobacillus plantarum* pyruvate oxidase (*Lp*POX), which catalyzes the oxidation of

pyruvate, producing CO_2 and acetyl-phosphate. In *Lp*POX, the electrons released are transferred from the TPP active site to a flavin adenine dinucleotide cofactor, which is oxidized by molecular oxygen to form H_2O_2 (*14*). The structure of the HE-TPP radical has been studied in detail by EPR spectroscopy of PFOR from *M. thermoacetica* and by X-ray crystallography of pyruvate-soaked crystals of PFOR from *D. africanus*. Based on the bent conformation of the thiazole ring of TPP and the unusually long bond (1.70 - 1.95 Å) between the substrate alpha carbon and C2 of the thiazole ring in the crystal structure proposed to be of the radical intermediate, it was suggested that the substrate-derived radical is a σ/n-type acetyl radical with most spin density on the substrate alpha carbon (*15, 16*). However, computational studies and EPR spectroscopy using isotopically labeled pyruvate and TPP support a π-type radical which is delocalized over the hydroxyethyl moiety and the thiazole ring of TPP (*17*). One proposed role for CoA in PFOR and other OFORs is to generate a highly reducing anionic intermediate that could transfer electrons to the clusters (*18*), and the same role has been proposed for phosphate in *Lp*POX (*14*).

From a cellular viewpoint, the purpose of CoA in most OFORs is likely to take advantage of activation of the alpha carbon of the substrate to preserve the free energy of the substrate transformation in the formation of an energy-rich CoA ester for further reactions in the cell. *Lp*POX uses phosphate for the same purpose (acetyl-phosphate is produced). From a catalytic standpoint, it has been proposed that anionic CoA (phosphate in the case of *Lp*POX) provides the driving force necessary for transferring the second electron (the radical electron) out of the active site to the iron-sulfur clusters (*7*). This is

an uphill reaction in the absence of CoA, and CoA binding is proposed to lower the redox potential of the radical species.

Although the catalytic cycle described above is straightforward with respect to pyruvate binding, some TPP-dependent enzymes display different reactivities toward the substrate in the two active sites of their dimers. One explanation for this is stabilization of different tautomers of the pyrimidine ring of TPP in the two active sites. Formation of the 1,4-iminopyrimidine tautomer of the pyrimidine ring of TPP is required for deprotonation of C2 of the thiazole ring to form the active ylide, and some TPP-dependent enzymes, including *Lp*POX, contain a mixture of pyrimidine ring tautomers in the absence of substrate and after binding of a substrate analogue (*19*). In the E1 component of human pyruvate dehydrogenase, it has been shown that one of the two TPP molecules bound to an enzyme monomer is able to be ionized quickly at C2 of the thiazole ring, while the other is ionized three orders of magnitude more slowly, and that the two TPP sites exhibit different substrate binding and turnover kinetics (*20*). A proton wire between the two active sites has been proposed to coordinate the states of the pyrimidine rings, with one site receiving a proton as the other site is deprotonated (*21*).

Although OOR does not use CoA, we hypothesize that its catalytic mechanism is similar to the mechanisms of other OFOR enzymes, based on its sequence similarity and likely structural similarity to other OFORs. The sequence of OOR is most similar to sequences of OFOR enzymes, particularly to pyruvate and 2-oxoisovalerate:Fd oxidoreductases from *Pyrococcus furiosus* and has conserved residues that are involved in cofactor and substrate binding. As was expected from sequence analysis, purified OOR contains almost one mole of TPP, 1-2 moles of Mg^{2+}, and three Fe_4S_4 clusters per mole of

enzyme like other members of the OFOR family, and like other OFORs, it forms a dimer containing two active sites.

In Chapter II, we described a proposed catalytic mechanism similar to that of PFOR, in which oxalate binds and reacts with TPP to form oxalyl-TPP, followed by decarboxylation, producing an anionic formyl-TPP intermediate. We proposed that negatively charged oxalyl- and formyl-TPP intermediates may be stabilized by protonation by a general base on the enzyme. We hypothesized that the anionic formyl-TPP adduct and its one-electron oxidized radical form would be less stable than their counterparts in the PFOR mechanism, and would quickly be oxidized as electrons are passed to the Fe_4S_4 clusters. Since these clusters are arranged in a line leading from the active site to the surface of the protein in the homologous *D. africanus* PFOR, based on the sequence homology between the two proteins, a similar arrangement is likely to be found in OOR. Although the electrons should leave the active site one at a time, since they are presumably going through a series of one electron acceptors (the clusters), electron transfer may be fast enough that there would be no appreciable accumulation of a substrate-derived radical species. Oxidation of the formyl-TPP would give carboxyl-TPP, which may be hydrolyzed to form bicarbonate or may be released as CO_2.

In this chapter, we describe work to test the hypothesis that OOR forms stable substrate-derived radicals on TPP. We provide further evidence that OOR does not catalyze the reaction of 2-oxoacid substrates with CoA, and hypothesize that the nature of the substrate controls the stability of the radical. According to our hypothesis, a radical derived from oxalate would be less stable than those derived from pyruvate or other singly negatively charged 2-oxoacids, since the oxalate-derived radical is expected to be

an anionic formyl-radical, which may be more similar in its redox potential to the anionic radicals proposed to be formed when CoA and phosphate react with the hydroxyethyl-TPP radicals on PFOR and *Lp*POX than to the un-reacted hydroxyethyl-TPP radical itself.

In the work described below, we show that OOR forms a substrate-derived radical on TPP like the radicals formed on other 2-OFOR enzymes, as shown below by experiments with pyruvate. Unlike in other 2-OFOR enzymes, this radical does not decay quickly in the presence of CoA. To characterize the role of this radical in oxalate turnover by OOR, we have used stopped-flow experiments to look at the reaction of oxalate with OOR. We are not able to predict the rate constant for decay of the radical from these experiments. However, these experiments show that the mechanism of oxalate oxidation is complex, with significant concentrations of two different forms of the enzyme reacting with oxalate. We propose two models to explain this behavior. In the first model, OOR reacts with oxalate with half-of-sites reactivity, in which one active site in each dimer reacts quickly while the other reacts slowly. In the second model, a second oxalate molecule binds during the catalytic cycle. Further experiments will be required to distinguish between these models and to find the best conditions for detecting the oxalate-derived radical on OOR, in order to test the hypothesis that the oxalate-derived radical is inherently less stable than radicals derived from singly negatively charged 2-oxoacids, such as pyruvate.

3.2 Experimental procedures

3.2.1 *Growth of M. thermoacetica and protein purification*

M. thermoacetica ATCC 39073 was grown at 55 ^{o}C in a 10 L fermentor that was continually bubbled with CO_2 during growth. The medium was described before (*5*). All cells used for OOR purification were grown on 20 mM glucose and 28 mM sodium oxalate. Cells were harvested during exponential growth by centrifugation under CO_2 or N_2 and were stored at -80^{o}C until use.

All protein purification steps and subsequent enzymatic manipulations were done in a Vacuum Atmospheres (Hawthorne, CA) anaerobic chamber maintained at less than 4 ppm O_2. OOR was purified as described (*5*), except that the red agarose step was omitted. At the end of the prep, fractions containing OOR were pooled, buffer exchanged into 50 mM Tris-HCl, pH 8.1 with 2 mM DTT, and concentrated to 316 μM for storage. The specific activity of purified OOR, measured at 25 ^{o}C was 0.04 U/mg.

3.2.2 *Preparation of thionin-oxidized OOR*

Oxidized OOR was prepared by adding small aliquots of an approximately 20 mM thionin solution to a sample of 316 μM OOR, with mixing after each addition. Thionin reduction by OOR took place within a few seconds after mixing. Thionin was added until no change in its color was seen upon further addition (i.e. the protein/thionin solution remained dark purple after mixing). Alternatively, aliquots of approximately 80 μM OOR were mixed with small amounts of thionin in a 0.2 cm path length cuvette, to achieve the desired oxidation state. Oxidized OOR was dialyzed against three changes of a 300-fold excess of 50 mM Tris-HCl, pH 8.0, with equilibration for at least 8 hours in

each change of buffer. After this dialysis, the UV-visible spectrum of OOR showed no evidence of thionin contamination. The final dialysis buffer was saved for diluting enzyme and substrate in subsequent experiments.

3.2.3 *Enzyme assays*

OOR activity was measured in 50 mM Tris-HCl, 2 mM DTT, pH 8.0. Assays at 25 ^{o}C were done in the anaerobic chamber, using a UV-visible spectrophotometer from Ocean Optics (Dunedin, FL). For steady-state assays, 1 mM sodium oxalate and 10 mM methyl viologen were used and the reduction of methyl viologen was followed at 578 nm (ε_{578} = 9.7 mM^{-1} cm^{-1}). In all assays, calculations were based on the assumption that oxidation of one mole of oxalate produces two moles of electrons.

To measure the effect of pyruvate on OOR activity, 10.9 µM OOR_{ox} was mixed with 1 mM pyruvate in 50 mM Tris-HCl, pH 8.0. The UV-visible absorbance of OOR was monitored to during the reaction of OOR with pyruvate. Based on the reduction of the Fe_4S_4 clusters, the reaction of OOR with pyruvate reached equilibrium within 120 minutes. Before assaying the enzyme, excess pyruvate was removed by concentrating and diluting OOR in 50 mM Tris-HCl, pH 8.0, using 10 kDa MWCO microcentrifuge concentrators (Millipore, Billerica, MA), using six cycles of nine-fold concentration and dilution in fresh buffer. The activity of pyruvate-incubated OOR was measured as described above, and was compared to the activities of a sample of OOR incubated at the same time in 1 mM oxalate and a sample of OOR_{ox}, both buffer exchanged in the same way.

3.2.4 *UV-visible spectroscopy*

OOR was diluted to approximately 4 μM in 50 mM Tris-HCl, pH 8.0, with or without 2 mM DTT. The enzyme was reduced at 25 ^{o}C by adding 100 μM sodium oxalate or 5-10 μM sodium dithionite. To measure the spectrum of the oxidized protein, OOR was oxidized with thionin and dialyzed, as described above.

3.2.5 *EPR spectroscopy*

The EPR spectrum of as-isolated OOR was measured to determine the number of reactive iron-sulfur clusters on OOR, to attempt to determine whether these clusters have the same or different potentials, and to see if an oxalate-derived radical could be detected after hand-mixing oxalate and OOR, and to study the reaction of pyruvate with OOR. Comparison of the UV-visible spectrum of this protein with dithionite-reduced OOR showed that the protein had approximately 1.8 iron-sulfur clusters per monomer already reduced. Sodium oxalate (100 μM, final) was added to completely reduce the protein. EPR spectra were collected at 9 K and the parameters were as follows: receiver gain, 2 x 10^2; modulation frequency, 100 kHz; modulation amplitude, 10 G; center field, 3450 or 3500 G; sweep width, 700 or 2000 G; and microwave power, 0.129 mW. The double integrals of the EPR signals were compared to that of a 1 mM copper(II) perchlorate standard to determine the number of spins per monomeric unit.

The pyruvate-derived radical on OOR was seen by EPR spectroscopy. 205 μM OOR was mixed with 1 mM CH_3- or CD_3-labeled pyruvate and incubated at 25 ^{o}C for 90 minutes. Each sample was split in half, and 1 mM CoA was added to one part from each sample. Samples were frozen after ten minutes additional incubation. EPR parameters

were receiver gain, 2 x 10^5; modulation frequency, 100 kHz; modulation amplitude, 0.4 G; center field, 3350 G; sweep width, 100 G; microwave power, 0.515 milliwatts; temperature, 70 K.

3.2.6 *UV-visible stopped-flow data collection and analysis*

The OOR used for stopped-flow experiments was first oxidized by thionin, then dialyzed, as described above. To make an oxalate stock solution, sodium oxalate and oxalic acid were dissolved in dialysis buffer to make separate 100 mM solutions. The pH of a separate aliquot of the buffer was measured as 8.02. The oxalic acid solution was used to adjust the pH of the sodium oxalate solution downward to 8.02. Stopped-flow experiments were done using a UV-visible stopped-flow (Applied Photophysics, Leatherhead, UK) set up in an anaerobic chamber (Vacuum Atmospheres, Hawthorne, CA) maintained at less than 1 ppm O_2. The temperature was maintained by a circulating water bath within the chamber that was connected to the stopped-flow instrument. The UV-visible spectrometer was equipped with a monochromator, which was used with entrance and exit slits set to 0.5 mm to collect data at 420 nm. The stopped-flow was also used with a photodiode array detector to monitor the overall spectral changes above 325 nm. The path length was 1 cm. Dilutions of OOR and oxalate stock solutions were made in the dialysis buffer.

Individual stopped-flow traces at 420 nm were fit by a triple exponential equation. The dependences of observed rate constants k_{obs1} and k_{obs3} on the oxalate concentration were shown to be hyperbolic, as described below, and were fit by Equation 3.1, where a,

b, and *c* are combinations of microscopic rate constants for steps in the reaction of OOR with oxalate.

$$k_{obs} = \frac{a * [oxalate] + b}{[oxalate] + c} \quad (3.1)$$

3.2.7 *Miscellaneous methods*

Protein concentrations were determined by the Rose Bengal method (*22*), using a lysozyme standard. For the prep of OOR used in these experiments, the concentration of TPP bound to OOR was determined by a fluorescent thiochrome assay (*23*). Pure TPP was used as a standard. Metal concentrations were determined by ICP-OES at the Chemical Analysis Laboratory at the University of Georgia. For metal and TPP analysis, 1.1 mL of 316 μM OOR was dialyzed against two changes of 850 mL of 50 mM Tris-HCl, 2 mM DTT, pH 8.0. Metal and TPP concentrations in the protein sample were calculated after subtracting the concentrations in a sample of the dialysis buffer treated exactly as was the protein. TPP and metal concentrations were similar to those reported in Chapter II.

3.3 Results

3.3.1 *Equilibrium of partial OOR reactions in the presence and absence of CO_2*

The difference spectrum of oxidized minus oxalate-reduced OOR has maxima at 316 and 428 nm, and the largest changes in the spectrum are seen between 300 and 500 nm (Figure 3.1). The same changes are seen when OOR is reduced by dithionite, and we

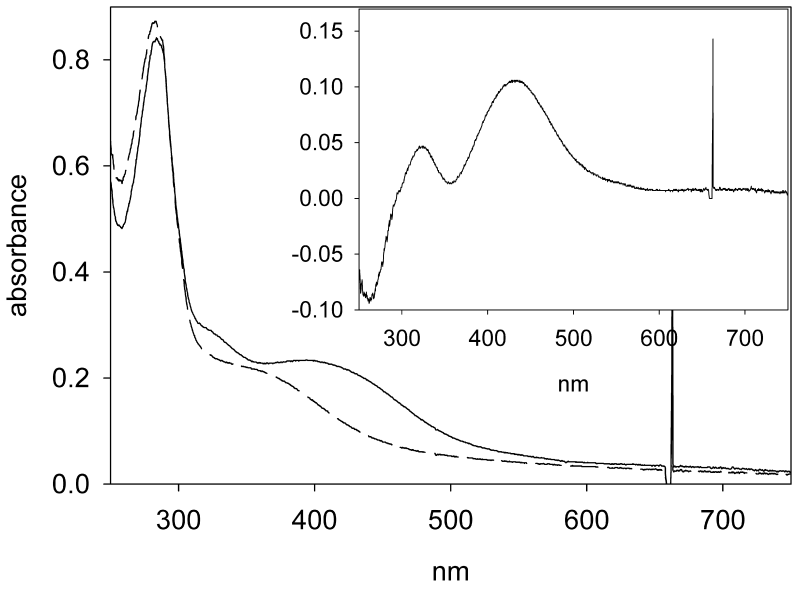

Figure 3.1. UV-visible spectra of oxidized and reduced OOR. Solid line: 3.4 μM OOR oxidized by thionin, and dashed line: thirty minutes after adding 50 μM oxalate. Inset: oxidized spectrum minus reduced spectrum.

showed in our previous work that both reductants produce EPR signals on OOR corresponding to about three $[Fe_4S_4]^{1+}$ clusters per OOR monomer. Since OOR has three $[Fe_4S_4]^{2+/1+}$ clusters, complete reduction of OOR by oxalate requires oxidation of more than one mole of oxalate per mole of OOR. The extent of reduction of OOR is less in the stopped-flow experiments described below than in an open cuvette, even when the same solutions are used for both experiments. A maximum of only 2.2 $[Fe_4S_4]^{2+/1+}$ clusters underwent reduction in the stopped-flow experiments, corresponding to oxidation of a little more than one mole of oxalate per mole of OOR. This could be explained if the equilibrium of the first half reaction of OOR, including oxalate binding, decarboxylation, reduction of the iron-sulfur clusters, and CO_2 release, is affected by the concentration of CO_2, the product, in solution. In the anaerobic chamber under an atmosphere of pure N_2, the equilibrium of this reaction should strongly favor CO_2 release from solution. This

hypothesis is supported by the observation that when 5 μM OOR was reduced by addition of 700 μM oxalate (concentrations similar to those used in stopped-flow experiments) in a stoppered cuvette that had been sparged with CO_2, only 2.3 [Fe_4S_4] clusters per OOR were reduced. However, this hypothesis should be tested further by measuring the overall equilibrium of the OOR reaction.

3.3.2 *Reaction of pyruvate with OOR and formation of a pyruvate-derived radical on OOR*

We previously showed that OOR can oxidize several 2-oxoacids besides oxalate (*5*). When OOR was mixed with 1 mM pyruvate and 10 mM methyl viologen, the amount of methyl viologen reduced approximated two moles per mole of OOR, although precise measurement of the stoichiometry is complicated by the facile photoreduction of methyl viologen. This suggested that OOR may not be able to complete its catalytic cycle with pyruvate as a substrate. Since the OOR catalytic cycle is hypothesized to contain intermediates covalently bound to TPP, we hypothesized that pyruvate may be a covalent inhibitor of OOR.

Pyruvate did not completely reduce the iron-sulfur clusters of either oxidized or partly reduced OOR, judging by the decrease in absorbance at 420 nm when pyruvate was mixed with OOR (Figure 3.2). Using an extinction coefficient of 0.0081 $\mu M^{-1}cm^{-1}$, the decrease in absorbance at 420 nm was equivalent to reduction of eight and sixteen percent of the iron-sulfur clusters in two samples of thionin-oxidized OOR prepared at different times, and to reduction of twenty-six percent of all of the iron-sulfur clusters in a sample of as-isolated OOR. The amount of reduction of the Fe_4S_4 clusters increased by

0.36 to 0.59 reduced clusters per OOR when as-isolated OOR was mixed with pyruvate, as monitored by EPR spectroscopy at 10K, where the spectrum of the reduced Fe_4S_4 clusters is seen (Figures 3.3 and 3.4). The spectra of OOR mixed with 1 mM pyruvate differed from those of oxalate-reduced and dithionite-reduced OOR. The UV-visible spectra of oxalate- and dithionite-reduced OOR show a decrease in absorbance between 300 and 600 nm, while the absorbance between 300 and 400 nm increased when OOR was incubated with pyruvate (Figure 3.2). The EPR spectrum of pyruvate-incubated OOR measured at 10K (Figure 3.4) is more complicated than those of as-isolated and oxalate- and dithionite-reduced OOR, which share similar EPR spectra (*5*), although it is not clear what changes give rise to the alterations in the spectra.

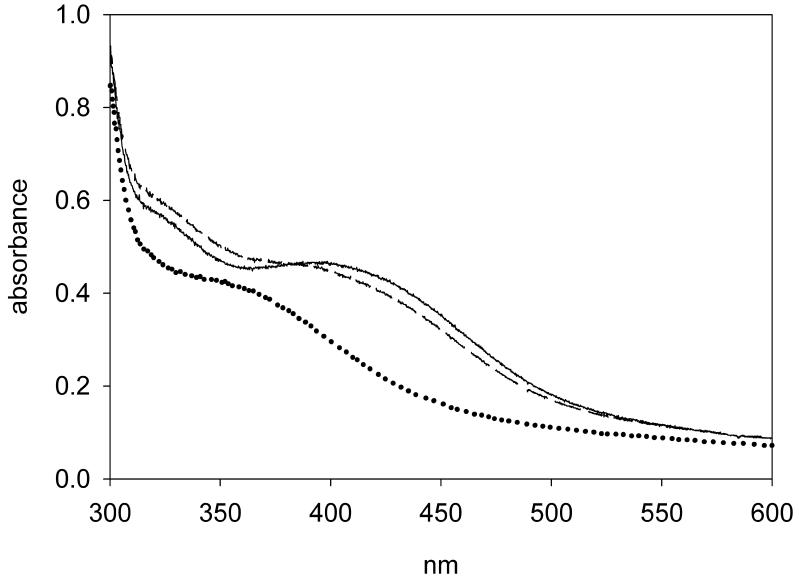

Figure 3.2. UV-visible spectra of pyruvate- and oxalate-reduced OOR. 8 μM OOR_{ox} (solid line) was incubated with 1 mM pyruvate (dashed line) or oxalate (dotted line) until no further change in either spectrum was seen.

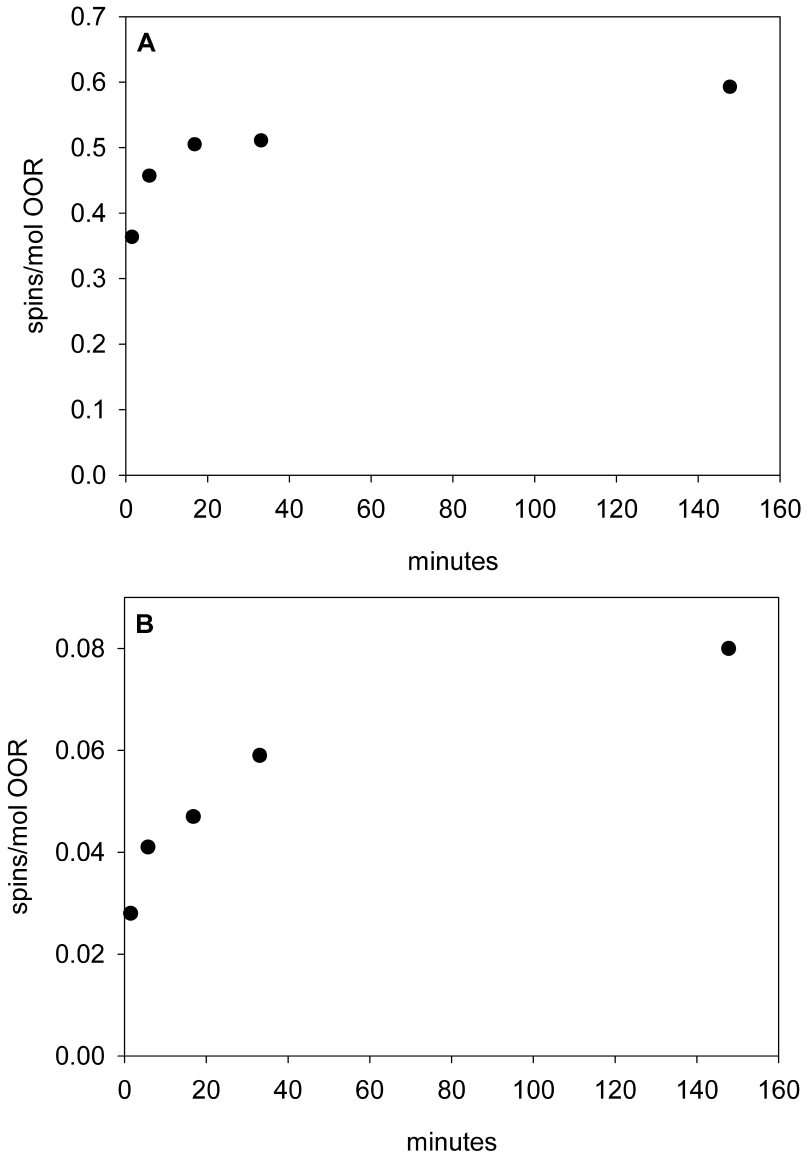

Figure 3.3. Quantitation of EPR signals produced when as-isolated (partly reduced) OOR was incubated with 1 mM pyruvate. 38 μM OOR was mixed with 1 mM pyruvate in 50 mM tris-HCl, pH 8.1. EPR samples were frozen after 1.5, 6, 17, 33 and 148 minutes. EPR spectra were integrated, and concentrations were calculated by comparison to a 1 mM copper perchlorate standard. *A*. Amount of the previously identified $[Fe_4S_4]^{1+}$, spectra were measured at 10K. Other EPR parameters were: receiver gain, 2 x 10^3; modulation frequency, 100 kHz; modulation amplitude, 10 G; center field, 3500 G; sweep width, 2000 G; microwave power, 0.103 milliwatts. *B*. Amount of the pyruvate-derived radical, spectra were measured at 70K. Other EPR parameters were: receiver gain, 2 x 10^4; modulation frequency, 100 kHz; modulation amplitude, 10 G; center field, 3500 G; sweep width, 2000 G; microwave power, 0.515 milliwatts.

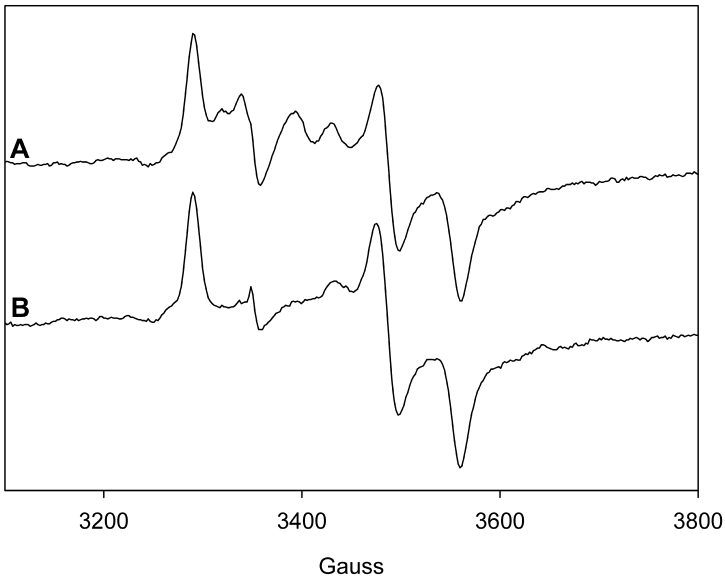

Figure 3.4. EPR spectra of as-isolated, partly reduced OOR, and of OOR incubated with pyruvate, measured at 10K. *A*. 38 μM OOR was mixed with 1 mM pyruvate in 50 mM tris-HCl, pH 8.1. The sample was frozen 17 minutes after mixing. *B*. 38 μM OOR in its as-isolated oxidation state, diluted in 50 mM tris-HCl, pH 8.1. EPR parameters are the same as in Figure 3.3A.

After incubation with 1 mM pyruvate for 20 hours and buffer-exchange to remove excess pyruvate, the activity of pyruvate-treated OOR was reduced eight-fold relative to that of untreated, buffer exchanged OOR (from 0.017 $\pm$ 0.001 U mg^{-1} to 0.002 $\pm$ 0.0006 U mg^{-1}). The almost complete disappearance of OOR activity in the pyruvate-treated sample indicates that almost all of the OOR was inhibited by pyruvate, even though the incomplete reduction of OOR might seem to suggest that only a fraction of the OOR reacted with pyruvate. An average of 0.58 clusters/OOR were reduced by pyruvate. 0.08 clusters/OOR can be attributed to the electron released when the radical is formed (as measured by EPR at 70K, see below), so approximately 0.5 clusters/OOR should be from the two-electron reduced form, which means 25 percent of the OOR would be in this state. This could be explained if the equilibrium of the reaction with pyruvate does not favor reduction of the iron-sulfur clusters.

In our previous work, we showed that addition of CoA to assays of pyruvate oxidation coupled to methyl viologen reduction by OOR had no effect on the rate of the reaction (*5*). To test whether phosphorolysis of pyruvate-derived intermediates could restore OOR activity, 50 mM KPi, pH 7.4 was added to assays of pyruvate-treated OOR, but no increase in the rate of oxalate-dependent methyl viologen reduction was seen over one hour.

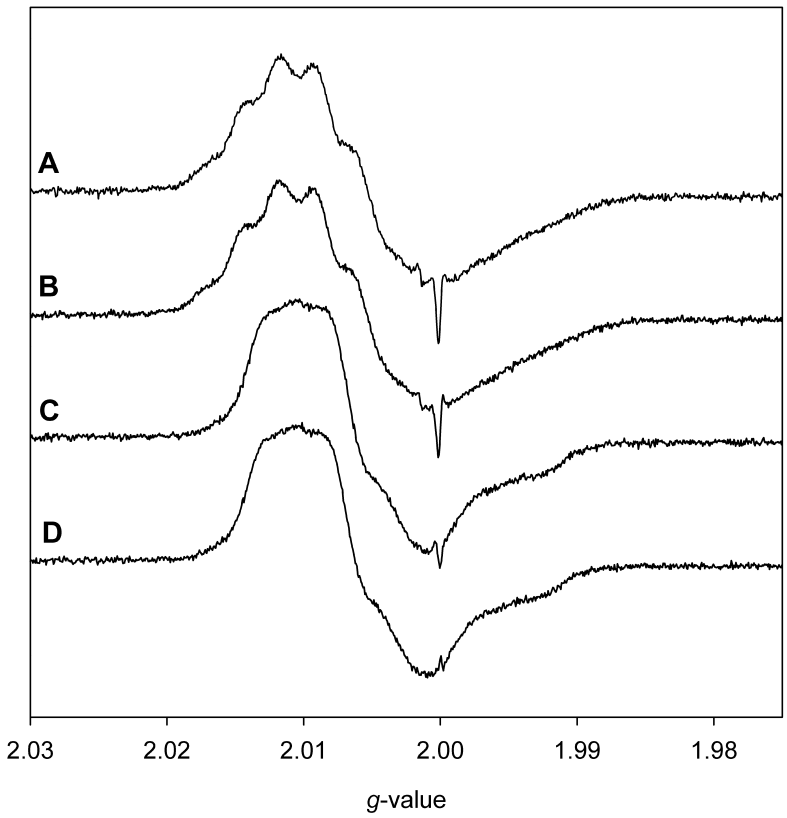

Figure 3.5. EPR spectrum of the pyruvate-derived radical on OOR. 205 μM OOR was mixed with 1 mM CH_3- (A) or CD_3-labeled pyruvate (C) and incubated at 25 °C for 90 minutes. Each sample was split in half, and 1 mM CoA was added to one part from each sample (B: CH_3-labeled pyruvate plus CoA, D: CD_3-labeled pyruvate plus CoA). Samples were frozen after ten minutes additional incubation. EPR parameters were receiver gain, 2 x 10^5; modulation frequency, 100 kHz; modulation amplitude, 0.4 G; center field, 3350 G; sweep width, 100 G; microwave power, 0.515 milliwatts; temperature, 70 K. All four spectra have the same intensity scale. The sharp feature at g = 2.00 is seen in spectra of the EPR cavity. This radical has different saturation behavior than the HE-TPP radical.

A fraction of OOR incubated with pyruvate contains a pyruvate-derived radical, which can be seen in EPR spectra at 70K. Figure 3.3 shows the increase in the concentration of this radical over time as OOR is incubated with 1 mM pyruvate. The pyruvate-derived radical is very similar to the hydroxyethyl-TPP radical that is seen when PFOR is mixed with pyruvate in the absence of CoA (*17*). When OOR is incubated with CD_3-labeled pyruvate, hyperfine splittings in the radical spectrum are lost (Figure 3.5). A similar spectrum is seen when PFOR is treated with deuterated pyruvate. Unlike in PFOR, where CoA addition increases the rate of decay of the radical by 10^5-fold, addition of CoA to OOR and pyruvate mixtures ten minutes before freezing EPR samples had no effect on the spectra of the radical (Figure 3.5).

3.3.3 *UV-visible stopped-flow of the first half-reaction*

Because experiments with pyruvate showed that OOR is able to form a radical like those formed on other 2-OFOR enzymes during catalysis, we wanted to study the kinetics of the reaction with oxalate to see whether the formyl-TPP radical hypothesized as an intermediate would accumulate appreciably at any time during the reaction. Stopped-flow experiments were used to follow the reduction of oxidized OOR by oxalate at 420 nm. There is some evidence of subtle spectral changes between 300 and 450 nm as covalent adducts form in other TPP-dependent enzymes. These changes are from the conjugated enamine intermediate and from changes in the tautomerization state of the pyrimidine ring of TPP (*24*) but the main spectral change observed during the reaction of OOR with oxalate is the decrease in the absorbance of the iron-sulfur clusters.

Stopped-flow data were collected at several oxalate concentrations, using either a photodiode array detector or a monochromator. When the photodiode array detector was used, there were significant changes in the baseline over 200 s, seen both when OOR was rapidly mixed with buffer, and when buffer was mixed with buffer. These changes in absorbance were on the same order of magnitude as the amplitudes of the first two phases in the reaction of enzyme with oxalate, so these data could not be cleanly analyzed. However, it is clear from the photodiode array experiments that the overall reaction of OOR with oxalate in the stopped-flow instrument gives spectral changes like those seen when the enzyme and substrate are manually mixed (i.e. like the changes shown in Figure 3.1).

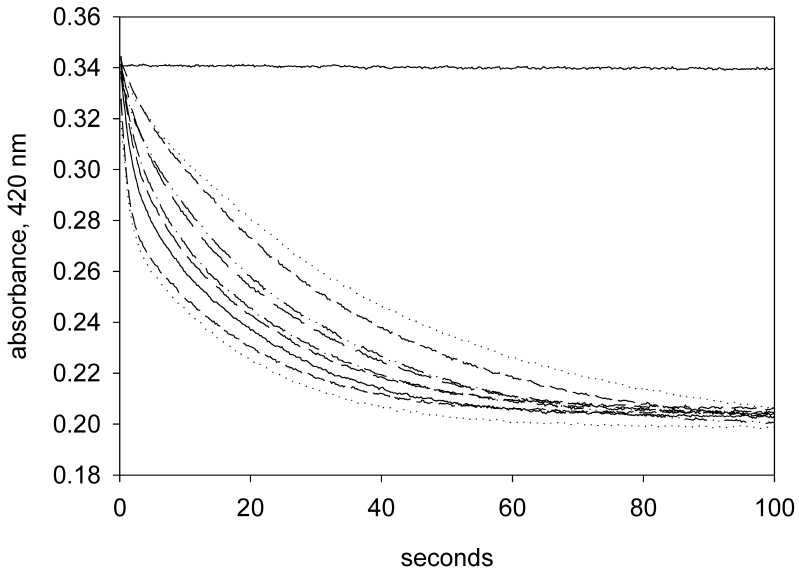

Figure 3.6 Representative stopped-flow traces of the reaction of oxidized OOR with oxalate. The concentration of OOR after mixing was 8 μM. Concentrations of oxalate after mixing vary from 25 to 700 μM. The nearly flat trace is 8 μM OOR (after mixing) shot against buffer without oxalate.

When stopped-flow experiments were performed using the monochromator, there was only a slight linear decrease in absorbance over time when OOR was mixed with buffer. Representative stopped-flow traces are shown in Figure 3.6. In our previous work, the K_m for oxalate was found to be 60 μM at pH 8.0 (*5*). 8 μM OOR was reacted with oxalate over the range from 10 μM to 700 μM. Kinetic traces of fully oxidized OOR reacted with oxalate were fit by a triple exponential equation (Figure 3.7), with a fast decrease in absorbance followed by a lag and a slower decrease. The reactions reached equilibrium after a total change in amplitude consistent with reduction of 2.2 iron-sulfur clusters per OOR monomer. At 700 μM oxalate, the relative amplitudes of the first and third phases were approximately 0.06 and 0.11, which correspond to 0.92 and 1.7 iron-sulfur clusters reduced per OOR However, the exponentials overlap, so these are not the actual amounts of cluster reduced in each phase. The overall reduction was of 2.2 clusters per OOR. All reactions reached equilibrium by 200 s, and no further reduction was seen over an additional 840 s (not shown).

As demonstrated in Figure 3.7 for one stopped-flow trace, single exponential fits were unsatisfactory. Both double and triple exponential equations fit the data much better, although there were still deviations of the fits from the data that were consistent over all stopped-flow traces. The size of these deviations of the fits from the data is small relative to the overall absorbance changes in the reaction. The additional complexity in the data could come from a small population of the enzyme that reacts differently with oxalate (e. g., enzyme molecules that are damaged in some way and are less active than the bulk of the molecules in solution), or from subtle changes in the absorbance spectrum

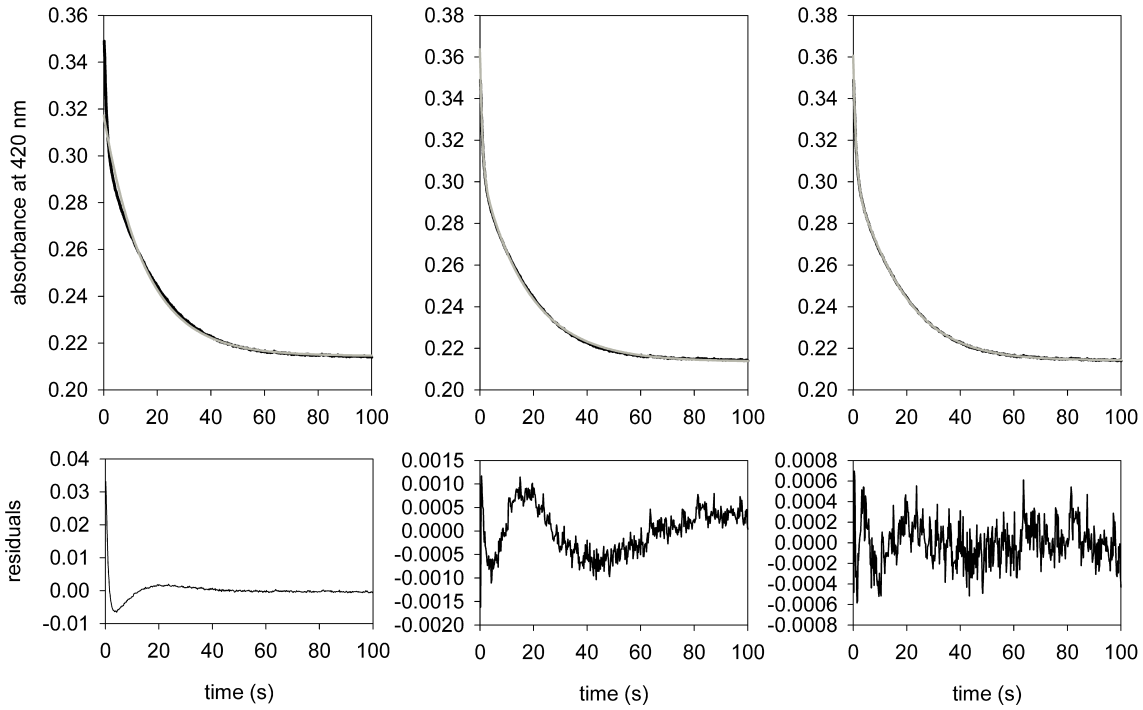

Figure 3.7. Fits of exponential equations to data from reaction of OOR with oxalate. The average of three stopped-flow traces of 8 μM OOR reacting with 700 μM oxalate was fit with a single (left), double (center) or triple (right) exponential equation. Data is shown in black, fits are shown in grey. The residuals from each fit are shown in the lower panels.

during the reaction that are masked by the larger changes in absorbance from the iron-sulfur clusters.

Although the best fit to the stopped-flow traces at 420 nm was with a triple exponential equation, the initial fast reduction and lag were more difficult to fit than the slow reduction, particularly as the oxalate concentration was lowered, and from the initial fits, it was unclear whether either or both of these observed rate constants were dependent on oxalate concentration. The oxalate concentration dependence of each of these observed rate constants was tested by holding k_{obs1}, k_{obs2} or both rate constants to a constant value (the average of each observed rate constant from the initial fits of three different traces at 700 μM oxalate was used), and allowing the fitting software to find the

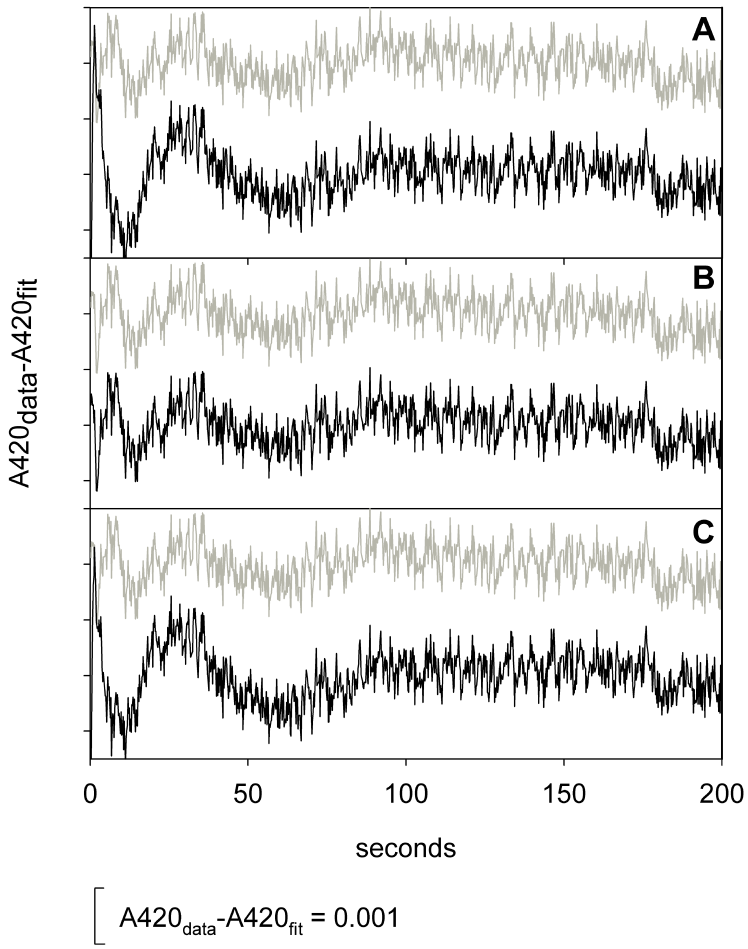

Figure 3.8. Residuals from triple exponential fits of a stopped flow trace at 420 nm. Oxalate was 120 μM, and OOR was 8 μM. In each panel, the grey trace shows the residuals of the triple exponential fit to seven parameters. The black trace shows the residuals of a fit of five or six parameters with one or more k_{obs} set at a certain value. The y-axis scale is the same in all three panels. The scale of the x-axis is shown by the half-bracket at the bottom of the figure. *A*. $k_{obs}1$ set at 0.908 s^{-1}. *B*. $k_{obs}2$ set at 0.118 s^{-1}. *C*. $k_{obs}1$ set at 0.908 s^{-1} and $k_{obs}2$ set at 0.118 s^{-1}.

best fit for the other six variables in the triple exponential equation. The effect on one stopped-flow trace (8 μM OOR vs. 120 μM oxalate) of holding k_{obs1} at 0.908 s^{-1}, holding k_{obs2} at 0.118 s^{-1}, and of constraining both values is shown in Figure 3.8. Refitting these data with k_{obs2} held constant at 0.118 s^{-1} (it was 0.078 s^{-1} in the initial fit) made no noticeable difference in the residuals from the fit, while refitting the same trace with k_{obs1} held constant at 0.908 s^{-1} (0.418 s^{-1} in the original fit), or with both k_{obs1} and k_{obs2} held

constant at the values given gave worse fits. From the above analysis, it appeared that k_{obs2} does not necessarily vary with the oxalate concentration[6], since holding it to a constant value had a relatively small effect on the quality of the fit, so all data were fit again with triple exponential equations, with k_{obs2} held constant at 0.118 s^{-1}. In these fits, k_{obs1} and k_{obs3} were both dependent on the oxalate concentration.

The dependences of k_{obs1} and k_{obs3} on oxalate are shown in Figure 3.9. Each apparent rate constant increased hyperbolically as the oxalate concentration was increased. The oxalate dependence of each apparent rate constant was fit with equation 3.1. Parameters from the fits are given in Table 3.1.

As is shown in Table 3.1 and Figure 3.9, the dependences of k_{obs1} and k_{obs3} on oxalate are very different, so the microscopic rate constants that give rise to the dependence of k_{obs1} on oxalate must be different than those that give rise to the dependence of k_{obs3} on oxalate. This is best explained by a kinetic model in which significant amounts of two different forms of the enzyme bind oxalate. Two such kinetic schemes are shown below. In *Scheme 1*, two forms of the enzyme, denoted by E_{ox} and E_{ox}', are in equilibrium. Each form can bind and react with oxalate, giving rise to two separate oxalate-dependent steps (denoted by rate constants k_1/k_2 and k_3/k_4). As *Scheme 1*

Table 3.1. Parameters from hyperbolic fits of k_{obs1} and k_{obs3}.

	k_{obs1}	k_{obs3}
a	1.4 ± 0.1 s^{-1}	0.070 ± 0.001 s^{-1}
b	27 ± 8 μM s^{-1}	0.32 ± 0.12 μM s^{-1}
c	420 ± 56 μM	46 ± 5 μM
amplitude	0.06 (~0.8 clusters/OOR)	0.12-0.16 (~2 clusters/OOR)

[6] It was suggested that the phase defined by k_{obs2} may also be attributed to a small fraction of a less-active form of the enzyme, and that a kinetic scheme that takes into account this lag phase may be unjustifiably more complicated than is necessary. Fits of all of the stopped-flow traces with double, rather than triple exponential equations gave the same dependence of the remaining two apparent rate constants on oxalate.

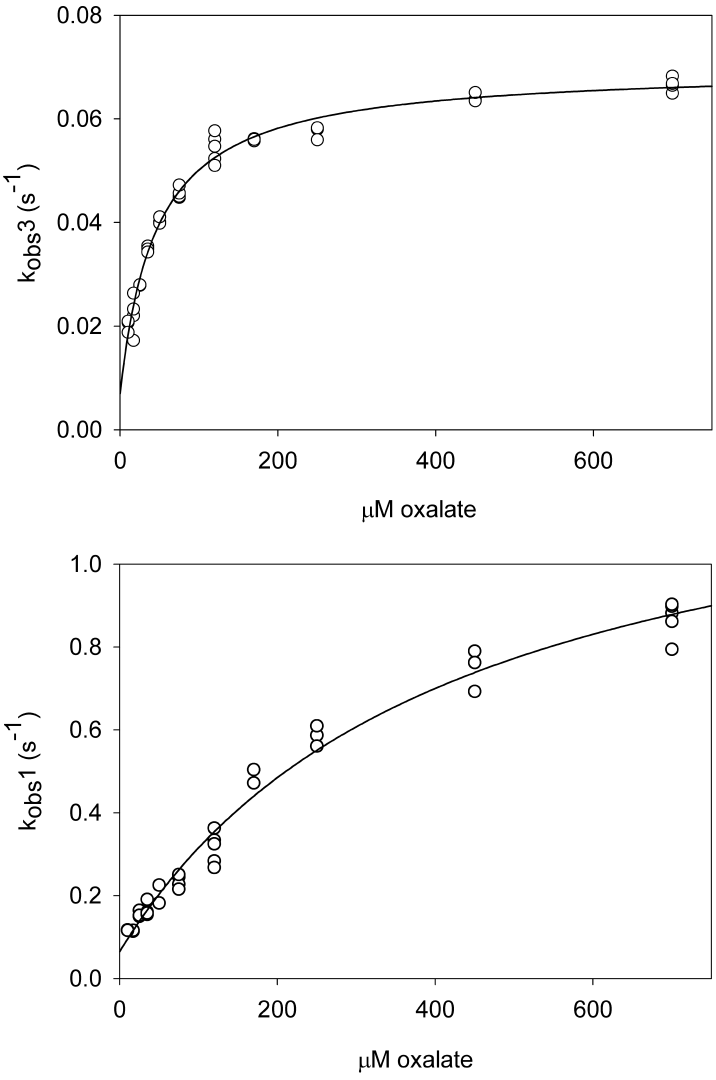

Figure 3.9. Dependence of k_{obs3} and k_{obs1} on oxalate concentration when k_{obs2} is set at 0.118 s^{-1}. 8 μM OOR and 25-700 μM oxalate were mixed in the stopped-flow instrument at 25 °C, and the absorbance at 420 nm was measured over 200 s. Stopped-flow traces were fit with triple exponential equations, with k_{obs2} set at 0.118 s^{-1}. The open circles are parameters from these fits to individual stopped-flow traces. Top panel, k_{obs1}, bottom panel, k_{obs3} vs. oxalate concentration. The lines show the best fits of Eq. 3.1.

is drawn here, each pair of intermediates, E_{ox} and E_{ox}', E-oxalate and E'-oxalate, and E_{red} and E_{red}' is in equilibrium. E_{ox} and E_{ox}' should be in equilibrium, to produce the two forms of OOR that would react with oxalate, but equilibration between the other enzyme forms may not be necessary.

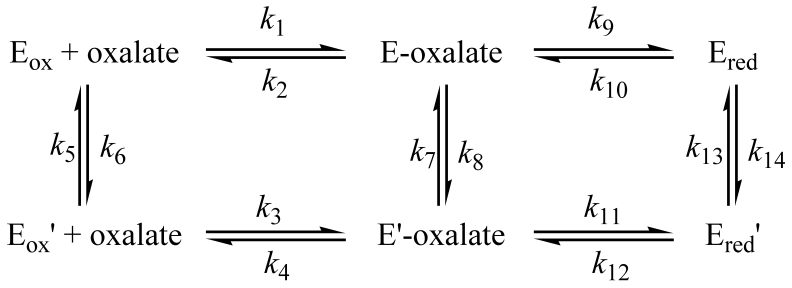

Scheme 1

In *Scheme 2*, the dependence of two different parts of the reaction on oxalate is explained by oxalate binding at two separate steps in the catalytic cycle. This could be understood as binding of a first oxalate molecule and partial reduction of the iron-sulfur clusters, followed by binding of a second oxalate to drive the rest of the reduction of OOR. This scheme also predicts two different oxalate-dependent steps (denoted by rate constants k_1/k_2 and k_5/k_6).

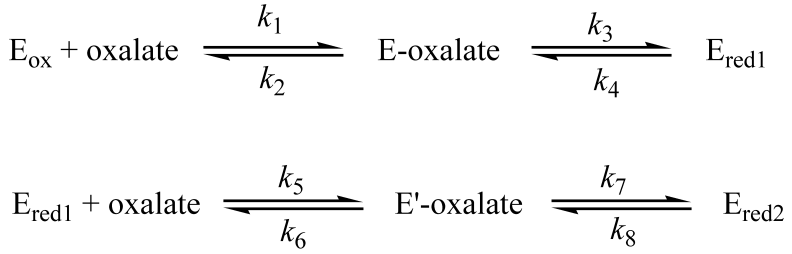

Scheme 2

3.4 Discussion

OOR is unique among the known 2-oxoacid:Fd oxidoreductases because its catalytic function is entirely CoA-independent. In other 2-oxoacid:Fd oxidoreductases, CoA plays an important mechanistic role in driving oxidation of stable substrate-derived radicals on TPP. Formation of a substrate-derived radical has been hypothesized to be intermediate in the mechanisms of all enzymes of this family. We hypothesize that a

formyl-TPP radical intermediate is formed in the OOR mechanism analogous to the intermediate radical adduct formed on other 2-OFOR enzymes when CoA reacts with the substrate-derived radicals (e.g., HE-TPP radical on PFOR). By analogy to the well-studied PFOR structure, a more or less stable radical can be hypothesized to be an obligatory intermediate in all members of the family, since the pair of electrons produced when the substrate is oxidized is passed out of the active site to the surface of the enzyme by one or more $[Fe_4S_4]^{2+/1+}$ clusters, which have been shown to be single-electron acceptors.

The specific role hypothesized for CoA in 2-OFOR enzymes is to provide the driving force necessary for transferring the second electron (the radical electron) out of the active site to the proximal iron-sulfur cluster, which has the most negative redox potential among the three clusters. The hydroxyethyl-TPP intermediate formed upon decarboxylation of lactyl-TPP quickly transfers an electron to the iron-sulfur cluster proximal to the active site (in PFOR, this cluster has a potential of -530 mV) and that electron ends up in the medial cluster approximately 33 Å from the site of spin density on the HE-TPP radical (*18*). However, the radical left by this electron transfer is proposed to be fairly stable, with a midpoint potential that is too high to drive the reduction of the proximal iron-sulfur cluster. Reaction of CoA with the radical would generate a radical anion with a midpoint potential that is significantly lower than -530 mV, thus providing a sufficient driving force to reduce the proximal cluster. A similar role has been hypothesized for phosphate in *Lp*POX, as described above.

Since OOR does not need CoA for oxalate turnover, and we have observed reduction at kinetically competent rates of all three clusters of OOR upon reaction with

oxalate, it is likely that OOR uses a mechanism similar to that which has been shown for PFOR; thus, we propose that the radical intermediate on OOR is higher in energy than that of HE-TPP radical. We hypothesize that the structure of the radical intermediate resembles the radical anion adduct formed on PFOR when the HE-TPP radical reacts with CoA.

Consistent with this hypothesis, OOR forms the HE-TPP radical upon reaction with pyruvate, however only a single turnover can occur with the reaction halting at the stage of radical formation in about ten percent of the OOR molecules. EPR experiments provide unambiguous evidence for the pyruvate-derived HE-TPP radical on OOR because the EPR signal is nearly identical to that of the hydroxyethyl-TPP radical formed on PFOR and because substitution of deuterated pyruvate decreased the hyperfine splittings in a manner similar to that observed with PFOR. Under steady-state conditions, CoA does not increase the rate of pyruvate oxidation or lead to multiple turnovers, presumably because OOR does not bind CoA. Furthermore, the radical intermediate is not affected by the presence of CoA in the reaction mixture.

OOR is inhibited by pyruvate, even after excess pyruvate is removed from the enzyme, consistent with the formation of a covalently attached intermediate(s) that would block the active site. We propose that this inhibition results from the formation of the stable TPP-bound radical and acetyl-TPP intermediates. The UV-visible spectrum of pyruvate-incubated OOR shows an increase in absorbance between 300 and 400 nm. Circular dichroism studies with other TPP-dependent enzymes have shown that covalently bound intermediates on TPP give rise to spectral changes in this region (for

example, see (*25*)). This increase in absorbance when OOR is reacted with pyruvate may be from some stable pyruvate-derived TPP intermediate.

The experiments with pyruvate support the hypothesis that OOR acts through a mechanism similar to the PFOR mechanism, including at least transient formation of a substrate-derived radical. When oxalate is the substrate, a formyl-TPP radical is proposed as an intermediate in the OOR mechanism, by analogy to the HE-TPP radical formed after decarboxylation and one-electron oxidation of pyruvate.

We undertook stopped-flow kinetic experiments to try to resolve steps in the first half-reaction of oxalate with OOR, with the goal of assessing whether the one-electron oxidation product of oxalate (the proposed formyl-TPP radical) is relatively stable, as is the HE-TPP radical, or whether it decays quickly as the HE-TPP radical does in the presence of CoA. The kinetics of reaction of oxalate with OOR are more complicated than we expected. The only large changes in the absorbance spectrum of OOR are from the reduction of the iron-sulfur clusters, and since reduction of these clusters is likely to come at the end of the first half-reaction, we could not monitor initial steps in the reaction, making it difficult to derive microscopic rate constants from the stopped-flow data.

Although we are so far unable to derive microscopic rate constants from the stopped-flow data, some conclusions about the mechanism can be drawn from the data. From the stopped-flow experiments, we can see that OOR is reduced by approximately two electrons per active site, in two separate phases. Each reductive phase is oxalate-dependent. Since the dependences of k_{obs1} and k_{obs3} are clearly fit by different parameters, the two phases should represent different steps in the reaction of oxalate with OOR.

Based on the hypothesis that the OOR mechanism is similar to the PFOR mechanism, we can make predictions about steps that should occur in the absence of an external electron acceptor. These include (i) binding of oxalate, (ii) nucleophilic attack of the ylide form of TPP on oxalate to form an oxalyl-TPP intermediate, (iii) decarboxylation of oxalyl-TPP to make formyl-TPP, (iv) one-electron oxidation of formyl-TPP by an iron-sulfur cluster, (v) a second electron transfer from the formyl-TPP radical to an iron-sulfur cluster, and (vi) release of the second CO_2 molecule to regenerate the starting form of TPP. Of these steps, changes in the intermediates covalently bound to TPP may lead to subtle spectral changes, but the large changes in absorbance at 420 nm most likely come from the first and second reductions of the iron-sulfur clusters. The observed rate constant for the slowest phase is approximately the same as k_{cat}, so some step in the first half-reaction should be at least partly rate-limiting.

The mechanisms shown in *Scheme 1* and *Scheme 2* both explain the observed variations of k_{obs1} and k_{obs3} with oxalate concentration. *Scheme 1* proposes that oxalate can bind to different forms of the enzyme, both of which carry out the reaction, but at different rates. One chemical rationale for this scheme could be that oxalate binds to OOR molecules that have different tautomerization states of TPP with different rates for deprotonation of C2 of the thiazole ring, as is described for other TPP-dependent enzymes in the introduction to this Chapter. In this model, one active site in the OOR dimer would be easily deprotonated and react quickly with oxalate, while the other would react much more slowly.

Scheme 2 proposes that a second oxalate molecule during binds during the first half-reaction. The form of the enzyme that the second oxalate binds to is denoted as E_{red1},

which represents some partly reduced form of OOR. With *Scheme 2*, the second oxalate molecule must bind to a partly reduced form of OOR, since each oxalate-dependent phase shows a large decrease in absorbance. Binding of a second oxalate molecule would then drive the rest of the reduction of OOR.

In terms of the chemical mechanism, two hypotheses could explain the two separate reduction steps. In the first hypothesis, the first phase of the reaction includes oxalate binding and reaction with TPP, followed by decarboxylation and oxidation of formyl-TPP to form the radical and reduce one iron-sulfur cluster. This radical would be stable until binding of a second oxalate molecule would somehow drive further oxidation of the radical to reduce the second iron-sulfur cluster. This is contrary to our earlier hypothesis that the formyl-TPP radical would be strongly reducing and therefore unstable. In the second hypothesis, the first phase of the reaction includes steps up to the two-electron oxidation of the substrate, reducing two iron-sulfur clusters per OOR. The second oxalate molecule would then bind and react, and its oxidation would reduce the rest of the iron-sulfur clusters. This is consistent with the ability of both OOR and PFOR to be completely reduced (three clusters per monomer) by their substrates, but contrary to the total change in amplitude corresponding to only ~2.2 iron-sulfur clusters reduced per OOR observed in the stopped-flow experiments. However, it is possible that not all of the OOR molecules in the stopped-flow sample were active.

3.5. References

(1) Drake, H. L., and Daniel, S. L. Physiology of the thermophilic acetogen *Moorella thermoacetica*. *Res. Microbiol. 155*, 422-436.

(2) Kerby, R., and Zeikus, J. G. (1983) Growth of *Clostridium thermoaceticum* on H_2/CO_2 or CO as energy source. *Curr. Microbiol. 8*, 27-30.

(3) Daniel, S. L., Keith, E. S., Yang, H., Lin, Y.-S., and Drake, H. L. (1991) Utilization of methoxylated aromatic compounds by the acetogen *Clostridium thermoaceticum*: Expression and specificity of the CO-dependent O-demethylating activity. *Biochem. Biophys. Res. Commun. 180*, 416-422.

(4) Seifritz, C., Fröstl, J. M., Drake, H. L., and Daniel, S. L. (1999) Glycolate as a metabolic substrate for the acetogen *Moorella thermoacetica*. *FEMS Microbiol. Lett. 170*, 399-405.

(5) Pierce, E., Becker, D. F., and Ragsdale, S. W. (2010) Identification and Characterization of Oxalate Oxidoreductase, a Novel Thiamine Pyrophosphate-dependent 2-Oxoacid Oxidoreductase That Enables Anaerobic Growth on Oxalate. *J. Biol. Chem. 285*, 40515-40524.

(6) Chabriere, E., Charon, M.-H., Volbeda, A., Pieulle, L., Hatchikian, E. C., and Fontecilla-Camps, J.-C. (1999) Crystal structures of the key anaerobic enzyme pyruvate:ferredoxin oxidoreductase, free and in complex with pyruvate. *Nat. Struct. Mol. Biol. 6*, 182-190.

(7) Furdui, C., and Ragsdale, S. W. (2002) The Roles of Coenzyme A in the Pyruvate:Ferredoxin Oxidoreductase Reaction Mechanism: Rate Enhancement of Electron Transfer from a Radical Intermediate to an Iron-Sulfur Cluster. *Biochemistry 41*, 9921-9937.

(8) Cammack, R., Kerscher, L., and Oesterhelt, D. (1980) A stable free radical intermediate in the reaction of 2-oxoacid:ferredoxin oxidoreductases of *Halobacterium halobium*. *FEBS Lett. 118*, 271-273.

(9) Smith, E. T., Blamey, J. M., and Adams, M. W. (1994) Pyruvate ferredoxin oxidoreductases of the hyperthermophilic archaeon, *Pyrococcus furiosus*, and the hyperthermophilic bacterium, *Thermotoga maritima*, have different catalytic mechanisms. *Biochemistry 33*, 1008-16.

(10) Pieulle, L., Guigliarelli, B., Asso, M., Dole, F., Bernadac, A., and Hatchikian, E. C. (1995) Isolation and characterization of the pyruvate-ferredoxin oxidoreductase from the sulfate-reducing bacterium *Desulfovibrio africanus*. *Biochim. Biophys. Acta, Protein Struct. Mol. Enzymol. 1250*, 49-59.

(11) Mai, X., and Adams, M. W. (1994) Indolepyruvate ferredoxin oxidoreductase from the hyperthermophilic archaeon *Pyrococcus furiosus*. A new enzyme involved in peptide fermentation. *J. Biol. Chem. 269*, 16726-16732.

(12) Heider, J., Mai, X., and Adams, M. (1996) Characterization of 2-ketoisovalerate ferredoxin oxidoreductase, a new and reversible coenzyme A-dependent enzyme involved in peptide fermentation by hyperthermophilic archaea. *J. Bacteriol. 178*, 780-787.

(13) Menon, S., and Ragsdale, S. W. (1997) Mechanism of the *Clostridium thermoaceticum* Pyruvate:Ferredoxin Oxidoreductase: Evidence for the Common Catalytic Intermediacy of the Hydroxyethylthiamine Pyropyrosphate Radical. *Biochemistry 36*, 8484-8494.

(14) Tittmann, K., Wille, G., Golbik, R., Weidner, A., Ghisla, S., and Hübner, G. (2005) Radical Phosphate Transfer Mechanism for the Thiamin Diphosphate- and FAD-Dependent Pyruvate Oxidase from *Lactobacillus plantarum*. Kinetic Coupling of Intercofactor Electron Transfer with Phosphate Transfer to Acetyl-thiamin Diphosphate via a Transient FAD Semiquinone/Hydroxyethyl-ThDP Radical Pair. *Biochemistry 44*, 13291-13303.

(15) Chabrière, E., Vernède, X., Guigliarelli, B., Charon, M.-H., Hatchikian, E. C., and Fontecilla-Camps, J. C. (2001) Crystal Structure of the Free Radical Intermediate of Pyruvate:Ferredoxin Oxidoreductase. *Science 294*, 2559-2563.

(16) Cavazza, C., Contreras-Martel, C., Pieulle, L., Chabrière, E., Hatchikian, E. C., and Fontecilla-Camps, J. C. (2006) Flexibility of Thiamine Diphosphate Revealed by Kinetic Crystallographic Studies of the Reaction of Pyruvate-Ferredoxin Oxidoreductase with Pyruvate. *Structure 14*, 217-224.

(17) Mansoorabadi, S. O., Seravalli, J., Furdui, C., Krymov, V., Gerfen, G. J., Begley, T. P., Melnick, J., Ragsdale, S. W., and Reed, G. H. (2006) EPR Spectroscopic and Computational Characterization of the Hydroxyethylidene-Thiamine Pyrophosphate Radical Intermediate of Pyruvate:Ferredoxin Oxidoreductase. *Biochemistry 45*, 7122-7131.

(18) Astashkin, A. V., Seravalli, J., Mansoorabadi, S. O., Reed, G. H., and Ragsdale, S. W. (2006) Pulsed Electron Paramagnetic Resonance Experiments Identify the Paramagnetic Intermediates in the Pyruvate Ferredoxin Oxidoreductase Catalytic Cycle. *J. Am. Chem. Soc. 128*, 3888-3889.

(19) Nemeria, N., Chakraborty, S., Baykal, A., Korotchkina, L. G., Patel, M. S., and Jordan, F. (2007) The 1',4'-iminopyrimidine tautomer of thiamin diphosphate is poised for catalysis in asymmetric active centers on enzymes. *Proc. Natl. Acad. Sci. U S A 104*, 78-82.

(20) Seifert, F., Golbik, R., Brauer, J., Lilie, H., Schroder-Tittmann, K., Hinze, E., Korotchkina, L. G., Patel, M. S., and Tittmann, K. (2006) Direct kinetic evidence for half-of-the-sites reactivity in the E1 component of the human pyruvate

dehydrogenase multienzyme complex through alternating sites cofactor activation. *Biochemistry 45*, 12775-85.

(21) Frank, R. A., Titman, C. M., Pratap, J. V., Luisi, B. F., and Perham, R. N. (2004) A molecular switch and proton wire synchronize the active sites in thiamine enzymes. *Science 306*, 872-6.

(22) Elliott, J. I., and Brewer, J. M. (1978) The inactivation of yeast enolase by 2,3-butanedione. *Arch. Biochem. Biophys. 190*, 351-357.

(23) Penttinen, H. K. (1979) Fluorometric determination of thiamine and its mono-, di-, and triphosphate esters. *Methods Enzymol. 62*, 58-59.

(24) Jordan, F. (2003) Current mechanistic understanding of thiamin diphosphate-dependent enzymatic reactions. *Nat. Prod. Rep. 20*, 184-201.

(25) Meyer, D., Neumann, P., Parthier, C., Friedemann, R., Nemeria, N., Jordan, F., and Tittmann, K. Double duty for a conserved glutamate in pyruvate decarboxylase: evidence of the participation in stereoelectronically controlled decarboxylation and in protonation of the nascent carbanion/enamine intermediate. *Biochemistry 49*, 8197-212.

CHAPTER IV

Characterization of a Sodium Binding Site in Acetyl-CoA Synthase[7]

4.1 Introduction

Acetyl-CoA synthase (ACS) catalyzes the formation of acetyl-CoA from CO, a methyl group donated by a methylated corrinoid iron-sulfur protein, and CoA. X-ray crystal structures of bifunctional CO dehydrogenase/acetyl-CoA synthase from *Moorella thermoacetica* (*1, 2*) and monomeric acetyl-CoA synthase from *Carboxydothermus hydrogenoformans* (*3*) have been solved (Figure 4.1). The active site of ACS (the A-cluster) consists of a Ni-Ni site, with one Ni bridged by cysteine to a Fe_4S_4 cluster. This central Ni atom is referred to as the proximal Ni or Ni_p. It is thought to be the site for substrate binding and catalysis. In both the CODH/ACS and ACS only structures, ACS is made of three domains arranged in a triangle. The N-terminal domain contains α-helical and Rossmann folds. This domain binds CODH in the bifunctional enzyme, and contains part of a 70 Å channel that allows CO to pass from the CODH active site to the ACS active site without leaving the enzyme (*4, 5*). The other domains of ACS are mixed alpha helices and beta strands. The C-terminal domain contains the ligands to the Ni

[7] The previously undetected metal binding site in ACS was found by Yan Kung, during his work in Cathy Drennan's lab at the Massachusetts Institute of Technology.

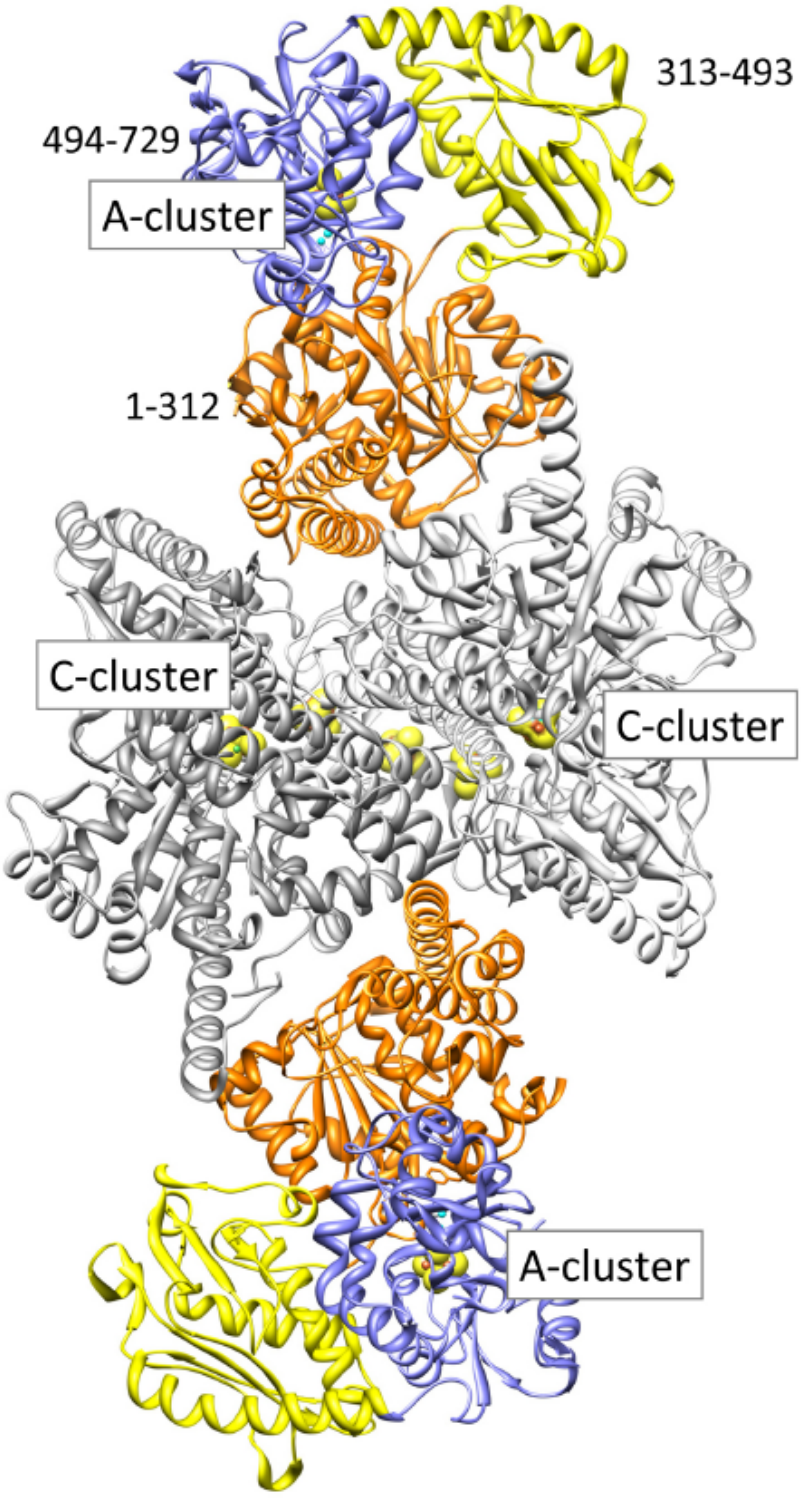

Figure 4.1. Crystal structure of *M. thermoacetica* CODH/ACS from pdb 1MJG. The CODH dimer is shown in grey, ACS domains are shown in orange (N-terminal domain), yellow (central domain) and blue (C-terminal domain). The C-cluster and A-cluster are the sites of CO_2 reduction to CO and acetyl-CoA synthesis, respectively.

and Fe atoms in the A-cluster. In *M. thermoacetica* ACS, the three domains consist of residues 1–312, 313–493 and 494–729.

ACS has been observed in open and closed conformations in X-ray crystal structures (*2*). In the closed conformation, the C-terminal domain is close to the N-terminal domain, the active site is buried in the protein, and the end of the CO channel is open to the ACS active site. In the open conformation, the N-terminal domain is farther away from the C-terminal domain, and the end of the CO channel in the N-terminal domain is closed. The middle domain moves with the C-terminal domain in this conformational change. It has been proposed that these two conformers are relevant to the catalytic mechanism, because delivery of CO to the A-cluster would require the enzyme to be in the closed state and interaction between the methylated CFeSP and ACS would require the open state. Therefore, large conformational changes between the closed and open states are expected to occur during the catalytic cycle.

During catalysis, CO and the methyl group are thought to bind directly to the proximal Ni. The central domain of ACS has been implicated in CoA binding, and X-ray absorption studies indicate that the sulfur of CoA ligates Ni_p (*6*), although the structural motif responsible for binding CoA is not known. Chemical modification studies have provided evidence for involvement of specific tryptophan and arginine residues in CoA binding. The arginine-modifying chemicals phenylglyoxal, methylglyoxal, and butanedione inhibit the CO/acetyl-CoA exchange activity, which involves the exchange of unlabeled CO with the labeled carbonyl group of acetyl-CoA. This is a convenient assay because it requires both CoA and CO binding, but not binding of the methylated corrinoid iron-sulfur protein. Inhibition was seen both in the presence and absence of CO,

which suggests that modification of an Arg residue blocks the CoA binding site (*7*). N-bromosuccinimide (NBS) was used to modify tryptophan residues in CODH/ACS. CoA binding protects against this modification and against inhibition of both CO/acetyl-CoA exchange and acetyl-CoA synthesis activity by NBS (*8*). A specific residue (Trp418 in *M. thermoacetica* ACS) that underwent modification by a different chemical, 2,4-dinitrophenylsulfenyl-Cl, was identified by purification and sequencing of a peptide protected from modification by CoA (*9*). Trp418 faces into a cleft in the center of the protein. Its sidechain is 24 Å from Ni_p. During acetyl-CoA synthesis, the acetyl group undergoes nucleophilic attack by the sulfhydryl of CoA, so the ATP moiety of CoA may bind to the central domain of ACS, with the pantetheine part of the molecule stretching across the cleft in ACS to position sulfur near the active site.

During refinement of the structure of the *M. thermoacetica* bifunctional CODH/ACS, Yan Kung discovered a previously unknown metal binding site in the ACS subunits of the $\alpha_2\beta_2$ (Figure 4.2). The site had been modeled as a water molecule in previous structures, but the coordination of the atom in this site was octahedral, with four backbone carbonyls, one water, and one glutamate side chain as ligands. This number of coordinating ligands is inconsistent with that expected for water. Modeling Na^+ into the site gave the most reasonable ligand distances, electron density and *B*-factors. Sodium was present in high concentrations during the ion exchange chromatographic steps in the purification of CODH/ACS and at 2 mM concentration throughout the purification, but was excluded from the crystallization buffer. The metal site was found in all four ACS molecules in the asymmetric unit. Although water was originally modeled in this site in all other *M. thermoacetica* CODH/ACS structures, inspection of these structures showed

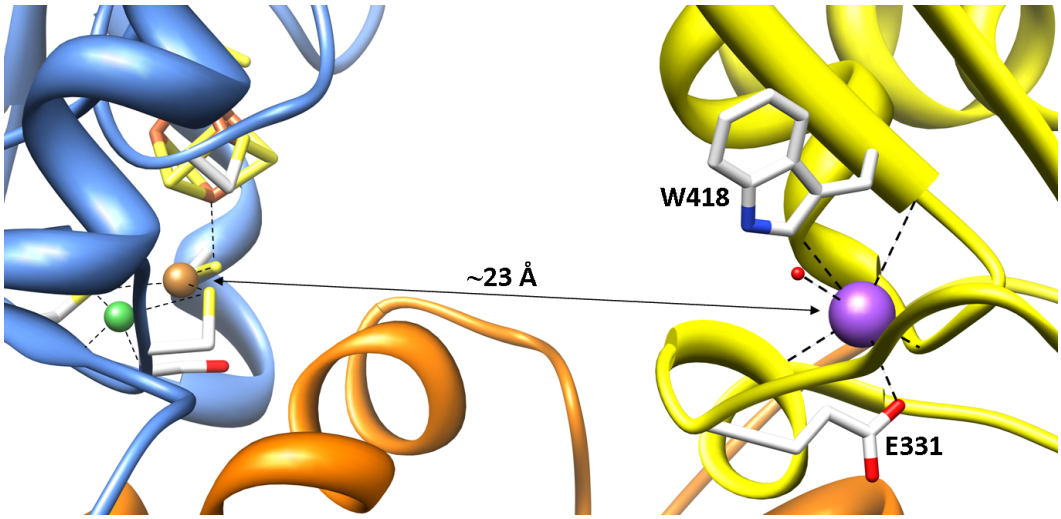

Figure 4.2. The Na^+ site in ACS. The ACS active site is on the left, with the iron-sulfur cluster shown as brown and yellow sticks, the proximal metal shown as a brown sphere (this atom was Cu in the enzyme used for crystallization, but has been shown to be Ni in the active enzyme), and the distal Ni as a green sphere. Sodium is shown as a purple sphere, the small red sphere is the coordinating water molecule. The coordination of sodium at the top is not to Trp418, but to the backbone carbonyl of Asn412 on the helix shown behind Trp418. Ribbon colors are the same as in Figure 4.1.

the octahedral coordination site in all previously published structures, in both closed and open forms of ACS. In the *C. hydrogenoformans* ACS crystal structure, the backbone carbonyls are arranged to give the same site, with only a slight rotation of the carboxylate of Glu334 (Glu331 in *M. thermoacetica* ACS).

The Na^+ site is in the middle domain of ACS, close to Trp418. The ligands to Na^+ are from backbone carbonyls of Phe328, Asn412, Gly414, and Leu417, the sidechain of Glu331, and a water molecule. Alignment of ACS sequences from several organisms (Figure 4.3) shows that Glu331 and Asn412 are most strongly conserved. The position of Phe328 has a conserved aromatic residue (F, Y or H), Gly414 is replaced by alanine, valine, isoleucine, cysteine and threonine in other ACS sequences, and the position of Leu417 has a conserved hydrophobic residue. Trp418 is replaced by methionine in several of the other aligned sequences.

```
637120264      IADKSVLPILP-GVDTVDSVLAGIPYDRIVSKAMDVRGIKVNITKVPVPVAYGPAYEGER 337
639703331      IADTDIPEILPTGVCTYEHVVSSVPYDKMTARSIEVRGLKLTVAEIPVPVAYGPAFEGER 290
640782894      ITD----QIVT---EVPTLLLTQKDFDKIPATSLEARNIKIKVTEIDIPVGFAAAFEGER 309
648091487      LTD----QVVP---EVPTLLLTQKDYDKMVKTSLEARNIKIKITEIPIPVSFAAAFEGER 309
637753967      ITD----QPLPEDKQIKDWFISEPDYDKIVQTALEVRGIKITSIDIDLPINFGPAFEGES 335
M.t. ACS       ITD----QPLPEDKQIPDWFFSVEDYDKIVQIAMETRGIKLTKIKLDLPINFGPAFEGES 332
643562715      LTD----QELGEDMQIPDWYLSEPDYEKIVPLALEVRGIKLTNIEIPIPVNFGPAFEGET 329
638175769      ----------------------------------------MVEFPFEISPMFEGER 16
638178731      ----------------------------------------MAEFPFEISPMFEGER 16
638156889      VER--------KRIEIPEGVKVKESVG---------------EEAEFPFDISPMYEGER 37
638201439      ITN--------NEVPVIKGALESSDIDNIVENALKMKGVKVKVVEFDIPVSVGPMNEGER 310
                                                                  *  *

637120264      GHKMNEDYEPILERQIHHLLNYAQGVMHIGQRDIAWLRVSKGAAAK-GFSLKHIGSILHA 455
639703331      GRKMQEDYEPILERQIHHLVNYAQGLMHIGQRDIAWYRISKQAVDK-GFTLEHIGKILHA 408
640782894      GKNMQLDFEPVLERRIHYFMNYTEGVMHVGQRDTTWIRISKDTYAS-GFRLEHIGEVLYA 428
648091487      GTNMQKDFEPVLERRLHYFLNYIEGVMHVGQRNLTWVRIGKEAFEK-GFRLKHFGEVIYA 428
637753967      GRKMQEDFEPVLERRIHYFTNYGEGFWHTAQRDLTWVRISKEAFAK-GARLKHLGQLLYA 453
M.t. ACS       GRKMQADFEGVLERRIHDFINYGEGLWHTGQRNINWLRVSKDAVAK-GFRFKNYGEILVA 450
643562715      GRKMQEDFEGVLERRIHYFTNYGEGVWHVAQRDLCWVRISKDARAK-GFLMKHIGELLLA 447
638175769      GELVEPDLESVVERRVHDFINYCQGIMHLNQRYDVWMRVSKDTAAK-MDSFEPFGQAVMM 134
638178731      GELVEPDLESVVERRVHDFINYCQGIMHLNQRYDVWMRVSKDTAAK-MDSFEPFGQAVMM 134
638156889      GEMVETDLEPVIERRNHDFQNYIEGYMHLNQRYDIWIRIGKNAIKKGLKSLIQIAKATMM 156
638201439      GSNLEEDLEGVLERRIHEFLNYIEGVMHLNQRDQVWIRINKNSFNK-GLRLKHIGEVVKQ 425
                              * *  **
```

Figure 4.3. Alignment of ACS sequences. The glutamate in the Na^+ binding site is highlighted in grey, other residues discussed in the text are marked with asterisks. Integrated Microbial Genomics identification numbers and species are 637120264: *Dehalococcoides ethenogenes* 195; 637753967: *C. hydrogenoformans* Z-2901; 637829135: *M. thermoacetica* ATCC 39073; 638156889: *Archaeoglobus fulgidus* DSM 4304; 638175769: *Methanosarcina acetivorans* str. C2A; 638178731: *Methanosarcina acetivorans* str. C2A; 638201439: *Methanocaldococcus jannaschii* DSM 2661; 639703331: *Syntrophobacter fumaroxidans* MPOB; 640782894: *Alkaliphilus metalliredigens* QYMF; 643562715: *Desulfitobacterium hafniense* DCB-2; 648091487: *Clostridium ljungdahlii* DSM 13528.

4.2 Experimental procedures

4.2.1 *Mutagenesis*

Mutations were made in the *acsB* gene from *M. thermoacetica* that was previously cloned into the pET29a vector (*10*). Glu331 was mutated to alanine, glutamine, and aspartate by the method given in the Stratagene QuikChange Site directed mutagenesis kit. The primers used for mutagenesis were 5'-CTGCCTTTGAGGGCGAT AGTATCCGTAAG-3' and 5'-CTTACGGATACTATCGCCCTCAAAGGCAG-3' for the E331D mutation, and 5'-CTGCCTTTGAGGGCGCGAGTATCCGTAAG-3' and 5'-

CTTACGGATACTCGCGCCCTCAAAGGCAG-3' for the E331A mutation. Mutations were confirmed by DNA sequencing at the University of Michigan DNA Core Facility.

4.2.2 *Protein expression and purification*

Wild-type and mutant ACS were expressed in BL21star *E. coli* cells from plasmid pET29a, as described (*10*). The cells were co-transformed with plasmid pDB1282 (kindly provided by Drs. Dennis Dean and Patricia DosSantos, Virginia Tech, Blacksburg, VA), which contains the genes *iscS-iscU-iscA-hscB-hscA-fdx* from the *isc* operon of *Azotobacter vinelandii.* Expression of these genes is controlled by an arabinose promoter. Cells were grown in terrific broth with 0.1 mg/mL ampicillin and 0.05 mg/mL kanamycin. Cultures were first grown aerobically, in stoppered 2 L bottles or a 10 L fermentor sparged with air, to an OD_{600} of around 0.5; then 0.5 g/L arabinose was added to induce expression of the *isc* genes. At OD_{600} = 0.7, the cultures were made anaerobic by bubbling with N_2 gas for 30 minutes, then by addition of an anaerobic solution of 1.5 mM sodium sulfide and 2 mM cysteine HCl (final concentrations). The medium was then supplemented with 0.1 mM ferrous ammonium sulfate and 0.2 mM $NiCl_2$, and ACS expression was induced by addition of 0.1 mM IPTG. Cells were harvested under N_2 four hours after induction and stored at -80 ^oC until use.

Frozen cells were suspended in a three-fold excess (weight/vol) of buffer containing 50 mM KPi, 10 mM imidazole, 10 mM beta-mercaptoethanol, 0.3 M NaCl, with 0.25 mg/mL lysozyme, 3 U/mL DNAse I and 0.2 mM PMSF. The cell suspension was sonicated for 10 minutes and centrifuged at 4 ^oC at 30,000 rpm for 45 minutes. The supernatant containing soluble protein was loaded on a Ni-NTA column from Qiagen

(Valencia, CA), and ACS was eluted by stepwise increases in the imidazole concentration. Purified ACS was buffer-exchanged into 50 mM tris-HCl, pH 7.6, by several cycles of concentrating the enzyme in 30 kDa molecular weight cutoff centrifuge concentrators from Millipore (Billerica, MA) and diluting in fresh buffer. ACS was reconstituted by incubation at 25 ^{o}C in 2 mM $NiCl_2$ for at least three days. Excess Ni was removed by buffer exchange as before.

4.2.3 *CO/acetyl-CoA exchange assays*

CO/acetyl-CoA exchange activity of ACS was measured at 55 ^{o}C in 0.5 mL solution in 1.5 mL v-shaped glass vials. 0.3 M MES-tetramethylammonium hydroxide, pH 5.8, and 2 mM CH_3-^{12}CO-ScoA were mixed in the vials. The vials were then removed from the anaerobic chamber, sparged with CO for 5 minutes, moved back into the anaerobic chamber, and then 2 mM freshly prepared Ti^{3+} citrate and 2 μL of CH_3-^{14}CO-SCoA (8 μM) was added via Hamilton gas-tight syringes. A 40 μL aliquot was removed to check the initial radioactivity, and 20-50 μg ACS was added via Hamilton syringe to start each assay. 0.1 mM methyl viologen was added to some assays shown in Table 4.3 for mutant and wild-type ACS, but was omitted from assays shown in Figure 4.7, since its omission seemed to give less variation in the assay results. Additional 40 μL aliquots were removed at several time points and immediately quenched in 0.1 M HCl. Samples were analyzed by liquid scintillation counting after adding scintillation cocktail.

For assays of wild-type ACS with controlled Na^+ and K^+ concentrations, the actual concentrations of these ions in each assay were measured by ICP-MS. The total volume of each assay was increased to 0.7 mL. After addition of Ti^{3+} citrate, but before

addition of radioactive acetyl-CoA, a 0.2 mL aliquot was removed from each vial for ICP-MS. A volume of ACS stock solution equal to that added to each assay was added to each metal analysis sample. Na^+ concentrations shown in Figure 4.7 are corrected for 40 μM sodium acetate buffer that was added with the radioactive acetyl-CoA stock solution.

4.2.4 *Electron paramagnetic resonance (EPR) spectroscopy*

EPR samples were prepared by reducing ACS with 5 equivalents of $Na_2S_2O_4$ from a 0.2 M stock solution in 0.1 M NaOH, sparging the headspace in each stoppered EPR tube with CO for 5 minutes, mixing each sample, and freezing samples in liquid N_2. EPR spectra were measured at 70 K from 2300-4300 G, under the following conditions: power: 0.237 or 0.948 mW, receiver gain: 2 x 10^4, modulation frequency: 100 kHz, modulation amplitude: 10 G. Concentrations of spectral features were determined by comparison to a 1 mM copper perchlorate standard.

4.2.5 *Miscellaneous methods*

Metal concentrations were determined by ICP-OES or ICP-MS at the Chemical Analysis Laboratory (University of Georgia), and by ICP-MS by Dr. Ted Huston in the University of Michigan Geological Sciences Department, after subtracting concentrations of each metal in a corresponding buffer sample.

Circular dichroism was performed in 5 mM Tris-sulfate, pH 7.6, with 0.12 mg/mL E331A ACS (1.5 μM) and 0.36 mg/mL wild-type ACS (4.4 μM). Spectra were measured in a 0.1 cm path-length cuvette. Instrumental parameters were: bandwidth of 5.0 nm, instrument response time of 4 s, scan rate of 50 nm min^{-1}, at 30 ^oC. Melting was

measured by increasing the temperature from 30 ^{o}C to 95 ^{o}C at a rate of 1 ^{o}C min^{-1}, and monitoring ellipticity at 220 nm (θ_{220}). For melting experiments, the bandwidth was decreased to 1.0 nm and the response time to 2 s. Wild-type ACS precipitated by the end of each experiment, while the E331A ACS samples remained clear.

All containers used for experiments with controlled Na^+ and K^+ concentrations, including containers for preparation of reagents and storage of stock solutions were cleaned by soaking in 4 M HCl made from trace metal grade concentrated HCl and distilled, deionized water (Milli Q system, Millipore, Billerica, MA), followed by extensive rinsing in fresh distilled, deionized water. Buffers were prepared and ACS was dialyzed and stored in plastic containers. Anaerobic water with low sodium and potassium concentrations was prepared in plastic containers by sparging water with N_2 gas, through acid-washed tygon tubing, before moving it into the anaerobic chamber.

4.3 Results

Mutations of ACS were made to explore the function of the Na^+ site. Since only one side chain is involved in the site, Glu331 was mutated to aspartate and alanine. Over-expression of ACS in *E. coli* allowed purification of ACS alone (without CODH). E331A and E331D mutants of ACS were expressed at levels similar to wild-type ACS, and were stable upon purification. E331D ACS was found to have similar CO/acetyl-CoA exchange activity, iron and nickel contents and NiFeC EPR spectra to wild-type ACS, so some of the experiments described below were focused on comparing E331A and wild-type ACS.

4.3.1 *Metal analysis results*

E331A and E331A ACS had approximately the same iron and nickel content as wild-type ACS (Table 4.1). Attempts were made to remove excess sodium and potassium from ACS. It was found that high concentrations of these metals, up to 0.7 mM sodium and 0.1 mM potassium, were present in water boiled in glass flasks and cooled under N_2, which is the usual method used in our laboratory to prepare anaerobic water, and in distilled, deionized water sent for metal analysis in glass serum bottles. The lowest Na^+ and K^+ concentrations were found in distilled, deionized water (MilliQ, Millipore) dispensed directly into plastic containers that had previously been soaked in 4M HCl (trace metal grade, Fisher Scientific) rinsed with copious amounts of distilled, deionized water, and stored in sealed plastic bags to keep out dust. Tris-HCl and MES-TMAOH buffers made from water treated in this way were analyzed by ICP-MS, and were found to have between 3 and 25 μM K^+ and between 6 and 27 μM Na^+.

4.3.2 *Spectral characterization of wild-type and E331A ACS*

Fully active ACS should have four irons and two nickel atoms per monomer, but ACS as purified contains significant amounts of Cu and Zn in the central Ni site, which are not active metals in ACS (*11-13*). When ACS is first reduced, then incubated with CO, a characteristic EPR spectrum, called the NiFeC spectrum develops. There is strong evidence that this is the spectrum of an intermediate state in the catalytic cycle (*1*), and it can be used as a measure of how much active enzyme, containing both Ni atoms, is present. Quantification of the NiFeC signals from three preparations of wild-type and E331A ACS and two preparations of E331D ACS is shown in Table 4.2. Two

preparations of E331A ACS had considerably lower intensities of the NiFeC spectrum. These enzymes were not deficient in iron and nickel. As shown in Table 4.1, both preparations 1 and 2 of E331A ACS contained levels of Ni and Fe comparable to wild-type ACS. The third E331A ACS preparation had NiFeC signal intensity similar to that observed with wild-type ACS.

Table 4.1. Metal analysis of ACS preparations. Results in moles/mol ACS

	Wild-type	E331A	E331D	Enzyme preparation
Fe[a]	2.37	2.90	3.26	1
Ni[a]	1.36	2.16	2.56	1
Cu[a]	0[d]	0.01	0	1
Zn[a]	1.18	0.74	0.70	1
Fe[a]	3.24	3.02	3.50	2
Ni[a]	2.64	2.94	2.91	2
Cu[a]	0.02	0.01	0	2
Zn[a]	1.30	0.98	1.35	2
Fe[b]	2.37, 3.20	2.57, 4.20	N.D.[c]	3
Ni[b]	1.80, 1.60	1.56, 1.74	N.D.	3
Cu[b]	0.005, 0.005	0.005, 0.005	N.D.	3
Zn[b]	0.43, 0.38	0.37, 0.31	N.D.	3
K[b]	0, 0[d]	0, 0	N.D.	3
Na[b]	0, 0	0.24, 0	N.D.	3
Average Fe	2.8 $\pm$ 0.5	3.2 $\pm$ 0.7	3.4 $\pm$ 0.2	
Average Ni	1.9 $\pm$ 0.6	2.1 $\pm$ 0.6	2.7 $\pm$ 0.3	
Average Cu	0.01 $\pm$ 0.01	0.01 $\pm$ 0.003	None detected	
Average Zn	0.8 $\pm$ 0.5	0.6 $\pm$ 0.3	1.0 $\pm$ 0.5	

[a] Determined by ICP-OES after buffer exchange into 50 mM tris-HCl, the two values shown are from two purifications of each enzyme.
[b] Determined by ICP-MS after dialysis against 100 mM Tris-HCl, 2 mM DTT with low Na^+, K^+. The two values shown are for enzyme pre-incubated in buffer containing 0.3 M K^+ or Na^+ buffer before dialysis.
[c] Not determined.
[d] The concentration of each element in a dialysis buffer blank was subtracted from the concentration in each protein sample. Zero indicates that the protein sample had less of the ion than the buffer had. Actual Na^+ concentrations were between 6 and 27 μM, and K^+ concentrations were between 3 and 25 μM. The copper concentration in buffers was around 1 μM.

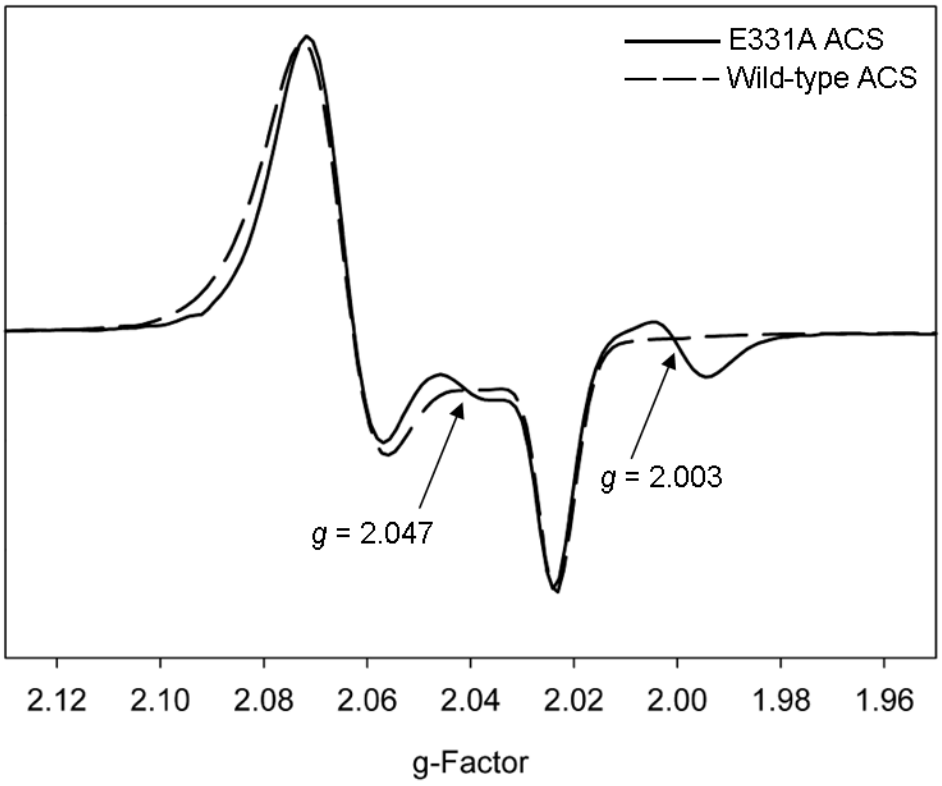

Figure 4.4. NiFeC EPR spectra of 161 μM wild-type (dashed line) and 151 μM E331A (solid line) ACS (both from preparation 1) were measured as described in the text. The intensity of the E331A spectrum has been multiplied by four for easier comparison with the wild-type spectrum.

Table 4.2 Quantification of NiFeC EPR signals, results in spins/ACS

Enzyme preparation	Wild-type	E331A	E331D
a	0.22	0.05	0.11
b	0.15	0.01	0.37
c	0.74	0.34	N.D.[a]

[a] Not determined.

In preparation 1, the E331A spectrum had features in addition to the NiFeC signal, at $g = 2.047$ and $g = 2.003$ (Figure 4.4). Spectra similar to the spectrum seen with E331A ACS preparation 1 were seen with wild-type and E331D enzymes from preparation 2. In preparation 2 of the E331A mutant, very low EPR signal intensity was seen after reduction of the enzyme and treatment with CO. This was probably not the

result of a difference in the amount of E331A ACS in the sample or the presence of a contaminant that was absent in other ACS samples, because the level of expression and purity of ACS were similar in all preparations of all of the ACS variants. In the small amount of EPR active protein, the intensity of the spectral features at $g = 2.00$ and $g = 2.04$ was greater than the intensity of the NiFeC spectrum (the concentration given in Table 4.2 represents both sets of spectral features). It is not known what state of the enzyme gives rise to the additional features in the EPR spectra of E331A preparation 1 and in preparation 2 of all three enzymes.

To test whether the additional EPR signals were the result of stabilization of a different conformation of ACS, circular dichroism spectra (Figure 4.5) and melting temperatures (Figure 4.6) of wild-type and E331A ACS from preparation 1 were measured. The melting curves shown are irreversible for wild-type ACS, which precipitated by the end of each experiment. The concentrations of Na^+ and K^+ in these samples were around 750 μM (Na^+) and 100 μM (K^+). This was approximately 500-fold or 170-fold excess of Na^+ over E331A or wild-type ACS, respectively, and around 70-fold or 20-fold excess of K^+ over E331A or wild-type ACS, respectively. Wild-type ACS samples with 5 mM and 50 mM K^+ were prepared to see if addition of a metal cation would affect the circular dichroism spectrum or stability of the enzymes. The circular dichroism spectra of wild-type and E331A ACS preparation 1 were similar, although there were subtle differences between the wild-type and E331A ACS spectra below 200 nm. Addition of 50 mM K^+ to wild-type ACS had little effect on the circular dichroism spectrum. The melting temperatures of wild-type and E331A ACS were also similar. The irreversible melting of the wild-type, particularly with added K^+, is monitored by the

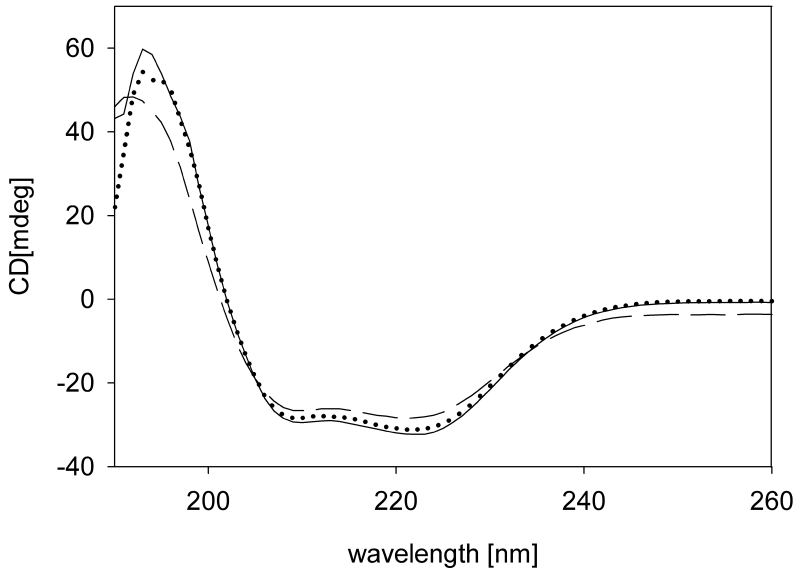

Figure 4.5. Circular dichroism spectra of wild-type and E331A ACS. Solid line: wild-type ACS, dashed line: wild-type ACS with 50 mM K^+, dotted line: E331A ACS. The E331A ACS spectrum has been multiplied by three for easier comparison with the wild-type spectra. Wild-type ACS was 4.4 µM and E331A ACS was 1.5 µM in these experiments.

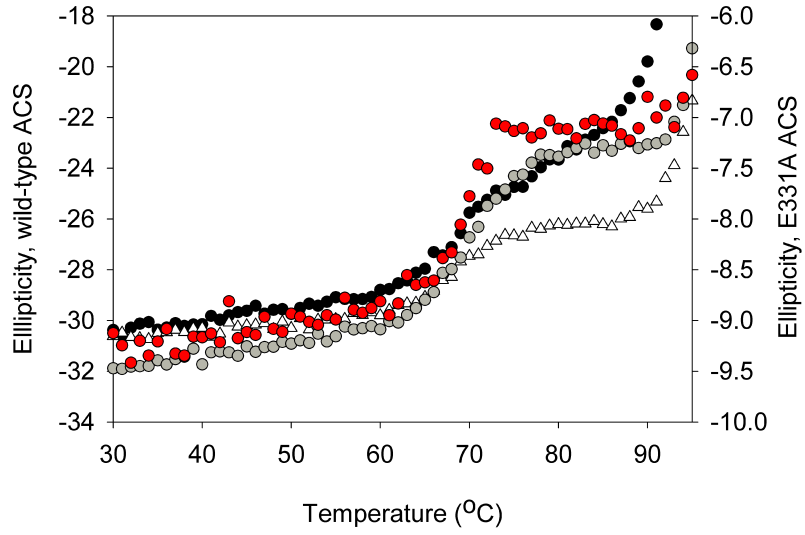

Figure 4.6. ACS melting measured by circular dichroism spectroscopy. Grey circles: wild-type ACS, triangles: wild-type ACS with 5 mM K^+, black circles: wild-type ACS with 50 mM K^+, red circles: E331A ACS. Wild-type ACS was 4.4 µM and E331A ACS was 1.5 µM in these experiments.

sharp increase in molar ellipticity above 80 °C, which could be caused by denaturation or aggregation of the protein. The melting temperature was taken as the inflection point on each curve (the point around 70 °C with the steepest slope). E331 A had a melting temperature of 71 °C. Wild-type ACS had a melting temperature of 69 °C with 100 μM K^+, 66 °C with 5 mM K^+, and 68 °C with 50 mM K^+.

4.3.3 *Comparison of CO/acetyl-CoA exchange activities*

The exchange of ^{12}CO with ^{14}CO from the carbonyl position of acetyl-CoA was measured to see if the enzymatic activity of ACS was affected by mutating E331. The results of several assays are shown in Table 4.3. The E331A ACS variant has approximately 25-fold lower specific activity than wild-type and E331D ACS. There is some variation in the activities measured with different preparations of enzyme and at different times, which is likely to be due to differences in the redox potentials in the

Table 4.3 CO exchange activities, U/mg

Enzyme preparation	Wild-type	E331A (%)[a]	E331D (%)
1	0.82	0.031 (3.8)	0.72 (88)
1	1.5	0.022 (1.5)	0.53 (35)
2	N.D.[b]	0.042	0.13
2	2.0	0.094 (4.7)	0.37 (19)
2	0.57[c]	0.033[c] (5.8)	0.73[c] (130)
1, 2 (wt), 2 (E331A)	0.49, 0.36[c]	0.034[c] (6.9)	N.D.
3	0.19[c]	0.007[c] (3.7)	N.D.
Average activity	0.85 ± 0.61	0.037 ± 0.025	0.50 ± 0.23

Each row shows a set of assays performed in parallel.
[a] The number in parenthesis shows a comparison of the activity of each variant to the wild-type ACS activity determined in the same set of assays.
[b] Not determined.
[c] No methyl viologen was added to these assays.

assays. In later experiments, marked with (*c*) in Table 4.3, more consistent results were seen by removing methyl viologen from assays, by very careful preparation of Ti^{3+} citrate solutions just before the assays were performed, and by addition of Ti^{3+} citrate after adding CO to the assay vials, and exactly three minutes before starting each assay.

The assays reported in Table 4.3 contained approximately 1 mM Na^+ from the Ti^{3+} citrate solution and from the glassware used in reagent preparation. More CO exchange assays were done with wild-type ACS, after careful dialysis to remove as much Na^+ and K^+ as possible. Different concentrations of Na^+ were added to these assays, and aliquots were taken for metal analysis before addition of radioactive acetyl-CoA and

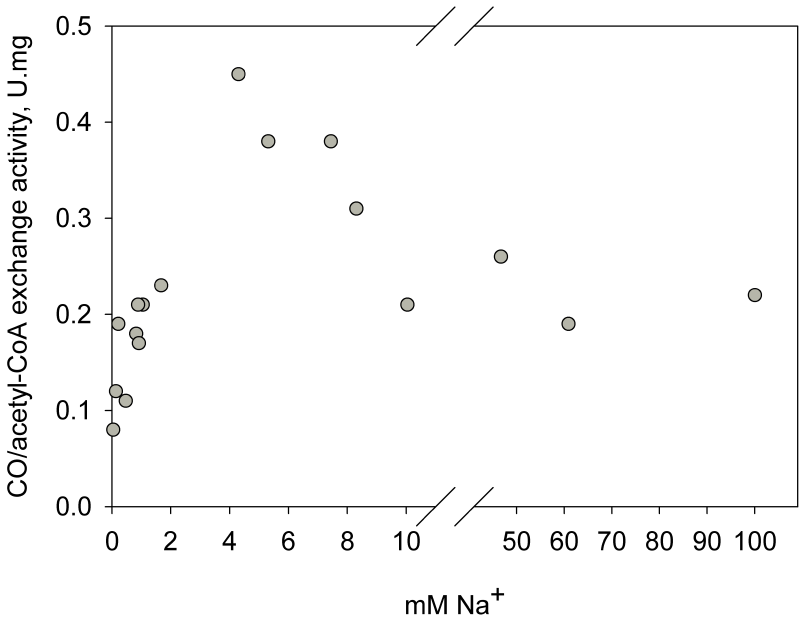

Figure 4.7. Dependence of the CO exchange activity of ACS on Na^+ concentration. Assays were performed as described in the methods section, without methyl viologen. Solutions were prepared in plastic containers, and the assays were done in acid-washed glass v-vials at 25 ^oC. Na^+ and K^+ concentrations were confirmed by removing an aliquot of each assay mix for ICP-MS, before addition of CH_3-^{14}CO-SCoA, which was prepared in sodium acetate buffer. Na^+ concentrations shown are corrected for the amount of Na^+ in the ^{14}C-acetyl-CoA solution (8 μM). K^+ was less than 30 μM in each assay.

enzyme. A small dependence of the activity on Na^+ concentration was seen (Figure 4.7). Comparing the activity at no added Na^+ to that at saturating concentrations, Na^+ appears to cause a 2.5-fold stimulation in CO/acetyl-CoA exchange activity. Additional assays with 2-50 mM Na^+ would be needed to clearly define the effect of Na^+ on the activity. However, these preliminary data show that Na^+ increases the CO/acetyl-CoA exchange activity at least four-fold below 5 mM, and inhibits it at least two-fold above this concentration.

4.4 Discussion

The sodium site in ACS may be important for activity. Mutation of E331 to aspartate had little effect on the properties of ACS. Given sufficient conformational flexibility, it is likely that the smaller acidic sidechain can substitute effectively and coordinate Na^+ in the same way as glutamate. Mutation of E331 to alanine led to a ~25-fold decrease in ACS activity. This effect was not clearly correlated with the ability ACS to bind Ni and Fe. The mutations did not alter the iron and nickel content of ACS, as expected given that the Na^+ site is about 23 Å from the A-cluster. Furthermore, the substitutions did not affect the overall secondary structure or stability of the enzyme, on the basis of the similar circular dichroism spectra and melting curves for wild-type and E331A ACS.

Despite these similarities to the wild-type enzyme, two of three preparations of the E331A variant had altered EPR spectra with additional features at $g = 2.047$ and $g = 2.003$ after reduction and CO binding, suggesting that the active site of the enzyme is perturbed in some way. However, since this altered spectrum was also seen in one

preparation each of wild-type and E331D ACS, in can not be a specific feature of the E331A mutant, and can not be attributed to disruption of the Na^+ site.

It was difficult to control Na^+ concentrations in the sub mM range, where the greatest effect on activity was observed. We attempted to completely remove Na^+ and K^+ from ACS so that the effect of addition of these ions could be precisely determined. In wild-type enzyme that was dialyzed against carefully prepared buffers containing low concentrations of Na^+ and K^+, the concentrations of these metals were similar in ACS and buffer samples. However, these concentrations, in the range of 3-30 μM, are similar to the ACS concentrations used in the metal analysis experiments, so it is hard to be sure that the metals are really removed from ACS. CO exchange assays of wild-type ACS at sodium concentrations from ~30 μM to 100 mM show a small dependence of activity on Na^+ concentration, with the largest changes below 5 mM. High concentrations of Na^+ have a moderate inhibitory effect on the activity. Further experiments are needed to show whether this effect is on the sodium site at residue E331 or is a more general effect of salt concentration on ACS activity.

The low concentration of Na^+ that affected the activity of ACS suggests that Na^+ plays a structural role and does not modulate the activity of the enzyme *in vivo*. Although internal Na^+ concentrations in *M. thermoacetica* have not been measured, in other bacteria, internal concentrations depend on external Na^+ concentrations, and vary between approximately 8 and 400 mM in *E. coli*, and between 30 and 300 mM in a halotolerant Gram-positive *Brevibacter* species (*14-16*). Based on these concentrations, Na^+ is likely to be constantly bound to ACS *in vivo*.

Future work should include further measurements of the NiFeC EPR spectrum in the variants to determine if the lower activity of E331A ACS is related to changes in the active site structure. The activity of E331A ACS should be assayed over a range of Na^+ concentrations, as was done for wild-type ACS, to see if this mutation abolishes the Na^+ dependence of the activity. Our hypothesis is that the Na^+ site is involved in binding CoA/acetyl-CoA. Thus, the E331A variant should have a markedly higher Kd for CoA. In addition, the CoA/acetyl-CoA exchange activity, which is orders of magnitude faster than the CO/acetyl-CoA exchange, is expected to be markedly altered by replacement of E331. The activity of E331A ACS was consistently lower than that of E331D or wild-type ACS. Whether this is because of some effect of the mutation on the active site is not clear.

4.5 References

(1) Doukov, T. I., Iverson, T. M., Seravalli, J., Ragsdale, S. W., and Drennan, C. L. (2002) A Ni-Fe-Cu Center in a Bifunctional Carbon Monoxide Dehydrogenase/ Acetyl-CoA Synthase. *Science 298*, 567-572.

(2) Darnault, C., Volbeda, A., Kim, E. J., Legrand, P., Vernede, X., Lindahl, P. A., and Fontecilla-Camps, J. C. (2003) Ni-Zn-[Fe_4-S_4] and Ni-Ni-[Fe_4-S_4] clusters in closed and open [alpha] subunits of acetyl-CoA synthase/carbon monoxide dehydrogenase. *Nat. Struct. Mol. Biol. 10*, 271-279.

(3) Dobbek, H., Svetlitchnyi, V., Gremer, L., Huber, R., and Meyer, O. (2001) Crystal structure of a carbon monoxide dehydrogenase reveals a [Ni-4Fe-5S] cluster. *Science 293*, 1281-5.

(4) Seravalli, J., and Ragsdale, S. W. (2000) Channeling of Carbon Monoxide during Anaerobic Carbon Dioxide Fixation. *Biochemistry 39*, 1274-1277.

(5) Doukov, T. I., Blasiak, L. C., Seravalli, J., Ragsdale, S. W., and Drennan, C. L. (2008) Xenon in and at the end of the tunnel of bifunctional carbon monoxide dehydrogenase/acetyl-CoA synthase. *Biochemistry 47*, 3474-3483.

(6) Seravalli, J., Gu, W., Tam, A., Strauss, E., Begley, T. P., Cramer, S. P., and Ragsdale, S. W. (2003) Functional copper at the acetyl-CoA synthase active site. *Proc. Natl. Acad. Sci. U S A 100*, 3689-94.

(7) Ragsdale, S. W., and Wood, H. G. (1985) Acetate biosynthesis by acetogenic bacteria. Evidence that carbon monoxide dehydrogenase is the condensing enzyme that catalyzes the final steps of the synthesis. *J. Biol. Chem. 260*, 3970-3977.

(8) Shanmugasundaram, T., Kumar, G. K., and Wood, H. G. (1988) Involvement of tryptophan residues at the coenzyme A binding site of carbon monoxide dehydrogenase from *Clostridium thermoaceticum*. *Biochemistry 27*, 6499-6503.

(9) Morton, T. A., Runquist, J. A., Ragsdale, S. W., Shanmugasundaram, T., Wood, H. G., and Ljungdahl, L. G. (1991) The primary structure of the subunits of carbon monoxide dehydrogenase/acetyl-CoA synthase from *Clostridium thermoaceticum*. *J. Biol. Chem. 266*, 23824-23828.

(10) Seravalli, J., and Ragsdale, S. W. (2008) Pulse-Chase Studies of the Synthesis of Acetyl-CoA by Carbon Monoxide Dehydrogenase/Acetyl-CoA Synthase. *J. Biol. Chem. 283*, 8384-8394.

(11) Gencic, S., and Grahame, D. A. (2003) Nickel in Subunit B of the Acetyl-CoA Decarbonylase/Synthase Multienzyme Complex in Methanogens. *J. Biol. Chem. 278*, 6101-6110.

(12) Bramlett, M. R., Tan, X., and Lindahl, P. A. (2003) Inactivation of Acetyl-CoA Synthase/Carbon Monoxide Dehydrogenase by Copper. *J. Am. Chem. Soc. 125*, 9316-9317.

(13) Seravalli, J., Xiao, Y., Gu, W., Cramer, S. P., Antholine, W. E., Krymov, V., Gerfen, G. J., and Ragsdale, S. W. (2004) Evidence that NiNi Acetyl-CoA Synthase is Active and that the CuNi Enzyme is Not. *Biochemistry 43*, 3944-3955.

(14) Epstein, W., and Schultz, S. G. (1965) Cation Transport in *Escherichia coli*: V. Regulation of cation content. *J. Gen. Physiol. 49*, 221-34.

(15) Gilboa, H., Kogut, M., Chalamish, S., Regev, R., Avi-Dor, Y., and Russell, N. J. (1991) Use of ^{23}Na nuclear magnetic resonance spectroscopy to determine the true intracellular concentration of free sodium in a halophilic eubacterium. *J. Bacteriol. 173*, 7021-3.

(16) Nagata, S., Adachi, K., Shirai, K., and Sano, H. (1995) 23Na NMR spectroscopy of free Na^+ in the halotolerant bacterium *Brevibacterium* sp. and *Escherichia coli*. *Microbiology 141 (Pt 3)*, 729-36.

CHAPTER V

Interconversions of carbon monoxide and carbon dioxide by carbon monoxide dehydrogenase on conducting graphite platelets and titanium oxide nanoparticles[8]

5.1. Introduction

Carbon dioxide is attractive as a feedstock for clean and efficient systems to produce industrially useful chemicals because it is non-toxic and abundant. Because it is a greenhouse gas that contributes to global warming and is produced in high amounts as the end product of the oxidation of carbon-based fuels, it is becoming increasingly important to find processes that use CO_2 (*1*). Strategies for converting CO_2 to useful products include chemical reactions that produce organic compounds, heterogeneous catalysts and electrochemical catalytic reductions, production of synthesis gas (i. e., syngas, a mixture of CO and H_2). These strategies can be accomplished by cell- and enzyme-based reactions.

Catalytic systems that include enzymes have several advantages. Enzymes usually catalyze specific reactions with high efficiency, including very low levels of unwanted side products. They work efficiently at low temperatures and pressures (relative to most

[8] The work described in this chapter is from collaboration between Dr. Stephen Ragsdale's lab and Dr. Frasier Armstrong's lab. Dr. Ragsdale's lab takes a strong interest in the study of the mechanism of CODH, while Dr. Armstrong's lab focuses on development of stable catalysts in which enzymes are mixed with other materials. The CODH enzyme used in this work was provided by our lab, while the development of the electrochemical systems took place in Dr. Armstrong's lab.

inorganic catalysts) and in aqueous solutions. A specific advantage that enzymes have in the reduction of CO_2 is that they use reduction mechanisms that avoid the extremely unfavourable one-electron reduction of CO_2 to an anion radical, which has a reduction potential of -1.9 V vs. standard hydrogen electrode. Thus, the enzyme reaction can be performed at the potential of the CO_2/CO couple (-0.53 V vs. SHE). Similarly, formate dehydrogenase reduces CO_2 to formate at a midpoint potential of -0.61 V vs. SHE (*2*).

CO and formate dehydrogenases catalyze the direct reduction of CO_2. Both are found in the Wood-Ljungdahl pathway, where they catalyze the first steps in the carbonyl and methyl branches of the pathway. Both enzymes are also widely distributed in organisms that do not use the Wood-Ljungdahl pathway, and are involved in bacterial energy metabolism. For example, in *E. coli*, formate dehydrogenase couples formate oxidation to H_2 reduction in the formate hydrogen lyase coupled to nitrate reduction during nitrate respiration (*3*). Different, evolutionarily unrelated forms of CO dehydrogenase allow anaerobic and aerobic bacteria to couple CO oxidation to H_2 or O_2 reduction (*4-7*). CODH also performs other functions, which are best exemplified in *Carboxydothermus hydrogenoformans*, a CO-oxidizing, H_2 evolving bacterium that encodes five CODHs in its genome (*8*). CODH I is expressed with hydrogenase in the complex used for CO-dependent energy conservation (*4*). CODH II reduces electron carriers such as $NADP^+$ (*9*). CODH III is part of the Wood-Ljungdahl pathway (*9*). CODH IV and V have not been purified, but based on adjacent genes, CODH IV is proposed to be involved in the oxidative stress response, while the function of CODH V is unknown (*8*).

Anaerobic CODHs contain iron and nickel. The active sites of CODH I, II, and III isolated from different organisms all consist of cluster C, which is an Fe_3S_4 sub-site ligated by cysteines and bridged to a NiFe sub-site. Ni ligation is planar. It roughly occupies one corner of the cubane made by the Fe_3S_4 sub-site, and is additionally ligated by cysteine. The iron of the NiFe sub-site, usually referred to as ferrous component II (FCII), is ligated by cysteine and histidine (*9-13*). As shown in Figure 5.1, CO and H_2O binding are required for CO oxidation (Step 1). X-ray crystal structures have been reported of CODH with CO_2 (*14*), or with water and CN^-, which is a competitive inhibitor with respect to CO, bound to the active site (*15*). In these two separate structures, CO_2 and CN^- were bound to Ni, and water or hydroxide to FCII. Evidence for CO binding to Ni is provided by an X-ray crystal structure of CO-bound CODH from a methanogen, (*11*) and by studies of binding of the competitive inhibitor CN^- by Fourier transform infrared (FTIR) (*16*) and X-ray absorption spectroscopies (*17*). Water is proposed to bind to FCII, based on the crystal structure of CODH with water and CN^- bound at the active site (*15*), and to be deprotonated with the assistance of Lys and His residues near the C-cluster (step 2) (*9, 10*). This would set up the active site for Fe-hydroxide attack on Ni–CO to form a carboxylate that bridges the Ni and Fe atoms (step 3), as seen in the crystal structure with CO_2 bound (*14*). Then, step 4 is release of CO_2, coupled to two electron reduction of the active site metal cluster before electrons are transferred from the active site through two more Fe_4S_4 clusters to the surface of the protein, where they can be passed to an external electron acceptor like ferredoxin (step 5) (*18*).

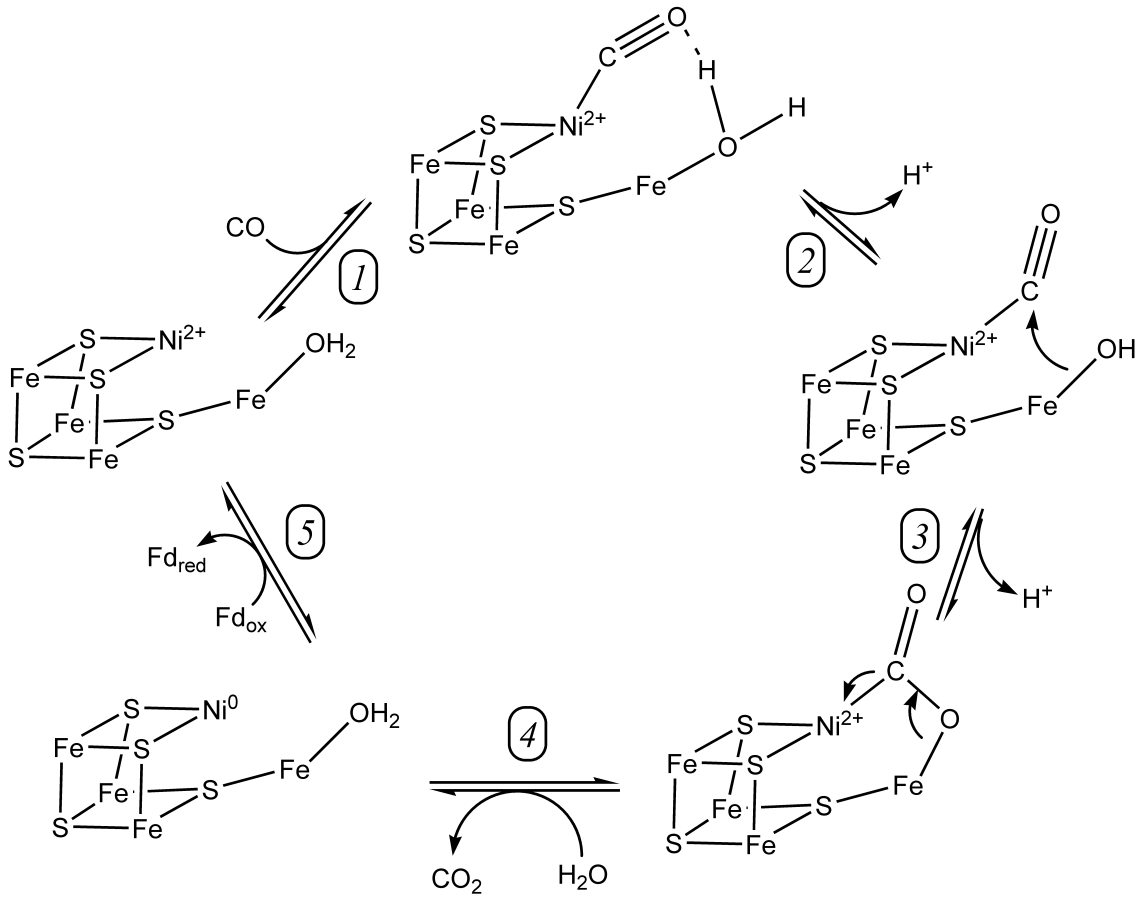

Figure 5.1. Mechanism of CODH. This figure is based on (*19*).

CO_2 is the most oxidized carbon compound. It is very stable, and most reactions to convert CO_2 into other usable compounds are kinetically and thermodynamically unfavorable. Development of efficient, environmentally friendly catalysts is an even greater challenge, since it means that a clean, cheap source of energy is needed. One possibility is to couple CO_2 reduction to solar energy by developing systems that catalyze photoreduction of CO_2 using sunlight. Below, two papers are summarized that describe the development of a system that catalyzes photoreduction of CO_2 to CO by CODH attached to titanium oxide nanoparticles. A third paper describes a heterogeneous catalyst made of CODH and hydrogenase electrically coupled on

pyrolytic graphite particles. This system mimics the energy conserving system used by *C. hydrogenoformans* and other CO-oxidizing, H_2-evolving bacteria.

5.2. CO_2 photoreduction on titanium oxide nanoparticles[9]

Photoreduction of CO_2 to CO by sunlight could provide a clean way to convert CO_2 into a useful feedstock for current industrial processes that produce hydrocarbons, acetic acid and methanol from CO, or for the water-gas shift reaction discussed below. CO_2 photoreduction to mixtures of formate, formaldehyde and methanol by Ti-, Zn-, Cd-, W-, Si- and Ga-oxide semiconductors using light that could be directly absorbed by each catalyst was first reported over three decades ago (*20*). High energy UV light is required for band gap excitation of these semiconductors and improvements on these catalysts came with the development of systems that could absorb visible light for CO_2 reduction by combining a dye that could be excited by visible light with a semiconductor whose conducting band could accept electrons from the excited dye (*21*). One drawback to these systems is that a mixture of products is formed.

CODH I from *C. hydrogenoformans* is a very efficient enzyme with k_{cat}/K_m = $1.3 \cdot 10^9$ M^{-1} CO s^{-1} at 70 °C, the maximal growth temperature of the organism (*9*). CODH was previously shown to be active in both directions when coupled to a pyrolytic graphite edge electrode (*22*). A photosensitive catalyst for CO_2 reduction was made by adsorbing CODH I and a ruthenium bipyridyl dye onto TiO_2 particles. At pH 6, where the experiments were performed, the conduction band edge of TiO_2 is at about -0.52 V vs. SHE, corrected to pH 6, which is very close to the potential of the CO_2/CO couple (-0.42

[9] This work was published as Woolerton et al. (2010) Efficient and Clean Photoreduction of CO_2 to CO by Enzyme-Modified TiO_2 Nanoparticles Using Visible Light, *JACS 132*, 2132-3 and Woolerton et al. (2011) CO_2 Photoreduction at Enzyme-modified Metal Oxide Nanoparticles, *Energy Environ. Sci 4*, 2393-9.

V vs. SHE at pH 6). The nanoparticles were prepared in MES buffer, and were sealed into a glass vial that was purged with 98% CO_2/2% CH_4 (added as an internal standard). The vial was irradiated with visible light from a tungsten-halogen lamp with a filter to block light below 420 nm, and the amount of CO produced was quantified by gas chromatography. CO was the only product detected. When the nanoparticles, the ruthenium dye, CODH or light were excluded, CO was produced in negligible amounts. However, in the absence of the dye, CO was produced upon irradiation of the nanoparticles at the band gap energy of TiO_2. In the presence of the dye, the turnover rate (with reference to the amount of CODH present on the nanoparticles) was about 0.15 s^{-1}. This should be compared to CO_2 reduction in solution, performed in the same buffer but using reduced methyl viologen as the reductant (E_0' = -0.44 V), which CODH catalyzed with a turnover number of 95 s^{-1}. The TiO_2/ruthenium dye/CODH system was unstable, with CO production leveling off after about six hours. The same lower rate was seen when the nanoparticles were stored in the dark for four hours after the addition of CO_2. Activity was also not restored to initial levels if CO was flushed out of solution after four hours, and was not inhibited initially by starting the experiments with mixtures of up to 30% CO in CO_2. These controls ruled out photo-degradation and CO sensitivity of some component as causes of the loss of activity.

Further experiments to try to improve the turnover rate and stability of the system were mostly unsuccessful. Effective attachment of CODH and the ruthenium dye to the TiO_2 nanoparticles was found to be limited to about 1 nmol CODH and 40 nmol ruthenium dye per 5 mg nanoparticles. Above these limits, although more CODH and dye could be adsorbed, the CO production activity did not increase. This could be explained if

the limiting concentrations were those required to form a monolayer over the surface of the particles. This hypothesis was supported by the observation that the activity increased when more TiO_2 was added to the suspensions.

Substitution of different materials into the system also mostly gave no improvement. The TiO_2 particles used in the initial experiments were mixture of two polymorphs of TiO_2, anatase and rutile. Substitution of pure nanoparticles of either material gave lower CO production, although removing anatase had a much larger effect, probably because the rutile conduction band is around -0.32 V at pH 6, which should be too high to drive CO_2 reduction. Replacement of TiO_2 with ZnO or $SrTiO_3$ gave less efficient CO_2 reduction. Replacement of MES (the sacrificial electron donor that re-reduces the ruthenium dye) with EDTA or triethanolamine did not increase the stability of the system, although EDTA addition increased the activity by about 40 %. Substitution of CODH II from *C. hydrogenoformans* for CODH I gave similar activity. Using CODH/ACS from *M. thermoacetica* or aerobic CODH from *Oligotropha carboxidovorans* gave no CO_2 reduction activity.

5.3. CO oxidation and H_2 formation on conducting graphite platelets[10]

The water-gas shift reaction is CO oxidation coupled to H_2 formation as shown by equation 5.1. This overall reaction is used as an energy conserving process in some bacteria, and is also used industrially in petroleum refining, chemical production, and in production of H_2 for fuel cells. The non-enzymatic reaction can be carried out by d-metal catalysts, including Cu, Fe-Cr, Au and Pt, often attached to oxide particles (for example,

[10] This work was published as Lazarus et al. (2009) Water-Gas Shift Reaction Catalyzed by Redox Enzymes on Conducting Graphite Platelets, *JACS 131*, 14154-5.

Au on CeO_2) at temperatures around 200 ^oC (*23*). The enzymatic reaction is carried out by a combination of CO dehydrogenase and hydrogenase. In *C. hydrogenoformans*, these two enzymes form a membrane-bound complex that also includes an electron transfer protein (*4*). The potentials of the CO_2/CO couple and the H^+/H_2 couple differ by about 0.1 V at pH 7, such that conversion of CO to H_2 is thermodynamically favorable.

$$CO + H_2O \leftrightarrow CO_2 + H_2 \quad (5.1)$$

CODH I and [NiFe]-dependent hydrogenase 2 (Hyd-2) from *E. coli* were used in experiments to electrochemically couple CO oxidation to H_2 production. Hydrogenases are sensitive to CO but when Hyd-2 was adsorbed on a pyrolytic graphite edge electrode (without CODH) it produced H_2 in the presence of up to 15 % CO. To test their combined activity, CODH and H_2 were adsorbed onto graphite platelets, which were placed in a thermostated glass cell in an anaerobic chamber. The cell was sealed and flushed with 98% N_2/2% CH_4, aliquots of CO were added, and changes in the concentrations of CO and H_2 over time were monitored by gas chromatography (CH_4 was added as an internal standard). H_2 was produced simultaneously with CO consumption until CO was almost completely depleted. Addition of additional CO at that time allowed additional H_2 formation. In the absence of CODH, hydrogenase, CO, or the graphite platelets, less than 0.01 % H_2 was produced over 24 hours. This trace of H_2 may have come from CODH, since another CODH has been shown to have slow hydrogen-evolving activity in the absence of any other electron acceptor (*24*). That H_2 is not produced in the absence of the platelets supports the hypothesis that the platelets are necessary for electron transfer from CODH to hydrogenase. The turnover frequency was calculated from the amount of hydrogenase loaded on the platelets as at least 2.5 s^{-1} at 30 ^oC. This compared favorably

with reports of a $Ru_3(CO)_{12}$ catalyst with a turnover rate of 0.01 mol H_2 s^{-1} per mole of catalyst at 160 ^oC, and an Au-CeO_2 catalyst with a turnover rate of 3.9 s^{-1} at 240 ^oC.

5.4. Discussion

Although these experiments demonstrate catalysis of useful reactions, these techniques are not ready for large scale commercial use. Problems include the fragility of enzymes, and the difficulty of producing them in large quantities. In addition, the CO_2 photoreduction system is inactivated over time. Furthermore, the activity of CO oxidation when CODH is adsorbed on an electrode is much lower than that of CODH in solution. Possible areas for improvement are in optimization of the system used to regenerate the dye and in more efficient attachment of the enzyme to the nanoparticles. While it is hypothesized that CODH is attached in a monolayer on the nanoparticle surface, it is not clear whether the enzyme molecules are preferentially oriented in one position and whether the most common orientations for attachment are those that would place the iron-sulfur cluster that is closest to the surface of the enzyme in close contact with the TiO_2 surface. Specific mutations to introduce an anchoring site on the enzyme may increase CODH binding in a productive orientation. However, such experiments will have to await the development of a good system for heterologous expression of CODH, which is made difficult by the complexity of the active site metal cluster and insufficient knowledge of the metallochaperones required to assemble the C cluster.

5.5 References

(1) Song, C. (2006) Global challenges and strategies for control, conversion and utilization of CO_2 for sustainable development involving energy, catalysis, adsorption and chemical processing. *Catal. Today 115*, 2-32.

(2) Benson, E. E., Kubiak, C. P., Sathrum, A. J., and Smieja, J. M. (2009) Electrocatalytic and homogeneous approaches to conversion of CO_2 to liquid fuels. *Chem. Soc. Rev. 38*, 89-99.

(3) Stewart, V. (1988) Nitrate respiration in relation to facultative metabolism in enterobacteria. *Microbiol. Rev. 52*, 190-232.

(4) Soboh, B., Linder, D., and Hedderich, R. (2002) Purification and catalytic properties of a CO-oxidizing:H_2-evolving enzyme complex from *Carboxydothermus hydrogenoformans*. *Eur. J. Biochem. 269*, 5712-21.

(5) Kistner, A. (1954) Conditions Determining the Oxidation of Carbon Monoxide and of Hydrogen by *Hydrogenomonas carboxydovorans*. *Proc. K. Ned. Akad. Wet., Series C 57*, 186-195.

(6) Singer, S. W., Hirst, M. B., and Ludden, P. W. (2006) CO-dependent H_2 evolution by *Rhodospirillum rubrum*: Role of CODH:CooF complex. *Biochim. Biophys. Acta, Bioenerg. 1757*, 1582-1591.

(7) Meyer, O., Jacobitz, S., and Krüger, B. (1986) Biochemistry and physiology of aerobic carbon monoxide-utilizing bacteria. *FEMS Micro. Lett. 39*, 161-179.

(8) Wu, M., Ren, Q., Durkin, A. S., Daugherty, S. C., Brinkac, L. M., Dodson, R. J., Madupu, R., Sullivan, S. A., Kolonay, J. F., Haft, D. H., Nelson, W. C., Tallon, L. J., Jones, K. M., Ulrich, L. E., Gonzalez, J. M., Zhulin, I. B., Robb, F. T., and Eisen, J. A. (2005) Life in hot carbon monoxide: the complete genome sequence of *Carboxydothermus hydrogenoformans* Z-2901. *PLoS Genet. 1*, e65.

(9) Dobbek, H., Svetlitchnyi, V., Gremer, L., Huber, R., and Meyer, O. (2001) Crystal structure of a carbon monoxide dehydrogenase reveals a [Ni-4Fe-5S] cluster. *Science 293*, 1281-5.

(10) Drennan, C. L., Heo, J., Sintchak, M. D., Schreiter, E., and Ludden, P. W. (2001) Life on carbon monoxide: X-ray structure of *Rhodospirillum rubrum* Ni-Fe-S carbon monoxide dehydrogenase. *Proc. Natl. Acad. Sci. U.S.A. 98*, 11973-11978.

(11) Gong, W., Hao, B., Wei, Z., Ferguson, D. J., Tallant, T., Krzycki, J. A., and Chan, M. K. (2008) Structure of the $\alpha_2\varepsilon_2$ Ni-dependent CO dehydrogenase component of the *Methanosarcina barkeri* acetyl-CoA decarbonylase/synthase complex. *Proc. Natl. Acad. Sci. U.S.A. 105*, 9558-9563.

(12) Doukov, T. I., Iverson, T. M., Seravalli, J., Ragsdale, S. W., and Drennan, C. L. (2002) A Ni-Fe-Cu Center in a Bifunctional Carbon Monoxide Dehydrogenase/ Acetyl-CoA Synthase. *Science 298*, 567-572.

(13) Lindahl, P. A. (2002) The Ni-containing carbon monoxide dehydrogenase family: light at the end of the tunnel? *Biochemistry 41*, 2097-105.

(14) Jeoung, J.-H., and Dobbek, H. (2007) Carbon Dioxide Activation at the Ni,Fe-Cluster of Anaerobic Carbon Monoxide Dehydrogenase. *Science 318*, 1461-1464.

(15) Kung, Y., Doukov, T. I., Seravalli, J., Ragsdale, S. W., and Drennan, C. L. (2009) Crystallographic Snapshots of Cyanide- and Water-Bound C-Clusters from Bifunctional Carbon Monoxide Dehydrogenase/Acetyl-CoA Synthase. *Biochemistry 48*, 7432-7440.

(16) Chen, J. Y., Huang, S., Seravalli, J., Gutzman, H., Swartz, D. J., Ragsdale, S. W., and Bagley, K. A. (2003) Infrared studies of carbon monoxide binding to carbon monoxide dehydrogenase/acetyl-CoA synthase from *Moorella thermoacetica*. *Biochemistry 42*, 14822-14830.

(17) Nemeria, N., Chakraborty, S., Baykal, A., Korotchkina, L. G., Patel, M. S., and Jordan, F. (2007) The 1',4'-iminopyrimidine tautomer of thiamin diphosphate is poised for catalysis in asymmetric active centers on enzymes. *Proc. Natl. Acad. Sci. U.S.A. 104*, 78-82.

(18) Seravalli, J., Kumar, M., Lu, W. P., and Ragsdale, S. W. (1997) Mechanism of carbon monoxide oxidation by the carbon monoxide dehydrogenase/acetyl-CoA synthase from *Clostridium thermoaceticum*: Kinetic characterization of the intermediates. *Biochemistry 36*, 11241-11251.

(19) Kung, Y., and Drennan, C. L. (2010) A role for nickel-iron cofactors in biological carbon monoxide and carbon dioxide utilization. *Curr. Opin. Chem. Biol. 15*, 276-83.

(20) Inoue, T., Fujishima, A., Konishi, S., and Honda, K. (1979) Photoelectrocatalytic reduction of carbon dioxide in aqueous suspensions of semiconductor powders. *Nature 277*, 637-638.

(21) Nguyen, T.-V., Wu, J. C. S., and Chiou, C.-H. (2008) Photoreduction of CO_2 over ruthenium dye-sensitized TiO_2-based catalysts under concentrated natural sunlight. *Catal. Commun. 9*, 2073-2076.

(22) Parkin, A., Seravalli, J., Vincent, K. A., Ragsdale, S. W., and Armstrong, F. A. (2007) Rapid and efficient electrocatalytic CO_2/CO interconversions by *Carboxydothermus hydrogenoformans* CO dehydrogenase I on an electrode. *J. Am. Chem. Soc. 129*, 10328-9.

(23) Kim, C. H., and Thompson, L. T. (2005) Deactivation of Au/CeO_x water gas shift catalysts. *J. Catal. 230*, 66-74.

(24) Menon, S., and Ragsdale, S. W. (1997) Mechanism of the *Clostridium thermoaceticum* Pyruvate:Ferredoxin Oxidoreductase: Evidence for the Common Catalytic Intermediacy of the Hydroxyethylthiamine Pyropyrosphate Radical. *Biochemistry 36*, 8484-8494.

CHAPTER VI

Conclusions and Future Directions

The work described in this thesis was focused on two enzymes: acetyl-CoA synthase and oxalate oxidoreductase. ACS has been studied for many years, and there is a wealth of information about the metals in its complex active site, the Ni-, Fe- and S-containing A-cluster. Our work on ACS involves a different metal in a newly-discovered Na^+ binding site. By contrast to ACS, OOR is a novel enzyme both in the sense that we present the first enzyme in the 2-oxoacid:ferredoxin oxidoreductase family to use oxalate as a substrate and to function independently of CoA, and in the sense that growth of *M. thermoacetica* on oxalate using OOR is the first known example of a strictly anaerobic bacterium metabolizing oxalate by directly oxidizing it to produce CO_2 and reducing equivalents.

6.1. Oxalate oxidoreductase

Chapter II describes the discovery of a novel TPP-dependent oxalate oxidoreductase. We showed that this enzyme is induced during growth on oxalate, and that it is the only enzyme necessary for oxalate oxidation in *M. thermoacetica*. OOR is a member of the 2-oxoacid:ferredoxin oxidoreductase family. It shares high sequence

similarity with other enzymes in this family, including with PFOR. The largest difference between OOR and other members of the 2-OFOR family is that OOR does not require CoA as a second substrate.

The experiments described in Chapters II and III show that although OOR does not use CoA, its catalytic mechanism is similar to the well-studied PFOR mechanism. In both enzymes, substrates react with TPP and are oxidized via a radical intermediate. In PFOR, the hydroxyethyl-TPP radical is stable, and reaction with CoA drives the catalytic cycle after HE-TPP radical formation. This has been hypothesized to occur through a large decrease in the redox potential of the radical as it combines with CoA to form an anion radical TPP adduct.

A very stable HE-TPP radical is also formed when OOR reacts with pyruvate. The formyl-TPP radical proposed as an intermediate in the OOR reaction with oxalate is apparently much less stable, and we have not been able to detect this radical by hand-mixing of samples, followed by freezing and EPR spectroscopy. We hypothesize that the stability of the radical depends on the nature of the substrate. Since oxalate is doubly negatively charged, we expect the radical intermediate in oxalate oxidation to be an anionic formyl radical. By analogy to the highly reducing anion radical that is formed when CoA reacts with the HE-TPP radical on PFOR, we propose that the anionic formyl-TPP radical is also a strong reductant that will quickly reduce the second iron-sulfur cluster on OOR.

The UV-visible stopped-flow experiments described in Chapter III showed that the mechanism of oxalate oxidation is complex, with at least two different forms of the enzyme reacting with oxalate.

6.1.1. *Proposed experiments*

The stopped-flow experiments described in Chapter III did not provide conclusive evidence as to whether a radical is stabilized during the reaction of OOR with oxalate. One limitation to the stopped-flow experiments is that probably the only visible change that is being monitored is the reduction of the iron-sulfur clusters. Two techniques have been developed in other laboratories to measure changes in the active sites of TPP-dependent enzymes. First, the subtle changes in the spectrum of TPP associated with tautomerization state changes and formation of intermediates might be seen more clearly by circular dichroism spectroscopy, where different forms of TPP give rise to large positive and negative bands in the visible region (*1, 2*), which might allow changes in the spectrum of TPP to be seen more clearly against the background of the reduction-associated bleaching of the iron-sulfur clusters. Second, acid-quenching followed by NMR has allowed quantification of different covalent TPP-bound intermediates on pyruvate decarboxylase (*3*). Mass spectrometry is another possible method for detection of TPP-bound intermediates. These techniques could be used to monitor steps before iron-sulfur cluster reduction. Knowing steady state concentrations of intermediates could provide evidence in favor of or against the kinetic schemes proposed in Chapter III, and could allow assignment of rate constants to individual reaction steps, with the goal of finding rate constants for the steps involved in oxidation of the proposed formyl-TPP and formyl-TPP radical intermediates.

A second area for exploration is the overall equilibrium of the OOR reaction. As mentioned in Section 3.3.1, the presence of CO_2 in solution affects the equilibrium of the

first half-reaction of OOR. Our attempts to measure the rate of the overall reverse reaction, reduction of CO_2 to oxalate, have so far been unsuccessful, but a systematic exploration of how the reaction of oxalate with OOR is affected by the concentration of CO_2 in solution could give more information about the rates of individual steps in the reaction, since CO_2 would be expected to specifically affect the rates of steps involving CO_2 release, allowing identification of those steps.

The original reason for our stopped-flow experiments was to try to answer the question whether a formyl-TPP radical is formed at appreciable concentrations during the oxidation of oxalate by OOR, and if so, to find a good reaction time to use for rapid freeze-quench EPR experiments. A complementary approach, of freeze-quenching mixtures of OOR and oxalate at many different times and looking at these samples by EPR, has the obvious advantage that this method could unambiguously detect a radical, if formed at sufficiently high concentrations, whereas UV-visible spectroscopy does not allow distinction between the one-electron and two-electron reduced forms of OOR.

6.2. Characterization of a sodium binding site in acetyl-CoA synthase

The work described in Chapter IV began with the discovery of a sodium site on ACS by Dr. Yan Kung, in Dr. Cathy Drennan's lab at MIT. We hypothesized that this site is important for CoA binding because of its proximity to Trp418, which is protected from reaction with tryptophan-modifying chemicals by CoA (*4, 5*). The experiments described in Chapter IV provide preliminary support for this hypothesis. We found that the CO/acetyl-CoA exchange activity of ACS increases approximately four-fold when the Na^+ concentration is increased from 40μM and 5 mM. We also found that mutation of the

only residue whose side-chain coordinates the Na^+ atom, E331, to alanine decreases the CO/acetyl-CoA exchange activity by about 20-fold, relative to wild-type ACS. This mutation has no apparent effect on the ability of ACS to bind Ni and Fe, as is expected, since the Na^+ site is about 23 Å from the active site. The mutation also has no apparent effect on the stability of ACS, as evidenced by the fact that expression levels of E331A ACS are similar to those of wild-type ACS, and by the similar melting temperatures of E331A and wild-type ACS. A more conservative mutation, E331D also had no great effect on expression and Ni and Fe binding, and had no consistent effect on the CO/acetyl-CoA exchange activity. Given the probability that ACS is somewhat flexible, mutation of glutamate to aspartate was expected to still allow for full coordination of Na^+.

6.2.2. *Proposed experiments*

The results described in Chapter IV show a consistent effect of Na^+ on the CO/acetyl-CoA exchange activity of ACS, both through the Na^+ concentration effect on activity, and through disruption of Na^+ binding by mutagenesis. However, the conclusions drawn from these experiments should be further tested by two lines of experimentation.

First, the experiments in Chapter IV should be repeated and expanded upon to allow drawing firmer conclusions. Although the magnitude of the effect of mutation of E331A on the CO/acetyl-CoA exchange activity is fairly consistent, the actual activity of wild-type, E331A and E331D ACS has not been clearly shown, due to large variations between assays done on different days. Efforts to make the assay more consistent are

described in Chapter IV. The inconsistency in the results could also be addressed by doing more assays to more clearly define the range of activity for each ACS variant. The EPR spectra of all three ACS variants varied between different preparations of enzyme. Additional preparations of each enzyme should be done to test whether mutation of E331 to alanine consistently gives enzyme with smaller amounts of NiFeC EPR signal than are seen with wild-type ACS. This is an important experiment to test the hypothesis that the Na^+ site is not needed for proper incorporation of the A-cluster into ACS. The Na^+ dependence of the CO/acetyl-CoA exchange activity could also be measured in more assays to try to more clearly define the effects between 40 μM and 5 mM Na^+, where the activity increases with Na^+, and above 5 mM Na^+, where the activity seems to be somewhat inhibited by higher Na^+ concentrations.

Second, experiments should be done to directly test the hypothesis that the Na^+ site is important for CoA binding, by measuring CoA binding to ACS under different Na^+ concentrations, and by comparing the CoA binding affinities of wild-type and E331A ACS. The best method to measure the Na^+ dependence of CoA binding will be one that allows the precautions described in Chapter IV for excluding Na^+. Equilibrium dialysis experiments could be done in the anaerobic chamber in plastic containers. Equilibrium dialysis has been successfully used by other researchers to measure CoA binding to ACS (*6*). The CoA binding affinity should be determined at Na^+ concentrations from the lowest achievable (around 30 μM) to 100 mM, to see if there is an effect on the CoA binding affinity that mirrors the effect on the CO/acetyl-CoA exchange activity.

The effect of Na^+ on CoA binding could also be studied by measuring the effect of different concentrations of CoA on assays of ACS over a range of Na^+ concentrations.

The CO/acetyl-CoA exchange assay is inhibited by CoA (*7*). A second assay, the CoA exchange assay, measures the transfer of the acetyl-group on acetyl-CoA to dephospho-CoA, or of the acetyl-group on acetyl-dephospho-CoA to CoA. Measuring the K_i for CoA in the CO/acetyl-CoA exchange assay or the effect of CoA and dephospho-CoA concentrations on activity in the CoA exchange assay at different Na^+ concentrations would allow us to assess whether Na^+ affects CoA binding.

6.3. References

(1) Nemeria, N., Baykal, A., Joseph, E., Zhang, S., Yan, Y., Furey, W., and Jordan, F. (2004) Tetrahedral intermediates in thiamin diphosphate-dependent decarboxylations exist as a 1',4'-imino tautomeric form of the coenzyme, unlike the Michaelis complex or the free coenzyme. *Biochemistry 43*, 6565-75.

(2) Jordan, F., Nemeria, N. S., Zhang, S., Yan, Y., Arjunan, P., and Furey, W. (2003) Dual catalytic apparatus of the thiamin diphosphate coenzyme: acid-base via the 1',4'-iminopyrimidine tautomer along with its electrophilic role. *J. Am. Chem. Soc. 125*, 12732-8.

(3) Tittmann, K., Golbik, R., Uhlemann, K., Khailova, L., Schneider, G., Patel, M., Jordan, F., Chipman, D. M., Duggleby, R. G., and Hubner, G. (2003) NMR analysis of covalent intermediates in thiamin diphosphate enzymes. *Biochemistry 42*, 7885-91.

(4) Shanmugasundaram, T., Kumar, G. K., and Wood, H. G. (1988) Involvement of tryptophan residues at the coenzyme A binding site of carbon monoxide dehydrogenase from *Clostridium thermoaceticum*. *Biochemistry 27*, 6499-6503.

(5) Morton, T. A., Runquist, J. A., Ragsdale, S. W., Shanmugasundaram, T., Wood, H. G., and Ljungdahl, L. G. (1991) The primary structure of the subunits of carbon monoxide dehydrogenase/acetyl-CoA synthase from *Clostridium thermoaceticum*. *J. Biol. Chem. 266*, 23824-23828.

(6) Wilson, B. E., and Lindahl, P. A. (1999) Equilibrium dialysis study and mechanistic implications of coenzyme A binding to acetyl-CoA synthase/carbon monoxide dehydrogenase from *Clostridium thermoaceticum*. *J. Biol. Inorg. Chem. 4*, 742-748.

(7) Ragsdale, S. W., and Wood, H. G. (1985) Acetate biosynthesis by acetogenic bacteria. Evidence that carbon monoxide dehydrogenase is the condensing

enzyme that catalyzes the final steps of the synthesis. *J. Biol. Chem. 260*, 3970-3977.